Title

Boiling Intelligence: Vision-Based and Event-Driven Flow Boiling Analysis

ISBN

9798186377337

Author

Chang, Sanghyeon

Publication Date

2026-08-20

Peer reviewed|Thesis/dissertation

UNIVERSITY OF CALIFORNIA,
IRVINE

Boiling Intelligence: Vision-Based and Event-Driven Flow Boiling Analysis

DISSERTATION

submitted in partial satisfaction of the requirements
for the degree of

DOCTOR OF PHILOSOPHY

in Mechanical and Aerospace Engineering

by

Sanghyeon Chang

Dissertation Committee:
Professor Yoonjin Won, Chair
Associate Professor Ramin Bostanabad
Associate Professor Aparna Chandramowlishwaran

2026

DEDICATION

To my parents

Hyuk Chang and Sunghee Choi

TABLE OF CONTENTS

Page

LIST OF FIGURES

Page

LIST OF TABLES

ACKNOWLEDGMENTS

I would like to express my sincere gratitude to my advisor, Professor Yoonjin Won, for her guidance, mentorship, patience, and support throughout my doctoral study. Her advice and encouragement have helped me grow as a researcher and as a person. I am especially grateful for the opportunities she provided, which allowed me to pursue research directions of my interest while learning the discipline and responsibility required for independent research.

I would also like to thank my dissertation committee members, Professor Aparna Chandramowlishwaran and Professor Ramin Bostanabad, for their time, insight, and constructive feedback. Their guidance helped strengthen the research presented in this dissertation.

My work at Irvine would not have been possible without the support of my colleagues, labmates, collaborators, and friends. I am grateful to everyone who shared their knowledge, offered technical help, provided thoughtful discussions, and encouraged me throughout this journey. Their support made my time in Irvine both productive and meaningful.

I would like to thank Professor Nenad Miljkovic, Professor William P. King, Professor Jiajun Wu, Professor Matteo Bucci and their research groups for their collaboration and valuable discussions through the ONR MURI program. I am also grateful to Professor Chirag Kharangate and the Purdue University Boiling and Two-Phase Flow Laboratory for sharing the microgravity flow boiling images used in Chapter 3. These data were used to investigate the artificial intelligence vision models developed in this study. In addition, I am especially grateful to Professor Nenad Miljkovic and the Energy Transport Research Laboratory at the University of Illinois Urbana-Champaign for sharing the flow boiling visualization data used in Chapter 5 to expand the flow regime classification dataset.

I gratefully acknowledge Elsevier Ltd. and Wiley for permission to include reprinted materials in this dissertation. Portions of Chapter 2 are adapted from material originally published by Elsevier Ltd. Portions of Chapter 3 are adapted from materials originally published by Elsevier Ltd. in 2023 and 2024. Chapter 5 is adapted from material originally published by Wiley in 2026.

Financial support for this dissertation was provided by the Office of Naval Research, including support through the Multidisciplinary University Research Initiatives program. I gratefully acknowledge this support.

Finally, I would like to thank my family for their unconditional love, patience, and support. This journey would not have been possible without them.

VITA

Sanghyeon Chang

EDUCATION

University of California, Irvine Irvine, CA

2026 Ph.D. in Mechanical and Aerospace Engineering

2025 M.S. in Mechanical and Aerospace Engineering

Virginia Polytechnic Institute and State University Blacksburg, VA

2021 B.S. in Mechanical Engineering

PROFESSIONAL POSITIONS

University of California, Irvine Irvine, CA

2021–2026 Research Associate

National Renewable Energy Laboratory Golden, CO

2024 Graduate Intern

Advanced Power Electronics and Electric Machines Group

Virginia Polytechnic Institute and State University Blacksburg, VA

2019–2020 Undergraduate Researcher

Independent Research Project on Lower Body Exoskeleton

AWARDS AND HONORS

William and Ida Melucci Space Exploration & Technology Fellowship
University of California, Irvine, 2025.

Beall Applied Innovation Graduate Innovation Fellowship
University of California, Irvine, 2024.

First Place Award
IEEE Symposium on Reliability for Electronics and Photonics Packaging, 2024.

First Place Award
ASME International Design Engineering Technical Conferences, 2021.

Dean's List
Virginia Polytechnic Institute and State University, 2015, 2016, and 2020.

TEACHING EXPERIENCE

2021–2024	Graduate Teaching Assistant
	MAE 120: Heat and Mass Transfer
2025	Graduate Teaching Volunteer
	MAE 295: Vision Intelligence: Methods and Applications

PUBLICATIONS

- Abere, A., **Chang, S.**, Zhao, C., Won, Y., and Weisensee, P. Investigation of droplet deformation and breakup dynamics in porous media using machine learning-assisted computer vision. *International Journal of Multiphase Flow*, 199, 105675, 2026.
- **Chang, S.**, Arani, S., Nuthalapati, N. S., Suh, Y., Choi, N., Khodakarami, S., Roni, M. R. H., Miljkovic, N., Chandramowlishwaran, A., and Won, Y. EventFlow: Real-time neuromorphic event-driven classification of two-phase boiling flow regimes. *Droplet*, e70066, 2026.
- **Chang, S.**, Paret, P., Narumanchi, S., and Won, Y. Spatiotemporal learning in power modules: Wavelet-enhanced forecasting of thermomechanical degradation. *IEEE Transactions on Components, Packaging and Manufacturing Technology*, Early Access, 2026.
- **Chang, S.**, Paret, P., Narumanchi, S., and Won, Y. Predicting thermomechanical degradation in bonded interfaces using enhanced image processing and deep learning techniques. *Proceedings of the 24th IEEE Intersociety Conference on Thermal and Thermomechanical Phenomena in Electronic Systems*, 2025.
- **Chang, S.**, Suh, Y., Shingote, C., Huang, C., Mudawar, I., Kharangate, C., and Won, Y. BubbleMask: Autonomous visualization of digital flow bubbles for predicting critical heat flux. *International Journal of Heat and Mass Transfer*, 217, 124656, 2023.
- Fu, Q., Suh, Y., Zhang, X., **Chang, S.**, and Won, Y. Bubble2Heat: Optical to thermal inference in pool boiling using physics-encoded generative neural network. *AI Thermal Fluids*, 100043, 2026.

- Gao, Y., Yu, H.-X., **Chang, S.**, Suh, Y., Won, Y., Zhu, B., and Wu, J. FluidNexus: Monocular 3D fluid reconstruction and prediction and its application in two-phase fluid. *AI Thermal Fluids*, 2026.
- Huang, C., **Chang, S.**, Suh, Y., Mudawar, I., Won, Y., and Kharangate, C. Machine learning boiling prediction: From autonomous vision of flow visualization data to performance parameter theoretical modeling. *International Journal of Multiphase Flow*, 179, 104928, 2024.
- Huang, C., **Chang, S.**, Suh, Y., Won, Y., and Kharangate, C. Modeling flow boiling utilizing machine learning vision data. *Proceedings of the 23rd IEEE Intersociety Conference on Thermal and Thermomechanical Phenomena in Electronic Systems*, 2024.
- Suh, Y., **Chang, S.**, Simadiris, P., Inouye, T., Hoque, M., Khodakarami, S., Kharangate, C., Miljkovic, N., and Won, Y. VISION-iT: A framework for digitizing bubbles and droplets. *Energy and AI*, 15, 100309, 2024.
- Zhang, X., **Chang, S.**, Suh, Y., and Won, Y. High-speed imaging driven multi-modal fusion: Enabling data-efficient segmentation for two-phase heat transfer. *AI Thermal Fluids*, 1, 100028, 2026.
- Zhao, C., Sim, J., **Chang, S.**, Yim, I., and Won, Y. ThermoVision: Non-destructive defect mapping in 3D stacked dies via surface thermography and deep learning. *IEEE Transactions on Components, Packaging and Manufacturing Technology*, 2026.

ABSTRACT OF THE DISSERTATION

Boiling Intelligence: Vision-Based and Event-Driven Flow Boiling Analysis
by
Sanghyeon Chang
Doctor of Philosophy in Mechanical and Aerospace Engineering
University of California, Irvine, 2026
Professor Yoonjin Won, Chair

Two-phase boiling is a highly effective heat transfer mechanism for high-power thermal management systems, but its performance is governed by complex, transient, and spatially distributed liquid–vapor interfacial dynamics. Conventional measurements such as temperature, pressure, and flow rate provide valuable system-level information, yet they do not directly resolve the bubble-scale and interface-scale processes that control heat transfer degradation, critical heat flux, flow instability, and regime transition. This dissertation develops a vision-based and event-based framework for characterizing, modeling, and diagnosing flow boiling heat transfer by transforming visual data streams into physically meaningful representations of interfacial behavior.

First, a flow boiling experimental platform is developed to enable high-speed visualization under controlled thermal and hydrodynamic conditions. Building on this platform, a vision-based bubble digitization framework is established using image segmentation, temporal tracking, motion estimation, and feature extraction. This framework converts raw high-speed flow boiling images into quantitative descriptors of bubble morphology, motion, vapor coverage, and wall wetting behavior. These descriptors provide a structured representation of liquid–vapor dynamics that can be analyzed across operating conditions and connected to macroscopic heat transfer behavior.

The extracted interfacial features are then used to improve the physical interpretation of microgravity flow boiling heat transfer. Under microgravity conditions, suppressed buoyancy leads to prolonged vapor residence, bubble coalescence, and reduced liquid replenishment near the heated surface. To account for these effects, image-derived wetting and dryout descriptors are incorporated into heat transfer coefficient analysis. Similarly, vision-derived interfacial parameters are integrated into mechanistic critical heat flux models, providing a more direct connection between vapor–liquid structure and macroscopic thermal performance. These results demonstrate that visual features can serve not only as image-based predictors, but also as physically interpretable descriptors of boiling heat transfer mechanisms.

In addition to frame-based imaging, this dissertation investigates neuromorphic event-camera sensing for flow boiling analysis. Unlike conventional cameras, event cameras asynchronously record pixel-level brightness changes generated by moving interfaces and transient vapor structures. Event-derived temporal, spectral, and spatial descriptors are developed to quantify interfacial activity, temporal unsteadiness, and spatial redistribution in flow boiling. The relationship between these descriptors and pressure drop behavior further demonstrates that event streams contain thermofluidically relevant information beyond qualitative visualization.

Finally, event-driven learning architectures are evaluated for real-time flow regime classification. Among the tested models, the Event LSTM framework provides an effective balance between accuracy, latency, and computational efficiency by directly processing raw event sequences without event-frame reconstruction. The Event LSTM achieves 97.6%

classification accuracy with a processing time of 0.28 ms, demonstrating the potential of sparse event streams for low latency monitoring of dynamic two-phase flow regimes.

Overall, this dissertation demonstrates that visual and event-based sensing can move flow boiling analysis beyond qualitative observation toward quantitative feature extraction, physically interpretable modeling, and real-time diagnostic prediction. By connecting high-speed imaging, computer vision, neuromorphic event sensing, machine learning, and heat transfer analysis, this work provides a foundation for more interpretable, efficient, and intelligent thermal-fluid monitoring systems.

INTRODUCTION

Advancements in technology and engineering have dramatically increased the power density demands of modern systems. Historically, early thermal management systems such as simple hotplates required relatively low heat dissipation capabilities. However, with the advent of nuclear reactors, high-power electronics, and aerospace propulsion systems, including rocket nozzles, the heat flux requirements have grown exponentially. In high-performance systems, heat fluxes can easily exceed 100 W/cm², with some specialized applications surpassing 1000 W/cm².[1] This trend underscores the critical importance of efficient thermal management strategies to ensure device performance, safety, and longevity.

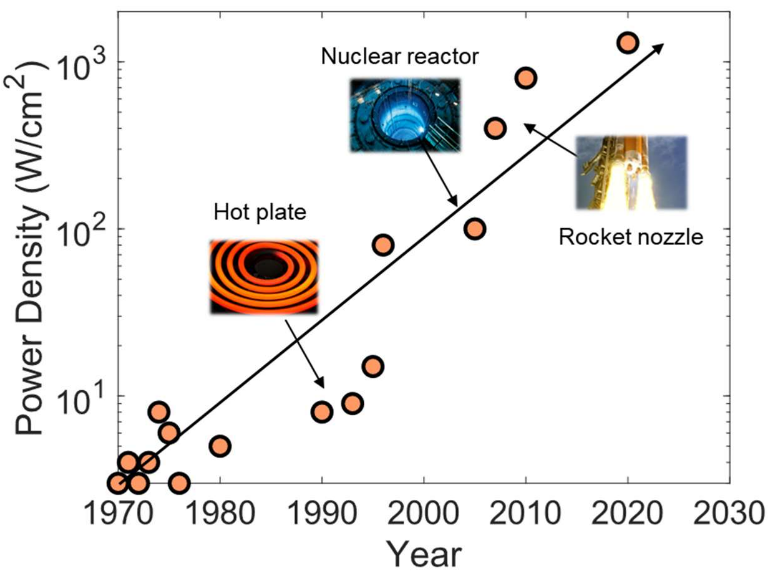

Figure 1. Power density evolution across technologies. Advances in technology have increased heat flux demands, highlighting the need for improved thermal management.

Despite continuous technological advancements, temperature-induced failures remain a dominant mode of failure in high-power systems, accounting for over 55% of component malfunctions across various industries.[2] These failures arise from localized overheating, thermal stresses, and material degradation, highlighting the urgent necessity for robust cooling technologies that can accommodate increasing thermal loads while maintaining system reliability.

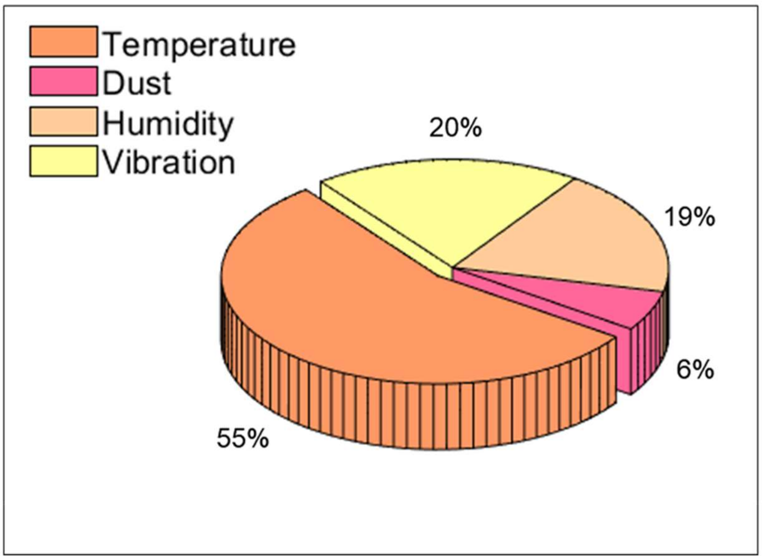

Figure 2. Temperature-related component failures in high-power systems. Despite continuous technological advancements, temperature-induced failures account for over 55% of component malfunctions across various industries.

Among the various cooling approaches developed to address this challenge, two-phase heat transfer has emerged as a highly effective technique. By leveraging both sensible and latent heat transfer mechanisms, two-phase systems offer significantly higher heat transfer coefficients compared to single-phase systems such as free or forced convection. The phase change from liquid to vapor enables efficient thermal regulation, maintaining nearly constant surface temperatures even under rapidly varying thermal loads. As illustrated in Figure 3, boiling-based cooling achieves heat transfer coefficients several orders of magnitude greater than those of traditional methods, positioning it as an ideal candidate for advanced thermal management.[3]

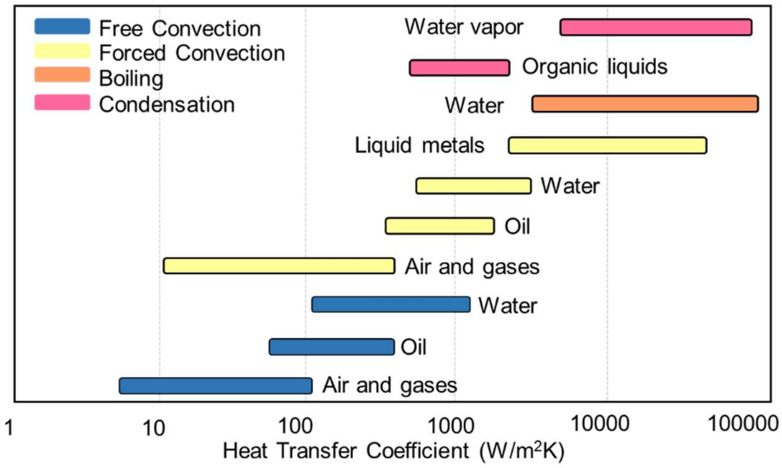

Figure 3. Two-phase heat transfer efficiency. Boiling-based cooling offers much higher heat transfer coefficients than single-phase methods, enabling stable thermal management under high heat loads.

Flow boiling, a subset of two-phase heat transfer, has received considerable attention due to its ability to combine convective heat transfer with the latent heat of vaporization. In flow boiling, the continuous motion of the liquid phase actively removes thermal resistance layers, enhancing the overall heat dissipation. It is widely utilized in compact heat exchangers, nuclear reactor cooling systems, high-performance electronic cooling, and spacecraft thermal management. Flow boiling enables high heat flux dissipation while minimizing temperature gradients across heated surfaces, thus improving operational stability and reliability.

However, flow boiling is not without challenges, and several key issues must be addressed to fully harness its advantages. One major challenge is hydrodynamic complexity. The boiling process involves the dynamic coexistence and transitions between multiple flow regimes, including bubbly, slug, churn, and annular flows. These regimes, along with their transitions, have a significant impact on local heat transfer performance, pressure drop characteristics, and overall system stability.[4] Another critical limitation is the thermal constraint associated with critical heat flux (CHF) conditions. When CHF is exceeded, the boiling surface becomes insufficiently wetted, leading to surface dry-out. This phenomenon results in a rapid escalation of surface temperature and can cause severe material degradation or burnout.[5] Additionally, boiling instabilities present further challenges. Dynamic instabilities such as pressure drop oscillations and density wave oscillations can arise from complex interactions between flow inertia, phase change processes, and system feedback mechanisms. If not properly managed, these instabilities can lead to substantial performance degradation, flow reversals, and even catastrophic system failures.[6]

The complex, spatially distributed, and transient nature of boiling phenomena has historically posed significant challenges to experimental characterization. Conventional measurement techniques, including thermocouples, pressure transducers, and flow meters, provide valuable system-level information, but they often lack the spatial and temporal resolution needed to capture rapid interface dynamics, local vapor accumulation, wetting behavior, and flow regime transitions. As a result, many conventional models for boiling heat transfer and critical heat flux rely on bulk parameters or empirical assumptions rather than direct measurements of the interfacial structures that govern heat transfer performance.

To address these limitations, recent research has increasingly leveraged computer vision techniques for high-resolution visualization and analysis of two-phase flow behavior. Computer vision methods, combined with high-speed imaging and advanced image processing algorithms, enable automated and scalable extraction of critical features such as bubble size, velocity fields, vapor coverage, wetting behavior, and interface dynamics. These approaches offer a promising pathway for improving the characterization of complex boiling phenomena without physically disturbing the system.[7,8].

Furthermore, the integration of artificial intelligence (AI) and machine learning (ML) with thermal and phase-change studies is rapidly growing.[9] As depicted in Figure 4, Scopus topic-search results show that the number of publications containing AI-related keywords increased from 273,757 in 2010–2011 to 1,856,356 in 2024–2025, while publications combining AI-related keywords with boiling or condensation increased from 19 to 550 over the same period. Although the absolute publication counts depend on the selected database, search date, and keyword combination, the strong upward trend indicates the increasing adoption of data-driven methods in phase-change heat transfer research. This trend reflects a broader shift toward AI-assisted approaches for characterizing complex thermal-fluid phenomena, identifying instability markers, predicting boiling performance and critical heat flux, and optimizing two-phase thermal systems under dynamic operating conditions.

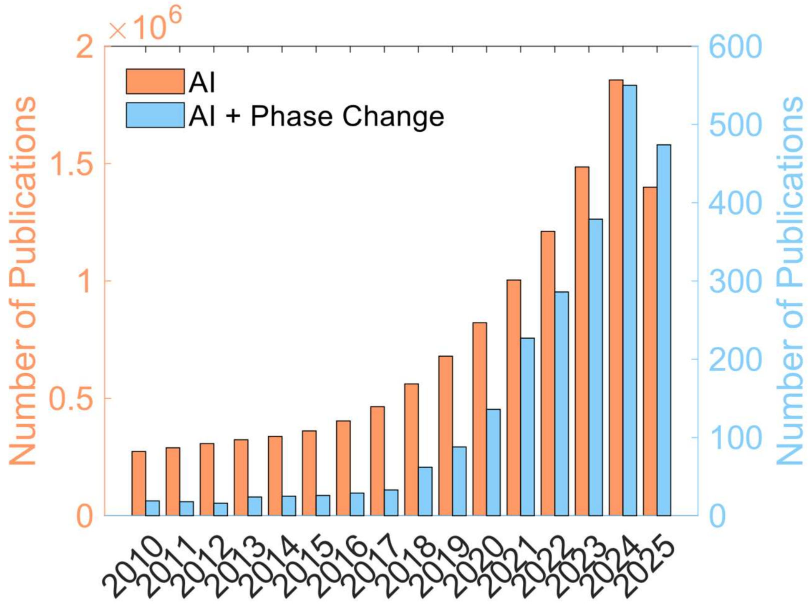

Figure 4. Growth of AI applications in thermal and phase-change research. Number of publications obtained from Scopus topic searches using AI-related keywords and their combination with boiling or condensation keywords. The AI category includes publications containing “artificial intelligence” or “machine learning,” while the AI + phase-change category includes publications containing AI-related keywords together with “boiling” or “condensation.”

Despite this progress, a major gap remains between visual observation and physical understanding of boiling processes. Many existing image-based studies focus primarily on classification accuracy, segmentation performance, or prediction error. Although these approaches can provide useful correlations, the extracted image features are not always directly connected to the physical mechanisms governing heat transfer, vapor transport, wetting behavior, pressure drop evolution, or critical heat flux. Conversely, classical heat transfer and flow boiling models provide physically interpretable relationships, but they often rely on bulk operating conditions, empirical correlations, or idealized assumptions. As a result, they may not fully account for the local and transient interfacial structures that directly influence boiling performance.

This limitation is particularly important in flow boiling systems, where thermal behavior is governed by multiscale and time-dependent interactions. At the local scale, bubble growth, coalescence, departure, vapor-layer development, and liquid replenishment influence heat transfer near the heated surface. At the channel scale, vapor accumulation, flow regime transitions, and interfacial-wave development affect pressure drop, flow stability, and thermal transport. At the system scale, these processes can interact with flow resistance, compressibility, and feedback mechanisms, leading to instabilities such as pressure drop oscillations and density-wave oscillations. Therefore, an effective diagnostic framework should not only identify visible flow patterns but also extract quantitative descriptors that represent these coupled thermal-fluid processes.

Although high-speed imaging enables direct observation of boiling interfaces, raw visualization data alone are insufficient for scalable and objective analysis. Large image datasets are difficult to examine manually, while qualitative observations such as larger bubbles, increased vapor coverage, or stronger instability must be converted into measurable descriptors to support physical interpretation. Computer vision provides a pathway for extracting quantitative information, including bubble morphology, vapor fraction, interfacial wavelength, vapor-layer thickness, and temporal interface evolution. These descriptors can then be related to heat transfer performance, critical heat flux behavior, and flow stability.

Conventional frame-based imaging also has limitations for highly transient boiling diagnostics. While high-speed cameras provide detailed spatial information, they generate substantial data volumes and sample the flow at fixed time intervals. Neuromorphic event cameras offer a complementary sensing approach by asynchronously reporting pixel-level brightness changes with microsecond-scale temporal resolution. Rather than recording complete image frames, event cameras generate sparse data streams that naturally emphasize moving interfaces, bubble motion, and rapidly changing vapor-liquid boundaries. This characteristic provides a potential route toward compact, temporally rich, and low latency monitoring of boiling systems.

However, the use of event camera measurements in boiling research remains limited. Important questions remain regarding how event streams can be converted into physically meaningful descriptors, how these descriptors relate to boiling activity and thermofluidic behavior, and whether event-driven data can support real-time diagnostics. Addressing these questions requires analysis frameworks that exploit the asynchronous and sparse characteristics of event camera sensing rather than treating event cameras simply as alternative imaging devices.

The central premise of this dissertation is that boiling interfaces contain measurable visual and event-based signatures that can be transformed into physically meaningful descriptors for heat transfer analysis, instability characterization, and real-time flow monitoring. Rather than treating visualization only as a qualitative tool, this work develops methods that convert boiling images and event streams into quantitative feature spaces. These feature spaces are used to connect interfacial behavior with thermal performance, critical thermal limits, pressure drop behavior, and flow regime dynamics.

The main contributions of this dissertation are summarized as follows. First, this work establishes a vision-based boiling analysis framework that transforms high-speed visualization data into quantitative bubble-scale and interfacial descriptors. The framework enables automated and scalable extraction of physically relevant features from large boiling-image datasets, reducing reliance on qualitative visual interpretation.

Second, this dissertation demonstrates that image-derived interfacial features provide useful physical information beyond conventional operating conditions. Bubble morphology, vapor coverage, interfacial wavelength, and related descriptors are incorporated into heat-transfer coefficient and critical heat-flux analyses to connect observed boiling structures with local heat-transfer behavior and CHF mechanisms.

Third, this work introduces neuromorphic event-camera sensing as a compact and temporally resolved diagnostic modality for boiling flows. Event-derived temporal, spectral, and spatial descriptors are developed to characterize transient interfacial activity across operating conditions. Their relationship with pressure drop behavior further demonstrates the thermofluidic relevance of event-based measurements.

Finally, this dissertation demonstrates low latency flow regime recognition using event-driven learning models. The results show that sparse event streams can support accurate real-time classification of dynamic two-phase flow regimes, providing a foundation for future closed-loop monitoring and control of boiling thermal systems.

The scope of this dissertation is experimental and data-driven. The proposed methods are developed and evaluated using the specific flow boiling configurations, working fluids, operating conditions, and visualization systems considered in this work. Therefore, the resulting models are not intended to serve as universal correlations for all boiling systems. Instead, the broader contribution of this dissertation lies in establishing a transferable methodology for extracting physically relevant information from visual and event-based measurements. This framework can be extended to other two-phase thermal systems in which interfacial motion, vapor accumulation, wetting behavior, or transient instability plays an important role.

The remainder of this dissertation is organized as follows. Chapter 1 describes the experimental platforms and measurement systems. Chapter 2 presents the vision-based bubble digitization and feature extraction framework. Chapter 3 applies image-derived interfacial features to heat transfer coefficient and critical heat flux modeling. Chapter 4 develops event-based activity descriptors for flow boiling diagnostics. Chapter 5 presents real-time event-driven flow regime classification. Finally, Chapter 6 summarizes the major findings, limitations, and future research directions.

In summary, while flow boiling offers exceptional potential for high-power thermal management, its reliable implementation requires diagnostic tools that can resolve, interpret, and respond to complex interfacial dynamics. This dissertation contributes to that goal by linking high-speed visualization, computer vision, neuromorphic event sensing, machine learning, and heat-transfer analysis into a unified framework for boiling research. By moving from qualitative observation toward quantitative feature extraction, physical interpretation, and real-time diagnosis, this work aims to advance the understanding and monitoring of two-phase boiling heat-transfer systems.

CHAPTER 1: Experimental Platforms for Two-Phase Boiling Studies

1.1 Introduction

This study develops an integrated experimental and imaging platform to investigate two-phase flow boiling phenomena from both thermofluidic and vision-based perspectives. The objective is to establish a unified framework that enables simultaneous acquisition of physical measurements and high-fidelity visual data, providing a direct connection between interfacial dynamics and macroscopic heat transfer behavior. Flow boiling is selected as the primary focus because it directly couples bubble growth, vapor transport, pressure variation, mass flow rate, and heat transfer performance under forced convection conditions.

A key challenge in flow boiling analysis is that many important physical processes occur at rapidly evolving liquid-vapor interfaces. Conventional sensor-based measurements provide essential information such as temperature, pressure, and flow rate, but they do not directly resolve local bubble dynamics, vapor accumulation, interfacial motion, or dryout-related behavior. In contrast, optical imaging provides access to local interfacial structures but requires systematic processing to convert visual information into quantitative physical descriptors. Therefore, integrating synchronized thermal-fluid measurements with advanced imaging is essential for linking local two-phase flow dynamics to system-level heat transfer behavior.

To address this need, the experimental platform developed in this study combines a closed-loop flow boiling facility with high-speed optical imaging and neuromorphic event-based sensing. The closed-loop facility enables controlled variation of operating conditions, including mass flow rate, heat flux, inlet temperature, and pressure. High-speed imaging captures transient bubble and vapor dynamics with high temporal resolution, while event-based imaging detects asynchronous brightness changes associated with moving interfaces and rapid phase redistribution. This combination allows the same flow boiling process to be analyzed from complementary perspectives: conventional thermal-fluid response, frame-based visual structure, and event-based dynamic activity.

The resulting dataset provides the foundation for the analysis frameworks developed in the following chapters. Vision-based image processing is used to extract bubble and interfacial descriptors, including bubble size, velocity, void fraction, vapor coverage, wetting behavior, and vapor structure evolution. These features are then incorporated into vision-based heat transfer modeling to connect local interfacial behavior with heat transfer coefficient and critical heat flux prediction. In addition, event-camera measurements are used to quantify temporal and spatial activity in flow boiling, providing a basis for low latency activity analysis and real-time flow regime classification. By focusing on flow boiling, this dissertation establishes an experimental foundation for connecting local liquid-vapor interfacial dynamics with macroscopic heat transfer performance and real-time diagnostic capability. The following sections describe the design of the flow boiling facility, the test section and heating assembly, the instrumentation system, and the imaging methods used throughout the study.

1.2 Flow Boiling Facility

The flow boiling facility is designed as a closed-loop experimental system for investigating two-phase flow behavior under controlled thermal and hydrodynamic conditions. The facility enables regulation of mass flow rate, inlet temperature, pressure, and heat input while providing optical access to the heated flow channel. This section describes the working fluid, flow loop configuration, test section geometry, heater assembly, and instrumentation used to establish repeatable flow boiling experiments.

The working fluid used in the loop is Flutec PP1, a dielectric liquid with a relatively low boiling point. The thermophysical properties of Flutec PP1 are compared with those of water in Table 1. Although water has higher latent heat of vaporization and thermal conductivity, Flutec PP1 is selected because of its dielectric nature and low saturation temperature. These characteristics allow safe operation with electrically heated components and enable boiling experiments to be conducted at relatively low temperatures. Therefore, Flutec PP1 provides a suitable working fluid for the present flow boiling platform.

Table 1. Comparison of key thermophysical properties of Flutec PP1 and water

Property	Flutec PP1	Water
Boiling Point (1 atm)	57 °C	100 °C
Liquid Density	1682 kg/m³	997 kg/m³
Latent Heat of Vaporization	85.5 kJ/kg	2257 kJ/kg
Thermal Conductivity	0.065 W/m·K	0.606 W/m·K
Surface Tension	11.1 mN/m	72.0 mN/m
Electrical Property	Dielectric	Conductive

The test section consists of two polycarbonate blocks, each measuring 30 mm in width, 12 mm in thickness, and 390 mm in length. A rectangular flow channel is machined into the top block with a width of 2.5 mm and a depth of 5 mm, corresponding to a hydraulic diameter of 3.33 mm. The transparent polycarbonate structure provides optical access to the flow channel while maintaining mechanical support for pressurized closed-loop operation. The inlet and outlet are connected through NPT tube ports located at 16.25 mm and 373.75 mm from the channel inlet, respectively. Additional 1/8 in NPT ports are incorporated for pressure and temperature measurements at axial locations of 56 mm, 194 mm, 249 mm, and 353 mm, corresponding to the inlet, flow development region, heater inlet, and heater outlet.

Heat is supplied through a resistance-based heating assembly integrated into the lower block of the test section. The heated section incorporates six 240 Ω thin-film resistors mounted on a copper heater base and connected to a variable power supply. The resistors are electrically connected in parallel to provide controlled and repeatable heat generation. The copper heater, measuring 100 mm in length and 1.6 mm in thickness, is embedded within a groove in the polycarbonate block to reduce conductive resistance between the heater and the flow channel. Compared with earlier design iterations using ceramic heaters, this resistor-based configuration provides higher heat flux capability and is better suited for driving the flow toward high heat flux conditions.

The final test section design adopts a simplified two-block configuration with outer gasket sealing and compression between aluminum support plates. This design improves sealing performance, structural stability, and ease of assembly. The optical quality of the channel is further enhanced through polishing procedures to improve visualization of bubble nucleation, growth, coalescence, and vapor transport during flow boiling experiments.

The fabrication of the copper heater assembly is one of the most technically challenging aspects of the experimental setup because it requires precise electrical insulation, reliable thermal contact, and mechanically stable wiring within a compact geometry. To achieve uniform heating, six resistors are mounted on the copper heater and electrically connected in parallel. During fabrication, particular care is taken to prevent electrical shorting between the resistor terminals, connecting wires, and the copper substrate. To reduce this risk, the side surfaces of the resistors are first abraded using sandpaper to remove conductive material near the edges that could otherwise promote unintended electrical contact. The resistors are then attached to the copper heater using solder paste. After the resistors are positioned on the copper surface, the heater assembly is placed in an oven at approximately 200°C for about 10 min to reflow the solder paste and bond the resistors firmly to the copper base, as shown in Figure 5.

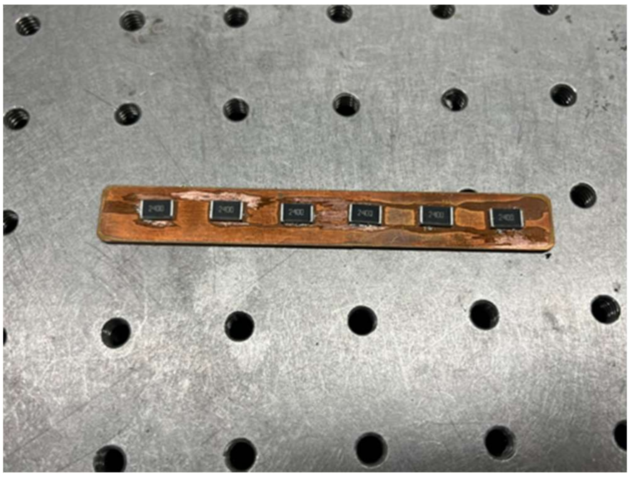

Figure 5. Fabrication of the copper heater assembly through resistor mounting

After the heater cools to room temperature, lead wires are prepared for electrical connection. Each wire tip is first dipped into a solder bath to produce a thin and uniform solder coating prior to final attachment. This pre-tinning process minimizes excessive solder accumulation during manual soldering and improves control over the final joint geometry , as shown in Figure 6. The wires are then connected to the resistor pads using a soldering iron, while careful attention is given to preventing the soldered leads from contacting the copper substrate, since such contact can directly cause electrical shorting. To further reduce this risk, thermal tape is applied as an insulating barrier in critical regions during assembly, as shown in Figure 7(left). Once all electrical connections are completed and verified, epoxy is applied over the soldered regions to mechanically reinforce the joints and improve durability during operation, as shown in Figure 7(right). This final encapsulation step helps secure the wire–resistor connections against vibration, handling, and thermal cycling. Through this multi-step fabrication process, a robust copper heater assembly is obtained, providing reliable electrical insulation, strong mechanical integrity, and stable heat generation for flow boiling experiments.

Figure 6. Solder bath pre-tinning and final wire attachment process for electrical connection. Lead wires are dipped into a solder bath to form a thin and uniform coating prior to attachment.

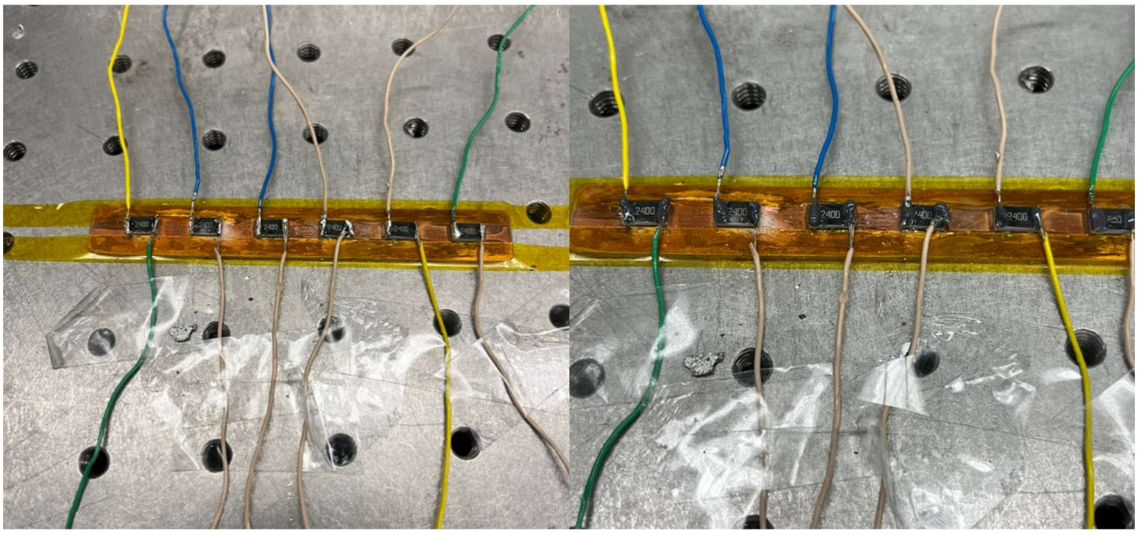

Figure 7. Insulation and reinforcement of the copper heater assembly. Thermal tape used to electrically isolate critical regions during assembly (left). Epoxy applied over the soldered connections for mechanical support and protection (right).

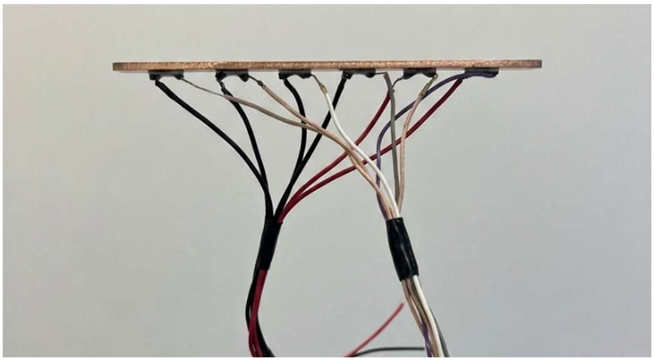

Figure 8. Final assembled copper heater (side view). The completed heater assembly after wire attachment, insulation, and epoxy reinforcement, showing the compact configuration of the resistors and lead connections. The side view highlights the overall structural integrity and electrical isolation achieved through the multi-step fabrication process.

To monitor thermal behavior, Type-K thermocouples are installed along the copper heater and bonded using thermally conductive epoxy to ensure accurate wall temperature measurements. Additional high-temperature epoxy is applied to reinforce the connections and enhance durability. The test section is further instrumented with 1/8 in NPT ports for pressure and temperature measurements at axial locations of 56 mm, 194 mm, 249 mm, and 353 mm from the channel inlet, corresponding to the inlet, flow development region, heater inlet, and heater outlet. The inlet and outlet are connected through NPT tube ports located at 16.25 mm and 373.75 mm, respectively. The copper heater is positioned 215 mm from the channel inlet and seated within a groove that accommodates gasket sealing to prevent leakage. The entire assembly is compressed between aluminum plates to ensure structural integrity and leak-free operation.

Beyond the test section, the flow loop includes a pump, inline heater, flow meter, reservoir, and condenser to maintain stable closed-loop operation, as illustrated in Figure 9. The flow is driven using an Ismatec Digital Gear Pump, and a differential pressure sensor is installed to monitor pressure variations across the system. A flow meter provides accurate measurement of the flow rate, which is a critical parameter governing liquid replenishment and heat transfer behavior in flow boiling. An inline circulation heater is employed to preheat the working fluid to near-saturation conditions prior to entering the test section, thereby minimizing subcooled boiling effects. A reservoir and condenser are incorporated to maintain continuous operation by returning vapor to the liquid phase. Numerical data are acquired using a Phidget-based data acquisition system, while visual data are collected using both high-speed optical imaging and neuromorphic event-based imaging. The high-speed camera records conventional frame-based images of bubble and vapor structures, whereas the event-based camera asynchronously detects local brightness changes generated by moving liquid-vapor interfaces. In this chapter, the event-based camera is introduced as part of the imaging system; its operating principle and event-data representation are discussed in detail in Chapter 4, where event-based sensing is used for flow boiling activity analysis and real-time diagnostic development.

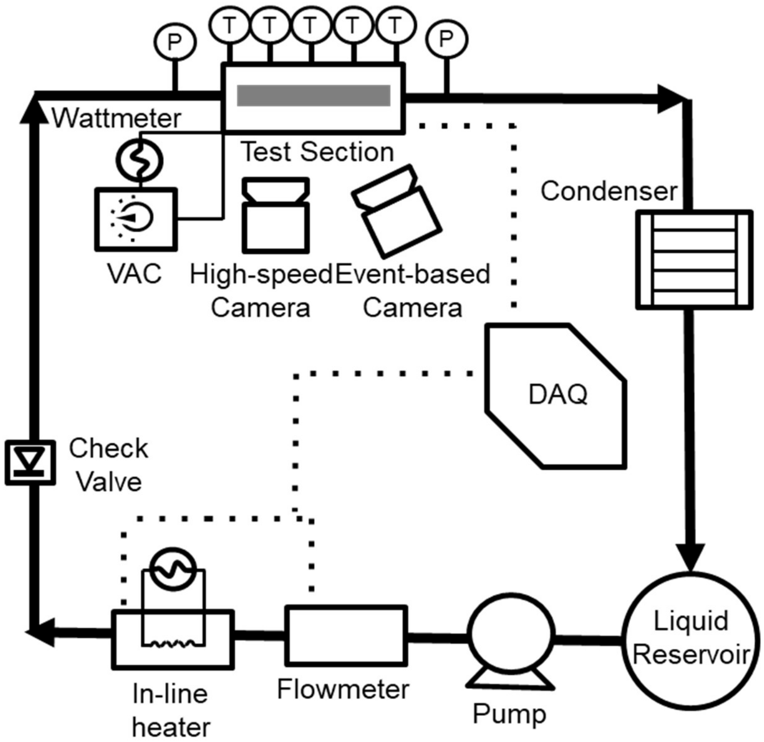

Figure 9. Schematic of the flow boiling loop and instrumentation layout.
The closed-loop system includes a liquid reservoir, pump, heater section, and downstream components, with integrated sensors and a data acquisition (DAQ) system for monitoring operating conditions.

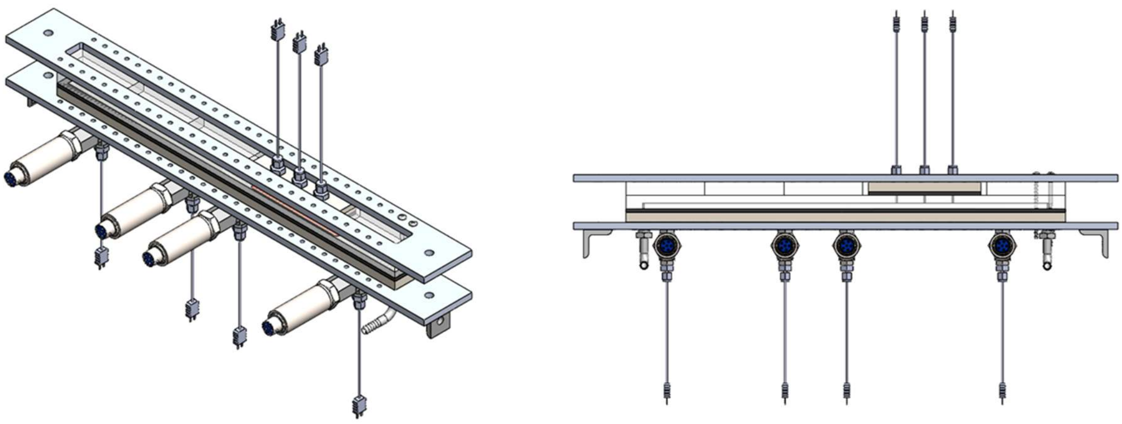

Figure 10. CAD model of the flow boiling experimental setup.

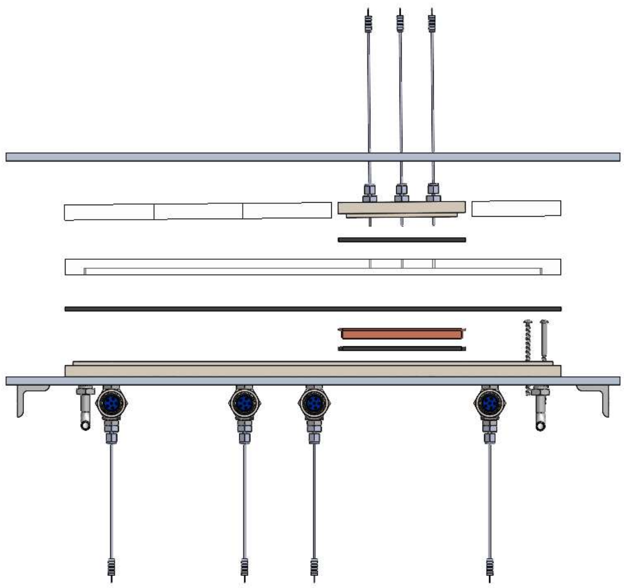

Figure 11. CAD parts of the flow boiling experimental setup.

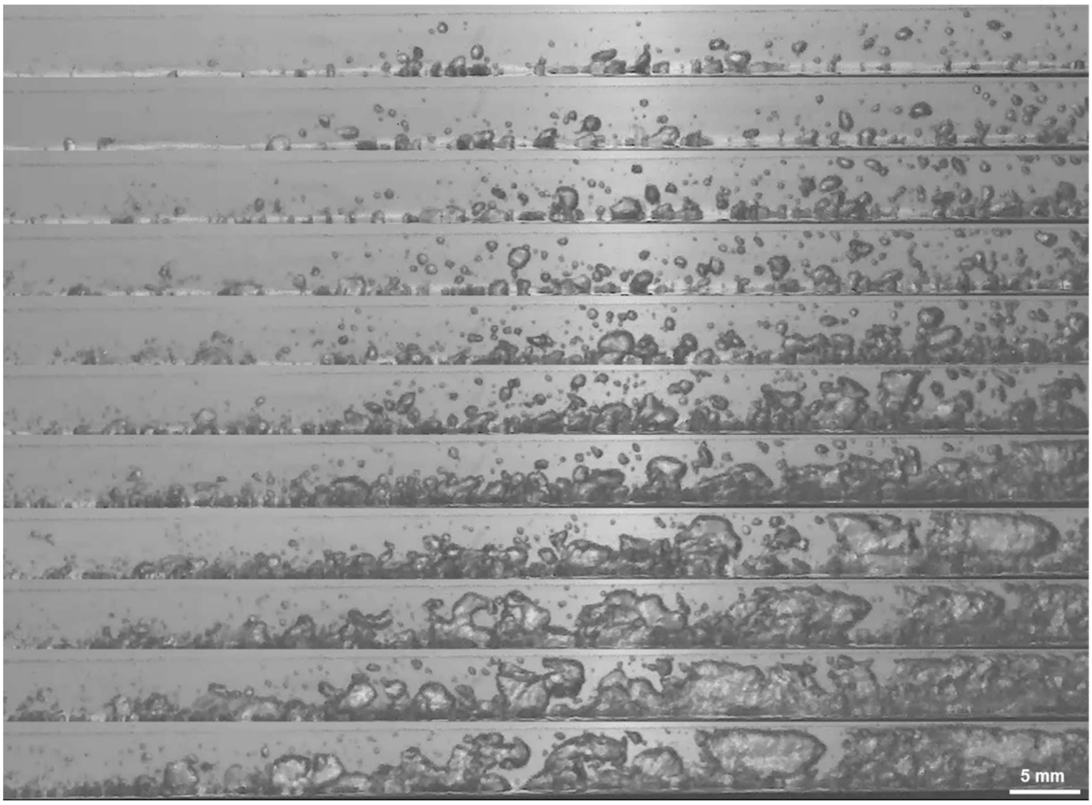

Figure 12. Representative visualization of flow boiling at a mass flow rate of 16 g/s.
High-speed image showing bubble nucleation, growth, coalescence, and transport along the heated surface within the flow channel. The spatial distribution of bubbles illustrates the evolution of two-phase structures, with increasing vapor accumulation and interaction downstream

1.3 Conclusion

This chapter establishes the experimental foundation of the dissertation by developing an integrated flow boiling platform that supports both thermofluidic measurement and vision-based analysis. The flow boiling facility provides a controlled closed-loop environment for investigating two-phase flow behavior under forced convection. By enabling regulation of mass flow rate, inlet temperature, pressure, and heat input, the platform provides a repeatable experimental basis for studying flow boiling dynamics under well-defined thermal and hydrodynamic conditions.

A central contribution of this chapter lies in the integration of advanced imaging modalities with conventional thermal-fluid instrumentation. High-speed optical imaging and neuromorphic event-based sensing are incorporated to capture transient boiling behavior with complementary representations. High-speed imaging provides frame-based visualization of bubble and vapor structures, while event-based imaging records asynchronous brightness changes associated with moving liquid-vapor interfaces. This combined measurement capability extends beyond traditional sensor-based approaches by directly linking macroscopic operating conditions with evolving interfacial structures and dynamic boiling activity.

This chapter also details the mechanical design, fabrication strategy, and instrumentation architecture required to achieve stable and repeatable flow boiling operation. The development of the resistor-based copper heater assembly, the implementation of sealing and structural support strategies, and the incorporation of temperature, pressure, and flow diagnostics collectively ensure the reliability of the experimental system. These design considerations are essential not only for maintaining experimental consistency, but also for producing high-quality datasets suitable for subsequent vision-based and data-driven analysis.

Overall, this chapter provides the physical and methodological framework upon which the remainder of the dissertation is built. By combining controlled flow boiling experiments with synchronized sensor, optical, and event-based measurements, the developed platform enables a unified investigation of interfacial dynamics, heat transfer behavior, and real-time diagnostic capability. The datasets and capabilities established here directly support the segmentation, tracking, motion analysis, feature extraction, event-based activity analysis, and modeling studies presented in the following chapters.

CHAPTER 2: Vision-Based Bubble Digitization and Feature Extraction Framework

2.1 Introduction

Accurate characterization of bubble dynamics is fundamental to understanding two-phase flow boiling heat transfer.[10–12] Bubble nucleation, growth, departure, coalescence, and transport govern key thermal-fluid mechanisms, including heat transfer enhancement, flow instability, and critical heat flux.[13–15] However, these phenomena are inherently spatiotemporal and highly nonlinear, making them difficult to quantify using conventional measurement techniques. Traditional approaches rely primarily on point-based sensor data, such as temperature, pressure, and flow rate, which provide indirect and spatially averaged information about the boiling process.[10,12,16] As a result, critical information regarding bubble morphology, motion, and interaction dynamics remains difficult to obtain.[17]

Recent advances in high-speed imaging have enabled direct visualization of boiling processes, offering detailed access to bubble behavior inside the flow channel.[18–20] Despite this progress, extracting quantitative and physically meaningful information from visual data remains a significant challenge.[21,22] Conventional image processing techniques often rely on heuristic thresholding, edge detection, or manual annotation, which are highly sensitive to noise, illumination variation, reflection, and bubble deformation. These limitations become more pronounced under high heat flux conditions, where bubbles exhibit rapid growth, coalescence, elongation, overlap, and partial occlusion in confined flow boiling environments.[14,23] Consequently, there is a need for a robust and scalable framework that can systematically convert raw high-speed images into quantitative representations suitable for scientific analysis and modeling.

To address these challenges, this study develops a vision-based bubble digitization and feature extraction framework that transforms high-speed image sequences into structured, physics-relevant data. The framework integrates Mask R-CNN-based segmentation, algorithm-based tracking, and quantitative feature extraction. Segmentation is used to identify bubble regions and generate pixel-level masks, while tracking establishes temporal correspondence between bubble instances across consecutive frames. The tracked bubble information is then converted into measurable descriptors such as bubble size, shape, centroid location, velocity, residence behavior, and spatial distribution.

The proposed framework is designed to support quantitative analysis of flow boiling images under varying heat flux and flow conditions. By using supervised instance segmentation, the framework improves robustness compared with conventional threshold-based image processing methods, particularly when bubble boundaries are irregular or visually ambiguous. The use of algorithm-based tracking provides a transparent and computationally efficient method for linking segmented bubbles over time, allowing dynamic bubble features to be extracted from high-speed image sequences.

The extracted features are designed to bridge the gap between visual observation and thermofluidic modeling. Unlike traditional approaches that treat visual data primarily as qualitative evidence, the present framework produces quantitative descriptors that can be directly used in downstream analysis. These descriptors provide the basis for heat transfer modeling, critical heat flux analysis, and flow boiling characterization in the following chapters.

Overall, this chapter establishes a focused vision-based pipeline for digitizing and analyzing bubble dynamics in flow boiling. The framework enables a systematic transition from raw high-speed images to structured physical descriptors, forming the methodological foundation for the vision-based feature extraction and heat transfer analysis developed throughout this dissertation.

2.2 Framework Overview

This section presents an overview of the vision-based bubble digitization framework developed in this study. The framework is designed to systematically transform high-speed flow boiling images into structured, physics-relevant representations of bubble dynamics. The overall pipeline, illustrated in Figure 13, consists of four main stages: (i) data acquisition and preprocessing, (ii) Mask R-CNN-based bubble segmentation, (iii) algorithm-based temporal tracking, and (iv) feature extraction and data representation.

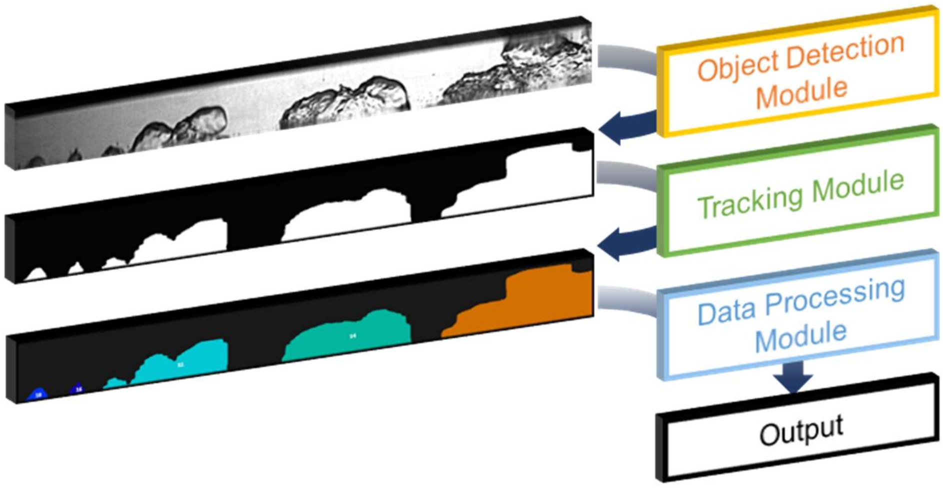

Figure 13. Overview of the vision-based pipeline The proposed framework converts high-speed flow boiling images into physics-relevant bubble descriptors through four main stages: data acquisition and preprocessing, Mask R-CNN-based bubble segmentation, algorithm-based temporal tracking, and feature extraction for quantitative data representation.

The framework focuses on flow boiling image sequences collected under controlled operating conditions. Raw high-speed images acquired from the flow boiling facility serve as the input to the pipeline. These datasets include variations in heat flux, mass flow rate, pressure, and inlet thermal conditions, allowing the framework to capture changes in bubble morphology and motion as the boiling process evolves along the heated channel. By applying a consistent processing workflow to these image sequences, the framework enables systematic comparison of bubble behavior across operating conditions.

The first stage of the pipeline focuses on data acquisition and preprocessing. High-speed image sequences are collected from the optically accessible flow boiling test section. The raw images are then conditioned through preprocessing operations such as region-of-interest selection, background normalization, frame alignment, and image quality adjustment. This step standardizes the input data and improves the reliability of subsequent segmentation and tracking tasks, particularly under nonuniform illumination, reflection, and visually complex flow boiling conditions.

The second stage performs bubble segmentation using Mask R-CNN. In this stage, bubble regions are identified and separated from the background at the pixel level. Mask R-CNN is used because it provides instance-level segmentation, allowing individual bubble structures to be detected separately even when multiple bubbles are present within the same frame. The segmentation output consists of binary masks, bounding boxes, and object-level information for each detected bubble. These outputs provide the spatial foundation for tracking and quantitative feature extraction.

The third stage consists of algorithm-based temporal tracking, where segmented bubbles are associated across consecutive frames to establish temporal continuity. In this study, tracking is performed using a geometry-based association method with KD-tree-based nearest-neighbor searching. Bubble centroids extracted from the segmentation masks are used as object positions, and associations are determined based on spatial proximity and prescribed displacement constraints between consecutive frames. This approach provides a transparent and computationally efficient method for reconstructing bubble trajectories from high-speed image sequences.

The final stage involves feature extraction and data representation. From the segmented and tracked bubble data, the framework computes quantitative descriptors such as bubble area, equivalent diameter, centroid position, velocity, displacement, residence behavior, spatial distribution, and bubble count. These outputs are organized into structured datasets that preserve both frame-level and trajectory-level information. In this way, the proposed framework directly converts raw flow boiling images into measurable descriptors that can be used for heat transfer analysis and physics-informed modeling in subsequent chapters.

Overall, the proposed framework establishes a focused methodology for converting high-speed flow boiling images into structured and physically meaningful representations of bubble dynamics. By integrating Mask R-CNN-based segmentation, KD-tree-based temporal tracking, and feature extraction, the framework enables consistent quantitative analysis of bubble behavior under varying flow boiling conditions.

2.3 Bubble Segmentation

Bubble segmentation is a fundamental step in the proposed vision-based analysis framework because it defines the spatial extent of bubble structures from which subsequent measurements are derived. Accurate segmentation enables the extraction of physically meaningful quantities such as bubble area, equivalent diameter, centroid location, shape, and spatial distribution. These quantities directly influence the reliability of tracking and feature extraction stages because errors in the segmented bubble regions propagate into the calculated geometric and kinematic descriptors.

Segmentation in flow boiling images is challenging due to the complex visual characteristics of two-phase flow. Bubble boundaries often exhibit low contrast against the background because of reflection, refraction, nonuniform illumination, and variations in local image intensity. In addition, bubbles continuously grow, deform, merge, elongate, and overlap as they are transported along the heated channel. These effects become more pronounced under high heat flux conditions, where vapor structures become denser and individual bubble boundaries are more difficult to distinguish. As a result, conventional image processing techniques, such as intensity-based thresholding, edge detection, and morphological operations, often struggle to provide robust and consistent segmentation across different flow boiling conditions.

To overcome these limitations, this study adopts Mask R-CNN as the primary segmentation method. Mask R-CNN is a supervised instance segmentation model that detects individual bubble objects and generates pixel-level masks for each detected instance. This instance-level capability is important for flow boiling analysis because multiple bubbles can appear within the same frame, interact with one another, and partially overlap. By learning bubble appearance from annotated high-speed images, the model provides more robust segmentation than conventional threshold-based approaches under visually complex conditions.

A structured annotation and model development process is established to train the Mask R-CNN model. Representative high-speed flow boiling images are manually annotated to generate pixel-level bubble masks, which serve as ground truth labels for supervised learning. The annotated images include a range of bubble conditions, such as isolated bubbles, elongated bubbles, coalescing bubbles, and partially overlapping structures. This annotation strategy improves the ability of the model to detect bubble structures under varying heat flux and flow conditions. The output of the segmentation stage consists of pixel-level masks and object-level information for each detected bubble. From these masks, geometric properties such as projected area, equivalent diameter, perimeter, centroid location, and bounding box dimensions are computed. These descriptors provide the spatial foundation for subsequent tracking and feature extraction. Through this segmentation process, raw high-speed flow boiling images are transformed into structured bubble-level representations suitable for quantitative analysis.

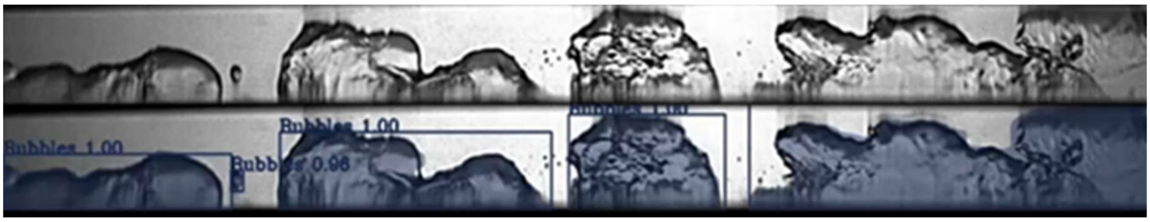

Figure 14. Mask R-CNN-based bubble segmentation results for flow boiling images. Representative outputs show pixel-level bubble masks, object boundaries, and detected bubble instances under varying flow boiling conditions.

2.4 Bubble Tracking

Bubble tracking is performed after segmentation to establish temporal correspondence between detected bubble instances across consecutive frames. While segmentation identifies bubble regions at each time step, tracking connects these segmented objects over time and reconstructs their trajectories. This temporal continuity allows dynamic bubble descriptors, such as displacement, velocity, residence behavior, and growth history, to be extracted from high-speed image sequences.

Tracking flow boiling bubbles is challenging because bubble motion is not always smooth or uniform. Bubbles may grow, deform, merge, split, or become partially obscured as they move through the channel. In addition, the presence of multiple bubbles in close proximity can create ambiguity when assigning object identities between frames. Therefore, the tracking method must be able to associate bubble detections efficiently while maintaining physically reasonable temporal continuity.

In this study, bubble tracking is implemented using an algorithm-based association method with KD-tree-based nearest-neighbor searching. For each segmented bubble, the centroid position is calculated from the corresponding mask. The centroid locations in the current frame are then compared with those in the following frame. A KD-tree structure is used to efficiently search for the nearest candidate bubble based on spatial proximity. Associations are accepted only when the displacement between consecutive detections satisfies a prescribed maximum displacement criterion. This constraint helps reduce incorrect matches caused by sudden jumps, overlapping detections, or unrelated neighboring bubbles.

The tracking procedure assigns a consistent identity to each bubble as it appears across frames. When a bubble in the next frame is matched to a bubble in the current frame, the trajectory is extended. If no valid match is found within the displacement threshold, the existing trajectory is terminated. Similarly, newly detected bubbles that are not matched to previous objects are initialized as new trajectories. This procedure provides a transparent and computationally efficient way to construct time-resolved bubble trajectories from segmentation outputs.

From the resulting trajectories, dynamic quantities are calculated, including frame-to-frame displacement, streamwise and transverse velocity components, total velocity magnitude, residence time, and changes in bubble size over time. These tracking-derived descriptors are used together with segmentation-derived geometric features to characterize bubble behavior under different flow boiling conditions. In this way, KD-tree-based tracking transforms discrete bubble detections into continuous spatiotemporal representations that support the quantitative analysis presented in subsequent chapters.

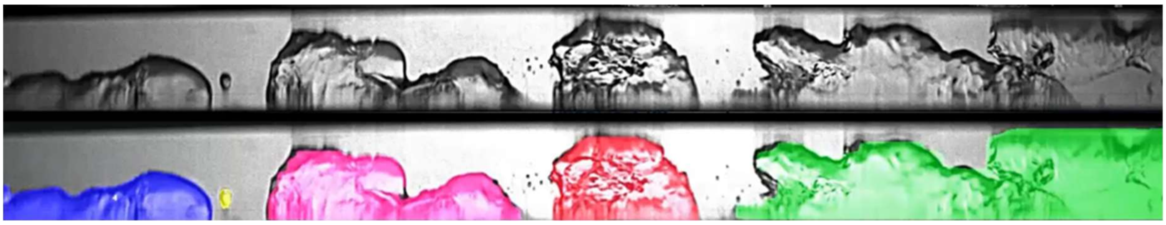

Figure 15. Tracking results from flow boiling. Representative bubble tracking results obtained from the segmented flow boiling image sequence. Each detected bubble is assigned a unique identification number, allowing individual bubble instances to be temporally linked across consecutive frames. The assigned IDs enable reconstruction of bubble trajectories and extraction of tracking-based descriptors such as displacement, velocity, residence time, and temporal changes in bubble size.

2.5 Feature Extraction and Data Representation

Feature extraction is the final stage of the proposed vision-based bubble digitization framework, where segmented and tracked flow boiling images are transformed into structured quantitative descriptors. While Mask R-CNN segmentation defines the spatial extent of bubble regions and KD-tree-based tracking establishes temporal continuity, feature extraction converts these outputs into measurable quantities that can be used for physical interpretation and heat transfer analysis. The extracted features are categorized into geometric and kinematic descriptors. Geometric features are derived from segmentation masks and describe the spatial properties of individual bubbles. These include projected area, equivalent diameter, perimeter, centroid location, bounding box dimensions, and shape-related quantities. Such descriptors provide fundamental information about bubble morphology, size distribution, and spatial organization within the flow channel. Table 2 summarizes the hierarchy of image-derived descriptors generated by the proposed framework, from low-level image information to object-level geometric features, time-resolved kinematic features, and population-level descriptors.

Table 2. Hierarchical Bubble Descriptors for Flow Boiling Analysis

Feature level	Analysis stage	Representative descriptors
Low-level image information	Preprocessing and mask generation	Edges, contours, intensity contrast, bubble boundaries
Object-level geometric features	Segmentation	Bubble area, equivalent diameter, perimeter, centroid location, bounding box size, bubble count
Time-resolved kinematic features	Tracking	Bubble trajectory, displacement, streamwise velocity, transverse velocity, residence time, temporal size variation
Population-level descriptors	Feature aggregation	Bubble size distribution, bubble number density, spatial distribution, condition-averaged statistics

Kinematic features are obtained from tracking results and describe the temporal evolution of bubbles. By analyzing bubble trajectories across consecutive frames, quantities such as streamwise displacement, transverse displacement, velocity, residence time, and temporal changes in bubble size are computed. These features are important for characterizing bubble transport along the heated channel and for relating bubble motion to flow boiling behavior under different operating conditions. In particular, velocity estimation based on tracked centroids provides a direct and consistent measure of bubble motion from high-speed image sequences.

In addition to individual bubble properties, population-level descriptors are calculated to summarize the collective behavior of bubbles within the field of view. These include bubble count, spatial distribution, bubble population density, and changes in bubble size distribution with increasing heat flux or flow rate. Such descriptors are useful for identifying changes in vapor generation, bubble accumulation, and two-phase flow development along the channel.

The extracted features are organized into structured datasets that preserve both frame-level and trajectory-level information. At the frame level, segmentation-derived descriptors describe the instantaneous bubble population and spatial distribution. At the trajectory level, tracking-derived descriptors describe the temporal evolution of individual bubbles as they move through the image sequence. This data structure allows systematic comparison of bubble behavior across operating conditions, including variations in heat flux, mass flow rate, pressure, and inlet temperature.

The resulting feature dataset forms the basis for the heat transfer analysis presented in the following chapter. By converting high-speed flow boiling images into quantitative descriptors, the framework enables image-derived bubble information to be linked with macroscopic thermal-fluid measurements. In this way, feature extraction serves as the bridge between visual observation and physics-informed analysis.

Overall, this stage completes the vision-based digitization process by transforming segmented and tracked bubble data into structured physical descriptors. These descriptors provide a consistent basis for analyzing flow boiling behavior and support the subsequent modeling of heat transfer performance using image-derived information.

2.6 Conclusion

This chapter establishes a vision-based bubble digitization and feature extraction framework for converting high-speed flow boiling images into structured quantitative descriptors. The framework integrates instance segmentation, temporal tracking, and feature extraction to systematically identify bubble regions, link bubble instances across consecutive frames, and quantify both geometric and kinematic characteristics of vapor structures. By replacing manual observation and threshold-based processing with a more automated and scalable workflow, the proposed framework enables consistent analysis of complex bubble behavior under varying flow boiling conditions.

The segmentation stage provides pixel-level bubble masks that describe the spatial extent, morphology, and distribution of vapor structures. The tracking stage establishes temporal correspondence between bubble instances, allowing bubble trajectories, displacement, velocity, residence behavior, and temporal size variation to be evaluated. These outputs are then transformed into object-level, trajectory-level, and population-level descriptors, including bubble area, equivalent diameter, centroid location, bubble count, velocity, residence time, and spatial distribution. Together, these descriptors provide a structured representation of bubble dynamics that can be compared across operating conditions such as heat flux, mass flow rate, pressure, and inlet temperature.

The resulting feature dataset serves as a bridge between visual observation and thermofluidic analysis. Rather than treating high-speed images only as qualitative evidence, the proposed framework converts visual information into measurable physical quantities that can be used for downstream modeling. This capability is particularly important for flow boiling, where bubble morphology, vapor accumulation, wetting behavior, and interfacial motion are closely connected to heat transfer performance, critical heat flux, and flow stability.

Overall, this chapter provides the methodological foundation for the image-derived heat transfer analysis presented in the following chapter. By transforming raw visualization data into quantitative bubble-scale and interfacial descriptors, the framework enables a more direct connection between observed liquid–vapor dynamics and macroscopic boiling performance.

CHAPTER 3: Image-Derived Flow Boiling Features for Heat Transfer Modeling

3.1 Introduction

Understanding and predicting heat transfer performance in two-phase boiling systems remains a central challenge in thermal sciences. Flow boiling is widely used for high-heat-flux thermal management because it utilizes both latent and sensible heat, enabling substantially greater heat removal than single-phase cooling.[2] However, this advantage is sustained only below the critical heat flux (CHF) limit, beyond which a boiling crisis occurs. Once CHF is reached, liquid contact with the heated surface is severely disrupted, causing a sharp deterioration in heat transfer performance and a rapid rise in wall temperature.[24] As a result, CHF serves as one of the most important design constraints in two-phase thermal management systems.[25]

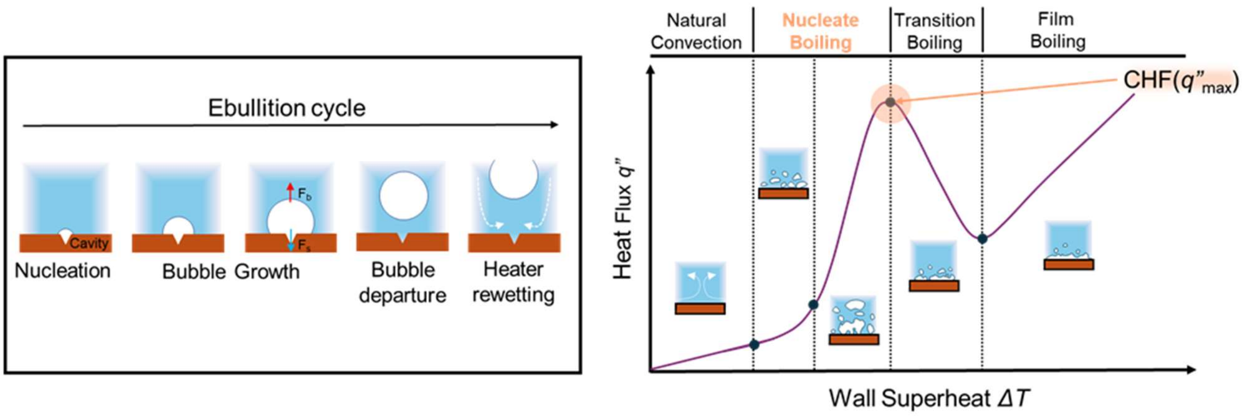

Figure 16. Ebullition cycle and Boiling curve during boiling. The ebullition cycle illustrates bubble growth and departure during boiling. As heat flux rises, heat transfer improves until reaching the critical heat flux (CHF), where vapor buildup reduces cooling efficiency and causes a rapid temperature increase.

In addition to CHF, other key performance parameters such as vapor void fraction and heat transfer coefficient (HTC) are also essential for characterizing flow boiling systems. Void fraction governs phase distribution within the channel and strongly affects pressure drop, flow regime transition, and interfacial transport behavior. The heat transfer coefficient reflects the cooling capability of the system and is closely linked to local wetting, vapor coverage, and interfacial renewal at the heated wall. Accurate prediction of CHF, void fraction, and HTC is therefore critical for robust design and operation of boiling-based thermal systems, particularly under conditions where the liquid-vapor interface evolves rapidly and non-uniformly.

Despite the advantages of two-phase thermal management systems, their implementation in space applications remains challenging due to flow instabilities and system failure risks associated with critical heat flux (CHF). These challenges are further compounded by uncertainties in other key performance parameters, including void fraction and heat transfer coefficient.[26] Void fraction influences pressure drop and flow regime transitions by determining the spatial distribution of vapor, while the heat transfer coefficient governs cooling efficiency through its sensitivity to interfacial dynamics and surface wetting. Accurate estimation of these parameters is therefore essential for the robust and reliable design of flow boiling systems.

Conventional predictive approaches for boiling heat transfer and CHF have primarily relied on empirical correlations or semi-empirical formulations derived from bulk measurements such as heat flux, wall temperature, mass flow rate, vapor quality, and pressure. Owing to the complexity and importance of CHF, more than a thousand empirical correlations have been developed over the past several decades to predict CHF under different operating conditions.[27] Although these correlations have been widely adopted, their applicability is often restricted to the specific geometries, working fluids, surface conditions, and flow environments under which they were developed. As a result, their predictive capability can deteriorate when extended beyond their calibration range, especially in two-phase flows where local vapor structures, wetting behavior, and transient interface motion directly determine thermal performance.

At the fundamental level, boiling heat transfer is governed by complex interfacial processes, including bubble nucleation, growth, departure, coalescence, liquid replenishment, vapor accumulation, local dry-out, and interaction with the surrounding liquid. These bubble-scale processes strongly influence macroscopic quantities such as CHF, void fraction, pressure drop, and heat transfer coefficient. Numerous factors have been reported to affect CHF, including wettability,[28] liquid spreading ability,[29] surface roughness,[30] capillarity and wickability[31], porosity,[32,33] Rayleigh–Taylor instability wavelength,[33] and critical pressure.[34] However, the highly coupled and transient nature of these mechanisms makes CHF difficult to predict using bulk-parameter-based correlations alone.

To improve the physical understanding of CHF and related boiling instabilities, several mechanistic models have been proposed over the past several decades. Representative examples include the *Bubble Crowding Model*,[35] *Boundary Sublayer Model*,[36] *Boundary Layer Separation Model*,[35] and *Interfacial Lift-off Model*.[37–39]

The *Bubble Crowding Model* postulates that CHF occurs when vapor bubbles grow and accumulate near the heated wall, forming a dense bubbly layer that interferes with the liquid supply from the bulk flow. As the bubble concentration increases, the transport of liquid toward the surface becomes insufficient to maintain wetting, ultimately leading to dry-out. This model highlights the importance of turbulent flow in sustaining liquid contact with the wall and identifies the local bubble concentration as a critical parameter in predicting CHF.

The *Boundary Sublayer Model* suggests that CHF occurs when a thin, liquid sublayer trapped underneath an evolving vapor blanket is completely vaporized. As the vapor blanket thickens and elongates, the liquid sublayer beneath it thins out due to evaporation. CHF is triggered once the available liquid in this sublayer cannot absorb the incoming heat flux, leading to complete local dry-out. Key parameters include the thickness of the liquid sublayer and its capacity for heat absorption.

The *Boundary Layer Separation Model* hypothesizes that CHF results from the obstruction of forward liquid motion near the wall by the production of vapor. The growing vapor layer at the wall separates the boundary layer from the surface, preventing bulk liquid access and causing rapid surface overheating. This model emphasizes the instability of the hydrodynamic boundary layer under intense vapor generation conditions.

The *Interfacial Lift-off Model* proposes that CHF occurs when the momentum generated by vapor at wetting fronts exceeds the pressure force that maintains liquid-wall contact. This results in the interface lifting off from the wall, forming a continuous vapor layer that blocks further heat removal by liquid. The model incorporates interfacial instability analysis and conservation laws of mass, momentum, and energy, and highlights critical parameters such as wetting front length, vapor layer thickness, and interfacial wavelength.

management systems in space applications.

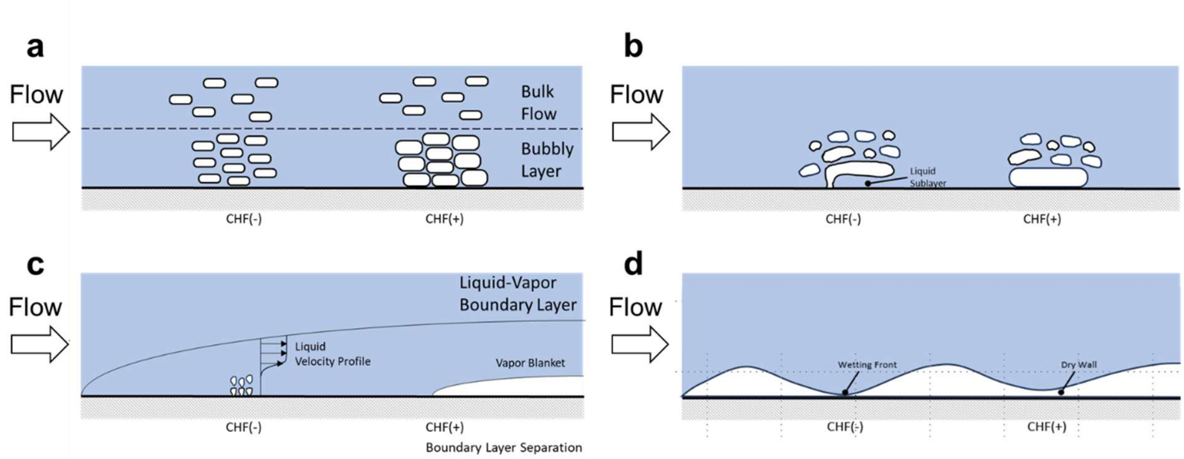

Figure 17. Flow boiling critical heat flux mechanistic theoretical models. (a) Bubble Crowding Model (b) Boundary Sublayer Model (c) Boundary Layer Separation Model (d) Interfacial Lift-off Model.

In addition to critical heat flux, another critical parameter for assessing system performance is the vapor void fraction, defined as the ratio of the cross-sectional area occupied by vapor to the total cross-sectional area of the channel. Void fraction influences key system characteristics such as pressure drop, flow regime transitions, and heat transfer behavior. However, direct measurement of void fraction in flow channels is often difficult due to the rapid and irregular motion of vapor-liquid interfaces. Therefore, researchers have developed various theoretical models and empirical correlations to predict void fraction, broadly classified into the *Homogeneous Model*,[40] *Slip Ratio Model*,[41–43] *Drift-Flux Model*,[44,45] *Empirical Correlations*.[46,47] and *Separated Flow Model*.[48] These frameworks provide important foundations for understanding phase distribution in flow boiling systems.

Another important design parameter in flow boiling is the heat transfer coefficient, which represents the system's ability to remove heat from the heated surface. Predicting the heat transfer coefficient is challenging due to its strong dependence on the flow regime. For example, the relationship between vapor quality and heat transfer coefficient is weak or slightly negative at low vapor qualities but becomes strongly negative at high vapor qualities.[5] In addition, the heat transfer coefficient experiences a sudden decline when critical heat flux or dry-out occurs. Over the years, numerous experimental studies have been conducted to develop correlations specific to various flow boiling configurations. Correlations have been proposed based on local measurements in circular tubes with refrigerants, studies in both circular and rectangular channels, and experiments under saturated and subcooled conditions.[49–52] Additional correlations have been derived through extensive databases and experimental campaigns focusing on different fluids and geometries.[53–57] In recent years, predictive models based on machine learning techniques have also been introduced, offering new potential for improved accuracy and adaptability.[58–60] While empirical correlations remain the most widely used tools for predicting the heat transfer coefficient, further advancements are needed to fully capture the complex and dynamic nature of two-phase flow boiling across a wide range of operating conditions.

Although these correlations offer valuable insights into heat transfer behavior, they remain constrained by limited access to high-resolution physical descriptors. Most models rely on bulk parameters or empirically fitted constants, with minimal incorporation of detailed interfacial features that directly influence heat transfer performance.

Despite substantial progress in the development of CHF, void fraction, and heat transfer coefficient models, a major limitation remains: the lack of direct, high-resolution measurements of vapor structures, interfacial dynamics, and instability wavelengths. These physical descriptors are essential for validating and refining theoretical models, yet they have historically been difficult to measure because two-phase flows are rapid, heterogeneous, and inherently three-dimensional. Although conventional image processing techniques such as thresholding and edge detection have been used to extract features from boiling images, these methods often struggle with variable gray-level intensities caused by light reflection, irregular bubble shapes, and dynamic deformation during bubble growth, sliding, coalescence, and dry-out.[61]

Recent advances in high-speed imaging and computer vision provide an opportunity to address this challenge by transforming visual observations of boiling into structured, quantitative data. Rather than relying solely on bulk measurements, vision-based analysis enables direct extraction of interface-level descriptors that govern heat transfer enhancement and degradation. In this context, the vision-based digitization framework developed in Chapter 2 provides a foundation for systematically extracting physically meaningful features from experimental observations, including projected bubble geometry, bubble motion, wetting characteristics, vapor coverage, wetting front length, interfacial wavelength, and vapor blanket thickness.

Building upon this foundation, the present chapter develops feature-informed models for boiling performance analysis. The extracted interfacial descriptors are used to investigate their relationship with key thermal parameters, particularly heat transfer coefficient and critical heat flux. An vision-based model is first developed for HTC by incorporating image-derived wetting and dry-out behavior. This is followed by a vision-based framework for CHF prediction using interfacial features associated with vapor accumulation, instability development, and wall dry-out. Together, these approaches establish a unified perspective in which bubble-scale interfacial dynamics serve as the link between visual observation and boiling performance.

The analyses in this chapter are based on flow boiling datasets obtained under microgravity conditions from Purdue University. In these experiments, buoyancy effects are largely suppressed, allowing interfacial behavior to be governed primarily by surface tension and inertial forces. This setting provides a useful opportunity to isolate the relationship between bubble dynamics and thermal performance. Although direct quantitative comparison with terrestrial boiling must be made with caution, the physical relationships identified here provide insight into the mechanisms governing two-phase heat transfer more broadly.

3.2 Image-Derived Interfacial Features in Microgravity Flow Boiling

Boiling heat transfer is fundamentally governed by interfacial dynamics occurring at the heated surface, where the distribution and evolution of liquid and vapor phases directly determine thermal performance. Bubble nucleation, growth, departure, interaction, and coalescence collectively regulate key mechanisms such as liquid replenishment, microlayer evaporation, and transient conduction. As a result, macroscopic quantities such as heat transfer coefficient and critical heat flux are intrinsically linked to bubble-scale behavior and interfacial structure.

The datasets analyzed in this study are obtained from flow boiling experiments conducted under microgravity conditions. In the absence of buoyancy-driven forces, bubble motion is governed primarily by surface tension and inertial effects rather than gravitational detachment. This leads to prolonged bubble residence near the heated surface, enhanced bubble coalescence, and increased vapor accumulation along the flow direction. As a result, interfacial dynamics play a more dominant role in determining heat transfer behavior, providing a clearer and more direct linkage between observable bubble features and the underlying physical mechanisms governing wetting, dry-out, and vapor transport.

Figure 18. Comparison between earth gravity and microgravity. In Earth gravity, bubbles rise and detach due to buoyancy. In microgravity, bubbles stay attached to the surface, grow larger, and behave differently, affecting heat transfer and boiling performance.

To quantitatively investigate these mechanisms, the vision-based framework described in Chapter 2 is applied to extract interfacial information from high-speed imaging data. Through segmentation, tracking, and data processing, raw visual observations are transformed into structured descriptors of bubble behavior and phase distribution. One of the most fundamental quantities derived from image data is the void fraction, which represents the relative presence of vapor within the flow.[62,63] As illustrated in Figure 19, void fraction is computed using a pixel-based approach by distinguishing vapor and liquid regions through image segmentation. By counting vapor pixels relative to the total area, the temporal and spatial evolution of vapor distribution can be directly quantified, thereby establishing a direct bridge between visual data and classical two-phase flow parameters.

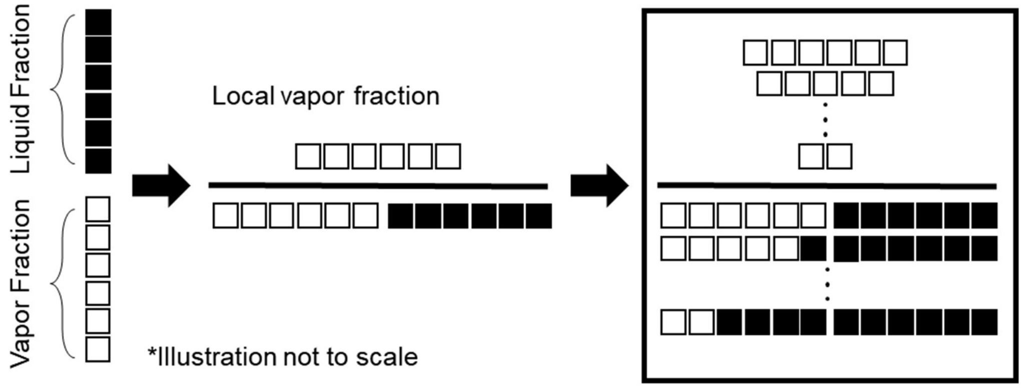

Figure 19. Pixel-based void fraction calculation. In the data processing module, void fraction is obtained by tabulating white pixels (representing vapor) and black pixels (representing working fluid).

Beyond global vapor fraction, more detailed interfacial features can be extracted to characterize local boiling behavior. As shown in Figure 20, key interfacial characteristics such as wetting front length, vapor wavelength, and vapor layer thickness are obtained from high-speed images. These quantities provide a refined description of liquid–vapor interactions near the heated surface. In particular, wetting front length represents the extent of liquid contact, while vapor wavelength and layer thickness characterize the spatial organization of vapor structures. These features serve as physically meaningful descriptors that capture the balance between wetting and dry-out processes.

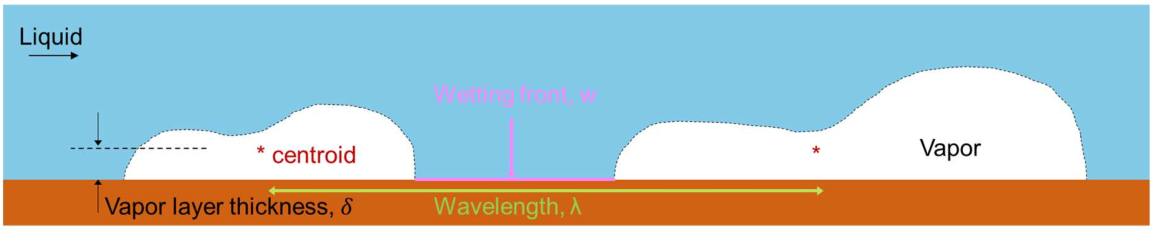

Figure 20. Interfacial characteristics under flow boiling. Wetting front length, vapor wavelength, and layer thickness are extracted from high-speed images for quantitative analysis.

A more comprehensive description of interfacial structure is provided in Figure 21 where spatial distributions of wetting front, interfacial length, wavelength, and vapor fraction are quantified across the flow channel. These parameters collectively describe the evolution of liquid–vapor distribution and provide direct measures of surface wetting and vapor coverage. In particular, the ratio between wetting front length and interfacial wavelength reflects the relative dominance of liquid contact versus vapor accumulation, offering a compact descriptor of interfacial state.

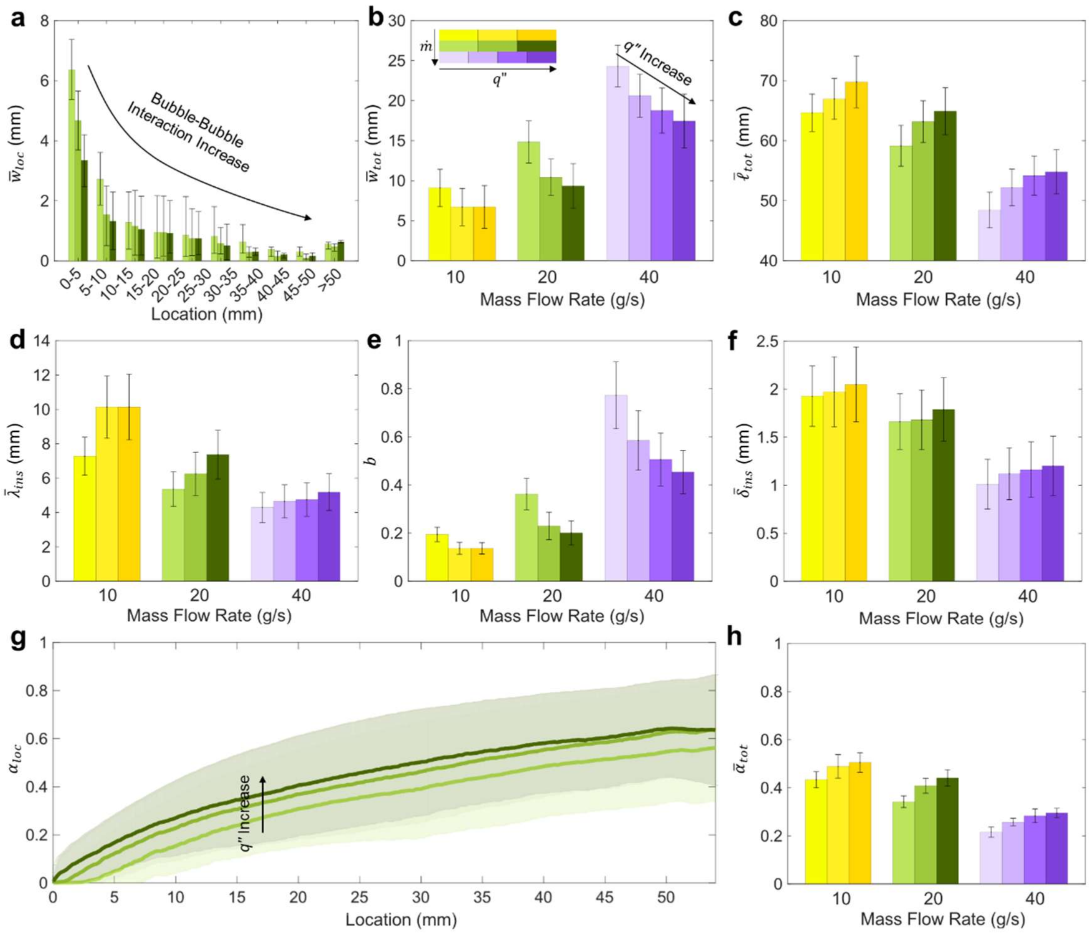

Figure 21. Interfacial characteristics. (a) Local wetting front w_{loc} of a mass flow rate of 20 g/s (b) Average of total wetting front over the channel w_{tot} for different mass flow rates (10 – 40 g/s) with varying heat flux. (c) Average of total interfacial length l_{tot}. (d) Average wavelength of individual bubbles λ_{ins}. (e) Constant b representing the ratio of overall wetting front length to overall wavelength. (f) Average vapor layer thickness of individual bubble δ_{ins}. (g) Local vapor fraction profile αloc of mass flow rate of 20 g/s. The lines represent average values from 3,000 images, and bands represent one standard deviation for each heat flux. (h) Average of total vapor fraction α_{tot}. Error bars from (a – d, and f) indicate the 16th and 84th percentile of the data, while error bars in (e) represent one standard deviation.

In addition to spatial structure, bubble dynamics play a critical role in determining interfacial behavior. As shown in Figure 22, bubble velocity exhibits strong dependence on both mass flow rate and heat flux. Increasing flow rate leads to higher bubble velocities and enhanced bubble removal, which promotes liquid replenishment at the heated surface. Conversely, lower velocities result in prolonged bubble residence and increased probability of coalescence, contributing to vapor accumulation. The observed increase in bubble velocity along the flow direction further indicates the influence of bubble–bubble interactions and flow acceleration, highlighting the importance of dynamic transport processes in boiling systems.

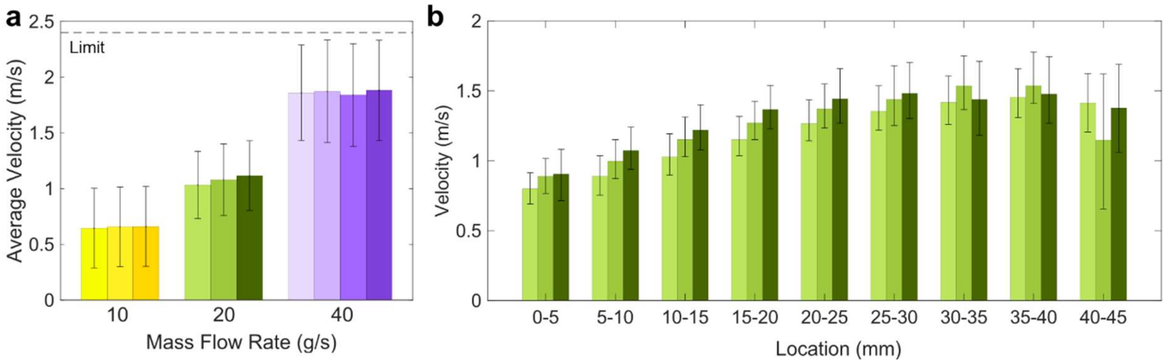

Figure 22. Bubble dynamics. (a) Average velocity plots for three different mass flow rates (10–40 g/s) with varying heat flux. Each mass flow rate represents 0.5, 0.9 and 1.8 m/s, which is comparable with flow inlet velocity. (b) Local velocity profiles of mass flow rates of 20 g/s within the regime of interest. Individual bubble velocities increase in the direction of flow in the channel potentially due to bubble-bubble interactions. The filtered bubbles after 45 mm of channel are not depicted in this plot. Both error bars of (a) and (b) indicate the 16th and 84th percentile of the data set for each case.

The combined effects of interfacial structure and bubble dynamics are reflected in the spatial evolution of vapor distribution along the channel. As shown in Figure 23, void fraction increases in the downstream direction, indicating progressive vapor accumulation. At lower mass flow rates, higher void fractions and larger fluctuations are observed, suggesting reduced liquid replenishment and stronger vapor dominance. In contrast, higher mass flow rates suppress vapor accumulation and stabilize the flow, resulting in lower void fractions and reduced variability.

These trends demonstrate how operating conditions directly influence the balance between wetting and dry-out.

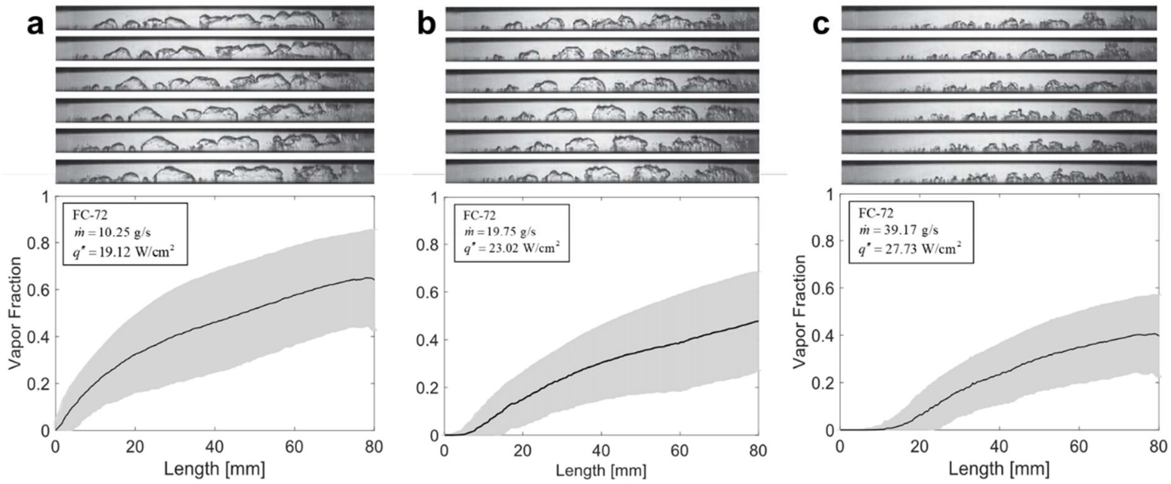

Figure 23. Void fraction profiles under varying mass flow rates and heat flux conditions. Time-averaged void fraction distributions with standard deviation bands for three test cases (a) 10.25 g/s at 76% of CHF, (b) 19.75 g/s at 77% of CHF, and (c) 39.17 g/s at 77% of CHF.

Statistical analysis of bubble dynamics further supports these observations. As shown in Figure 24, bubble size decreases with increasing mass flow rate, indicating enhanced bubble removal and reduced residence time. Conversely, lower mass flow rates lead to larger bubbles and increased likelihood of coalescence. The variation in aspect ratio reflects changes in bubble deformation and elongation under different flow conditions. These statistical trends highlight the competition between bubble growth and removal mechanisms, which ultimately governs interfacial behavior.

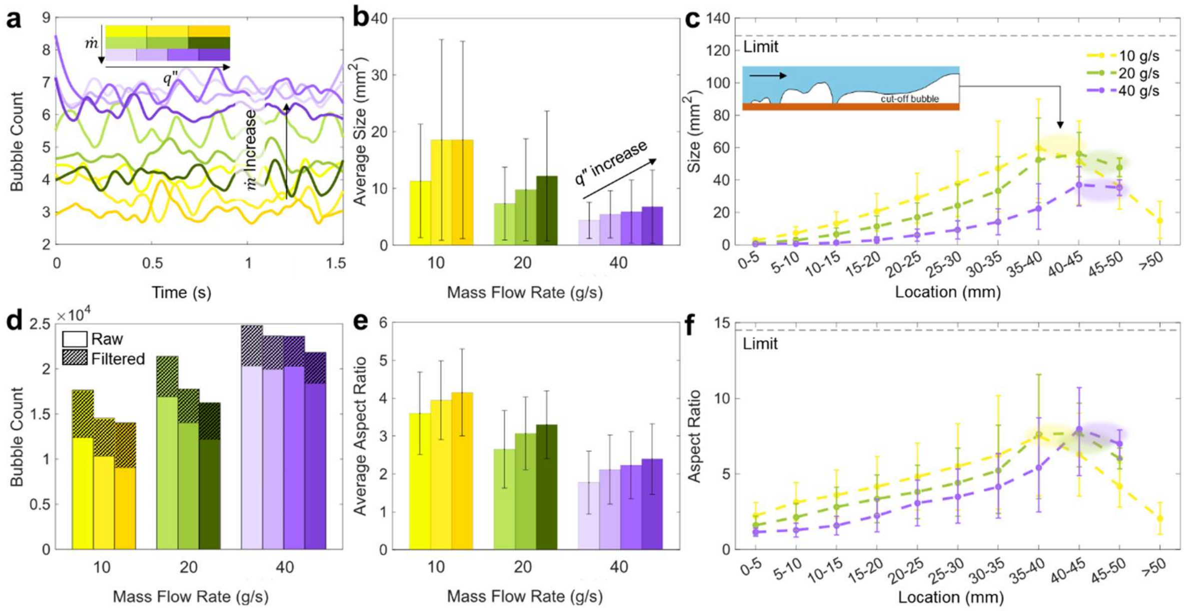

Figure 24. Spatial statistics. (a) Bubble count per frame with smoothed plot portrays individual bubbles that are identified and counted from 3,000 images of each frame. (b) The average bubble size decreases as the mass flow rate increases, indicating a quantitative competition between bubble growth and removal. (c) The local bubble sizes show an increasing trend until the cut-off point (insert) along the channel. Three lines represent average size of bubbles for each mass flow rate of 10, 20, and 40 g/s. (d) The accumulated total bubble counts from (a) range from 10,000 to 25,000 bubbles. In this study, elongated bubbles that reach the end of channels, cut-off bubbles, are filtered for the size and aspect ratio calculations. Filtered bubbles are represented in a plaid pattern, which is 30–35%, 20–25%, 16–18% for each mass flow rate. After the filtering process, total 155,000 bubbles are used for this study. (e) The average aspect ratio increases as the heat flux increases or the mass flow rate decreases. (f) The local aspect ratio also shows an increasing trend until the cut-off point. All error bars indicate the 16th and 84th percentile of the data set.

Taken together, these image-derived quantities establish a direct link between observable bubble features and underlying physical processes. Parameters such as void fraction, wetting front length, bubble velocity, and interfacial structure can be interpreted as indicators of wetting and dry-out dynamics at the heated surface. Conditions characterized by low void fraction, high bubble velocity, and strong wetting correspond to enhanced heat transfer performance. In contrast, conditions with high void fraction, reduced bubble mobility, and increased vapor coverage indicate degraded heat transfer and the onset of dry-out.

These observations suggest that both heat transfer enhancement and degradation can be interpreted through the evolution of interfacial dynamics. At moderate heat flux, active bubble departure and strong liquid replenishment lead to high heat transfer coefficients. As vapor accumulation increases, intermittent dry-out reduces heat transfer efficiency. Eventually, sustained vapor coverage leads to critical heat flux, where heat transfer collapses due to thermal insulation by the vapor layer.

This feature–physics relationship forms the foundation for the modeling approaches developed in the following sections. In particular, the extracted interfacial features are used to quantify wetting and dry-out dynamics for heat transfer coefficient prediction in Section 3.3, and to identify vapor accumulation mechanisms leading to critical heat flux in Section 3.4.

3.3 Vision-based Prediction of Heat Transfer Coefficient

Building upon the interfacial feature analysis presented in Section 3.1, this section develops a vision-based modeling framework for predicting the heat transfer coefficient (HTC) using image-derived descriptors of bubble dynamics. Rather than relying solely on conventional bulk parameters such as heat flux, wall temperature, and mass flow rate, the proposed approach leverages directly observed interfacial features to construct a mechanistic representation of boiling heat transfer.

In flow boiling systems, the heat transfer coefficient is strongly influenced by the balance between liquid replenishment and vapor coverage at the heated surface. Efficient heat transfer occurs when liquid continuously rewets the surface, sustaining microlayer evaporation and transient conduction. In contrast, the accumulation of vapor near the wall reduces liquid contact and introduces thermal resistance, ultimately degrading heat transfer performance. Therefore, accurately capturing the dynamics of wetting and dry-out is essential for predictive modeling of HTC.

The image-derived features extracted in this study provide direct quantification of these mechanisms. In particular, parameters such as wetting front length, vapor layer thickness, interfacial wavelength, void fraction, and bubble velocity collectively describe the spatial and temporal distribution of liquid and vapor phases. Among these, the wetting front length serves as a key indicator of liquid–solid contact, while vapor layer thickness and void fraction represent the extent of vapor coverage. Bubble velocity further characterizes the transport and removal of vapor structures along the channel. Together, these features form a physically interpretable feature space that captures the essential processes governing boiling heat transfer.

To translate these features into predictive capability, a vision-based modeling approach is adopted in which image-derived quantities are used to parameterize the effective heat transfer mechanisms. Instead of treating the model as a purely data-driven black box, physically meaningful relationships are incorporated to preserve interpretability and generalizability. In this framework, the heat transfer coefficient is modeled as a function of interfacial conditions that reflect the competition between wetting and dry-out processes.

Specifically, the contribution of liquid contact to heat transfer is associated with the extent of the wetting front, which promotes efficient heat removal through conduction and evaporation. Conversely, vapor-dominated regions introduce thermal resistance due to the low thermal conductivity of the vapor phase. By integrating these competing effects, the model captures the transition from efficient heat transfer regimes to degraded performance as vapor accumulation increases. This formulation enables a direct linkage between measurable visual features and macroscopic thermal behavior.

The effectiveness of the proposed approach lies in its ability to bridge the gap between observation and modeling. By grounding the model in physically interpretable features extracted from high-speed imaging data, the framework provides both predictive capability and mechanistic insight into boiling heat transfer. The following subsections present the detailed formulation of the model and its validation against experimental data obtained under microgravity flow boiling conditions.

3.3.1 Model Formulation

The heat transfer coefficient (HTC) model adopted in this study is based on a vision-based formulation that incorporates image-derived interfacial features into conventional boiling heat transfer modeling. Rather than relying solely on bulk flow parameters, this approach leverages spatial and temporal characteristics of vapor and liquid distributions obtained from high-speed visualization. The formulation builds upon prior work in which interfacial dynamics are explicitly linked to wall heat transfer behavior through measurable quantities such as wetting front length, vapor coverage, and void fraction.

Although numerous empirical correlations have been developed for flow boiling HTC prediction, most were formulated for specific working fluids, channel geometries, and operating conditions. Consequently, their predictive performance often deteriorates when applied outside their calibration range. More importantly, these correlations are generally expressed in terms of bulk variables such as mass flux, heat flux, vapor quality, and thermophysical properties, while only indirectly accounting for the local interfacial dynamics that actually govern wall heat transfer.

When applied to the present microgravity flow boiling configuration, several classical correlations provide reasonable estimates of average HTC, but none reproduce the experimentally observed downstream decline in heat transfer coefficient. This limitation arises because conventional models typically assume uniform surface wetting and quasi-steady boiling conditions, whereas the actual microgravity flow exhibits progressive vapor accumulation and shrinking wetting fronts along the heated wall.

In flow boiling, the heated surface is not continuously exposed to a single phase. Instead, the wall experiences intermittent exposure to vapor patches and liquid wetting fronts as interfacial structures evolve and propagate along the channel. This behavior is particularly pronounced under microgravity conditions, where buoyancy effects are suppressed and vapor structures remain attached to the surface for longer durations. As a result, a fixed location on the wall undergoes alternating dry and wet states, and the local heat transfer process must be interpreted in terms of time-varying surface exposure rather than spatially averaged bulk conditions alone.

Based on this physical interpretation, the total exposure time at the wall is defined as the sum of dry and wet periods,

$$t_{total} = t_{dry} + t_{wet} \tag{1}$$

where the dry period is given by

$$t_{dry} = \frac{L_{dry}}{u_g} \tag{2}$$

and the wet period is defined as

$$t_{wet} = \frac{L_{wet}}{u_f} \tag{3}$$

Here, L_{dry} represents the characteristic length of vapor-covered regions, and L_{wet} corresponds to the wetting front length. These quantities are directly obtained from image-based segmentation and interfacial analysis. The velocities u_g and u_f denote the vapor and liquid velocities, respectively. These velocities are not directly measured, but are estimated using energy-balance-based relations that incorporate the local heat flux, image-derived void fraction, and phase-change enthalpy terms. In this way, void fraction serves not only as a measure of vapor presence, but also as a bridge between visual phase distribution and phase transport behavior within the channel.

Using this time-scale decomposition, the effective heat transfer coefficient is expressed as a weighted combination of single-phase and two-phase contributions,

$$h_{eff} = \frac{t_{dry}}{t_{total}} h_{sp} + \frac{t_{wet}}{t_{total}} h_{tp} \tag{4}$$

In this formulation, h_{sp} represents the heat transfer coefficient associated with vapor-covered (dry) regions, while h_{tp} represents the contribution from liquid-contact (wetting) regions. The single-phase component h_{sp} is evaluated using established correlations depending on the flow regime, while the two-phase component h_{tp} is obtained from conventional flow boiling correlations. By combining these contributions through time-based weighting, the model reflects the actual wall-access behavior observed in the visualization data rather than assuming uniform phase exposure over the heated surface.

A key advantage of this formulation is that it augments conventional HTC correlations using measurable interfacial information extracted from visual data. In particular, it accounts for nonuniform vapor accumulation and the corresponding reduction in liquid wetting along the channel, which are not adequately represented in classical bulk-parameter-based models. Rather than replacing conventional correlations entirely, the present approach modifies them in a feature-informed manner, preserving their practical utility while improving their physical interpretability. This is particularly important in microgravity flow boiling, where the absence of buoyancy-driven bubble detachment enhances vapor persistence and intensifies the coupling between interfacial structure and heat transfer degradation.

Overall, the proposed HTC model establishes a direct connection between observable interfacial features and macroscopic heat transfer performance. By grounding the formulation in quantities extracted from high-speed visualization, it provides a more physically consistent framework for interpreting boiling heat transfer under microgravity conditions and offers improved predictive capability compared with purely empirical approaches.

3.3.2 Model Validation and Comparison

The predictive performance of the proposed heat transfer coefficient model is evaluated by comparing its results with experimental measurements and previously proposed empirical correlations.[51,55–58,64–67] Figure 25 presents representative comparisons for microgravity flow boiling cases at mass flow rates of 10.25 g/s and 19.76 g/s, corresponding to heat flux conditions near 76% and 77% of CHF, respectively. Although several conventional correlations provide reasonable agreement in terms of average magnitude, they generally fail to reproduce the experimentally observed variation in heat transfer coefficient along the flow direction. In particular, most of the existing models overpredict the local HTC and do not capture the progressive downstream reduction measured in the experiments.

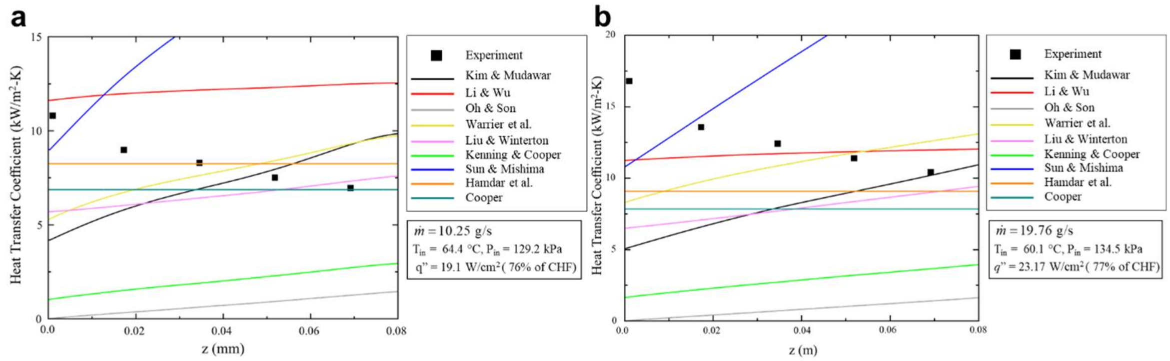

Figure 25. Heat transfer coefficient comparison. Comparison between experimental measurements and correlation predictions for (a) mass flow rate of 10.25 g/s with heat flux 76% of CHF, and (b) mass flow rate of 19.76 with heat flux 77% of CHF.

A key limitation of these classical correlations is that they are primarily formulated using terrestrial datasets and typically assume relatively uniform liquid coverage and quasi-steady boiling behavior. Under microgravity conditions, however, buoyancy-driven bubble detachment is largely suppressed, causing vapor structures to remain attached to the heated surface, slide downstream, and coalesce into larger vapor patches. As a result, liquid contact becomes progressively reduced and intermittent dry-out becomes more pronounced along the channel. These effects directly lower the local heat transfer coefficient, but are not adequately represented in conventional bulk-parameter-based formulations.

This limitation is further supported by the image-derived interfacial measurements shown in Figure 26 The wetting front ratio decreases systematically along the flow direction for all tested mass flow rates, indicating progressive loss of liquid contact with the heated wall. The downstream reduction in wetting is consistent with increasing vapor accumulation observed in the visualization data and provides direct evidence that the wall does not experience the uniform exposure implicitly assumed in classical correlations. Instead, the surface undergoes alternating wet and dry states whose balance changes continuously with position and operating condition.

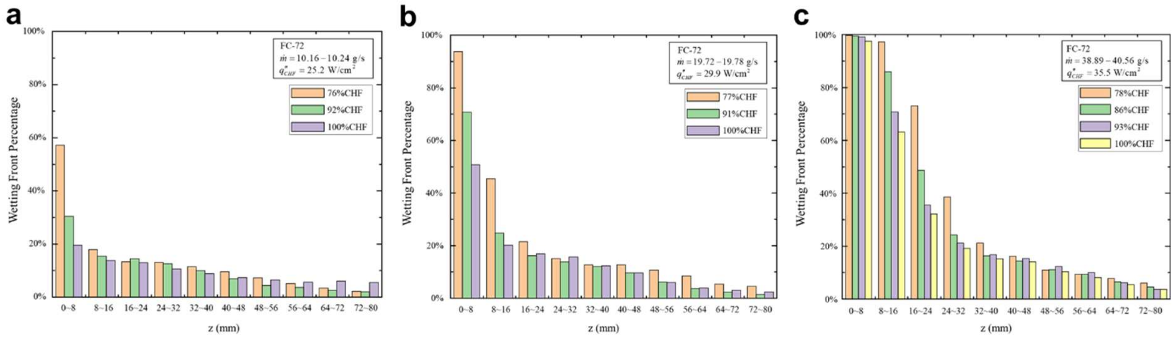

Figure 26. Wetting front ratios along the flow channel. Wetting front ratios are shown for each 8 mm segment of the flow channel at (a) 10 g/s, (b) 20 g/s, and (c) 40 g/s mass flow rates, illustrating the downstream reduction in liquid contact.

To account for this behavior, the revised formulation introduced in Section 3.3.1 incorporates image-derived wetting and dry-out descriptors through time-weighted contributions of liquid-contact and vapor-covered regions. Figure 27 shows that the revised model substantially improves agreement with experimental measurements. Unlike traditional correlations, which tend to predict constant or even increasing downstream HTC, the proposed model reproduces the measured spatial decline in heat transfer coefficient caused by growing vapor coverage and shrinking wetting fronts. This result demonstrates that incorporating surface exposure dynamics significantly improves both the physical consistency and predictive capability of the model.

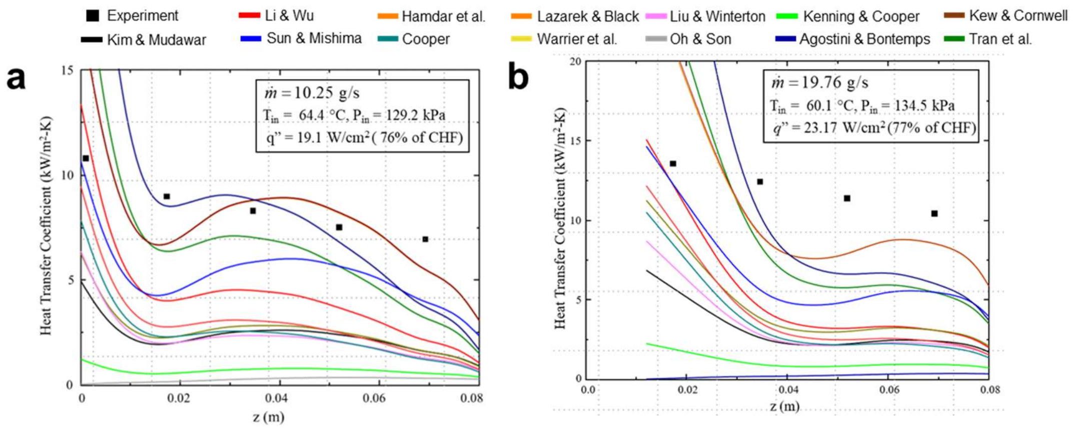

Figure 27. Comparison between revised model predictions and experimental measurements of local heat transfer coefficient (a) 10.25 g/s at 76% of CHF and (b) 19.76 g/s at 77% of CHF. The revised model captures the downstream reduction in HTC by incorporating image-derived wetting and dry-out dynamics.

Some discrepancy is observed near the inlet region, where the model assumes fully developed two-phase flow even though the liquid may still be partially subcooled and the onset of nucleate boiling is not explicitly resolved. Consequently, mismatch in this region is expected. However, once boiling is fully established, the revised formulation closely follows the measured data. At higher flow rates, the model continues to capture the correct downstream trend, although prediction error increases somewhat due to greater uncertainty in estimating vapor structures and phase-front velocities under conditions of stronger interfacial deformation and mixing. Despite these challenges, the revised model consistently provides lower error than the classical correlations across the tested dataset.

Overall, the validation results confirm that the vision-based formulation provides a more accurate and physically interpretable representation of boiling heat transfer than conventional empirical approaches. By combining image-derived interfacial features with a mechanistic time-weighted framework, the model is able to connect local wall exposure dynamics directly to macroscopic heat transfer performance. This feature-informed approach is especially valuable in microgravity flow boiling, where vapor persistence and non-uniform wetting dominate the thermal response and cannot be captured adequately by traditional assumptions.

3.4 Vision-Based Prediction of Critical Heat Flux

Critical heat flux (CHF) represents one of the most important operational limits in boiling heat transfer, marking the transition from efficient nucleate boiling to a degraded regime characterized by sustained surface dry-out and rapid deterioration of cooling performance. Once CHF is reached, liquid contact with the heated surface becomes severely restricted, causing a sharp rise in wall temperature and posing a significant risk of thermal failure. For this reason, accurate prediction of CHF remains a central challenge in the design of two-phase thermal management systems.

As discussed in Section 3.1, numerous theoretical models have been proposed to explain the onset of CHF, including the *Bubble Crowding Model, Boundary Sublayer Model, Boundary Layer Separation Model, Hydrodynamic Instability-based Model, and Interfacial Lift-off Model.* Although these models provide valuable physical interpretations, their validation has historically been limited by the lack of high-resolution measurements of interfacial quantities such as wetting front length, vapor blanket thickness, interfacial wavelength, and bubble clustering behavior. Consequently, many CHF models have relied on simplified assumptions or empirically assigned parameters rather than directly measured interfacial descriptors.

As established in the preceding sections, image-derived interfacial descriptors provide direct information on vapor accumulation, wetting, and dry-out behavior. These quantities make it possible to revisit classical CHF frameworks using experimentally resolved interfacial data rather than relying solely on bulk parameters or empirically assigned constants. In the present study, this opportunity is explored using microgravity flow boiling data, where CHF is strongly influenced by persistent vapor structures and reduced liquid replenishment at the heated surface. Building upon this foundation, the present section develops a vision-based framework for CHF prediction using interfacial features extracted from high-speed flow visualization. Rather than introducing a purely empirical predictive model, the approach adopted here revisits classical mechanistic CHF models using directly measured visual descriptors. Particular attention is given to formulations whose governing variables can be linked to image-derived quantities, enabling a more physically interpretable and experimentally grounded prediction of CHF

3.4.1 Model Formulation

To predict critical heat flux (CHF), the present study considers two mechanistic frameworks: the *Interfacial Lift-off Model* and the *Hydrodynamic Instability-based Model*. Among the classical CHF models discussed in Section 3.1, these two formulations are particularly suitable for the present analysis because their governing variables can be directly linked to interfacial quantities extracted from high-speed visualization, including wetting front length, vapor layer thickness, and interfacial wavelength. By incorporating image-derived inputs, both models can be reformulated in a feature-informed manner while preserving their original physical basis.

The *Interfacial Lift-off Model* describes CHF as a condition in which the momentum generated by vapor at the liquid-vapor interface exceeds the restoring force that maintains liquid contact with the heated surface. Once this balance is lost, the interface lifts away from the wall, producing sustained vapor coverage and initiating dry-out. In this sense, CHF is interpreted as an interfacially driven transition governed by the competition between vapor-induced lift-off and wall wetting. Based on this framework, CHF is expressed as

$$q''_{CHF} = \rho_g\left(c_{p,f}\Delta T_{sub,in}+h_{fg}\right)\left[\frac{4b\pi\sigma\sin(b\pi)}{\rho_g}\right]^{\frac{1}{2}}\delta^{\frac{1}{2}}\lambda_c\;|_{z^*} \tag{5}$$

where ρ_g is the saturated vapor density, $c_{p,f}$ is the liquid specific heat, $\Delta T_{\mathrm{sub,in}}$is the inlet subcooling, h_{fg} is the latent heat of vaporization, and $\sigma$is the surface tension. The quantities δ, λ_c, and b represent the vapor layer thickness, the critical wavelength, and the wetting front ratio, respectively.

A key limitation of the classical formulation is that the wetting front ratio is commonly treated as a constant, typically $b = 0.2$, irrespective of operating condition. This assumption neglects the fact that both wetting front length and wavelength evolve continuously with heat flux, mass flow rate, and local interfacial dynamics. Under such conditions, a fixed value of b can obscure the actual relationship between vapor accumulation and liquid-wall contact.

To address this limitation, the present study replaces the constant wetting front ratio with an image-derived quantity obtained from the interfacial features introduced in Section 3.2. Specifically, the wetting front ratio is defined as:

$$b = \frac{w_{tot}}{\lambda_{tot}} \tag{6}$$

where w_{tot} is the total wetting front length and λ_{tot} is the corresponding total wavelength, both extracted from segmented high-speed image data. In the same manner, the vapor layer thickness δ and the critical wavelength λ_c are obtained directly from image-derived interfacial measurements. This allows the CHF model to incorporate spatially resolved physical descriptors rather than relying on empirically prescribed constants.

The *Hydrodynamic Instability-based Model* predicts CHF by analyzing the growth of interfacial instabilities that hinder liquid rewetting of the heated surface. This model considers the development of wave-like disturbances along the vapor-liquid interface and evaluates when these instabilities become strong enough to trap vapor near the wall and induce dry-out. The CHF is expressed as:

$$q''_{CHF} = \rho_g h_{fg} \frac{\pi}{16} \left(\frac{4\sigma}{\lambda_c}\right)^{\frac{1}{2}} \left[\frac{\left(\frac{\rho_f+\rho_g}{\rho_f \rho_g}\right)^{\frac{1}{2}}}{\left(1+\frac{\rho_g}{\rho_f}\frac{\pi}{16-\pi}\right)} \right] \tag{7}$$

where ρ_f and ρ_g are the densities of the saturated liquid and vapor, respectively, σ is the surface tension, λ_c is the critical wavelength of interfacial instability. In this work, λ_c is extracted from segmented bubble contours and wave-like vapor structures observed in flow-parallel image sequences, providing a physically grounded input to the model.

Figure 28 presents the spatial variation of vapor wavelength at CHF, showing the downstream evolution of vapor wavelengths along the channel for three flow rates. This result supports the use of image-derived wavelength as a physically meaningful parameter for CHF prediction and highlights the condition-dependent nature of interfacial instability in microgravity flow boiling.

Taken together, these two models capture complementary mechanisms underlying the initiation of CHF. The *Interfacial Lift-off Model* emphasizes local interfacial momentum and vapor expansion near the wetting front, whereas the *Hydrodynamic Instability-based Model* focuses on the evolution of vapor-liquid interfacial waves and their effect on liquid replenishment. By incorporating image-derived measurements into these mechanistic formulations, the present study aims to provide more physically interpretable and experimentally grounded predictions of CHF under microgravity flow boiling conditions. Model performance is evaluated in the following section through direct comparison with experimentally measured CHF values.

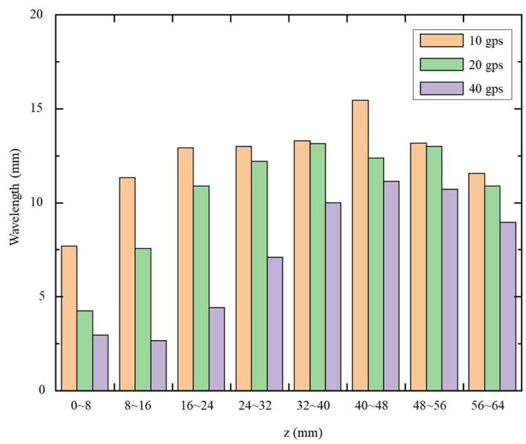

Figure 28. Spatial variation of vapor wavelength at CHF. Downstream evolution of vapor wavelengths along the channel for three flow rates at critical heat flux.

3.4.2 Model Validation Using Image-Derived Features

The performance of the feature-informed CHF model is evaluated by comparing its predictions with experimental CHF measurements and with predictions obtained from the classical *Interfacial Lift-off Model*. Using the image-derived interfacial parameters defined in Section 3.4.1, the model is validated across the tested microgravity flow boiling conditions.

The validation results confirm that replacing the classical constant-b assumption with image-derived interfacial quantities improves CHF prediction. In the conventional formulation, b is typically fixed at 0.2, which implies that the wetting front length is always 20% of the wavelength at CHF, regardless of operating condition. However, the experimental results indicate that this ratio varies with flow condition and interfacial structure. By using measured values of b, together with image-derived δ and λ_c, the revised model becomes more responsive to the actual vapor-liquid configuration in the channel.

To assess model performance, predictions from both the *Interfacial Lift-off* and *Hydrodynamic Instability-based models* are compared with experimentally measured CHF values across a range of mass fluxes as shown in Table 3. In each case, image-derived features such as vapor layer thickness, critical instability wavelength, and wetting front ratio are used as direct inputs. This approach eliminates the need for empirical constants and allows each model to reflect local interface characteristics extracted from high-speed visual data.

Table 3. Experimental data and model predictions for CHF .

Mass flow rate (g/s)	10	20	40
Experimental measurement (W/cm^2)	28.8	34.2	40.6
Original Interfacial Lift-off Model (W/cm^2)	34.2	31.8	32.1
Revised Interfacial Lift-off Model (W/cm^2)	8.5	15.3	35.1
Original Hydrodynamic Instability-based Model (W/cm^2)	22.4	25.0	29.6
Revised Hydrodynamic Instability-based Model (W/cm^2)	25.9	36.5	36.1

The results indicate that both models reproduce the order of magnitude and overall trend of CHF across varying flow conditions. However, the *Hydrodynamic Instability-based Model* consistently shows closer agreement with experimental data, particularly at higher mass flow rates where interfacial dynamics are more fully developed. By capturing both capillary and inertial influences through the critical wavelength, this model is more responsive to changes in vapor structure and phase distribution. Its predictions follow the experimentally observed increase in CHF with increasing flow rate and demonstrate reduced error when vision-derived wavelengths are used in place of assumed values.

The remaining discrepancy at lower mass flow rates can be explained, at least in part, by limitations in data acquisition. In particular, the viewing window effect introduces uncertainty in the measurement of interfacial wavelength for end bubbles, cut-off bubbles, continuous vapor structures, and elongated bubbles. This effect becomes more pronounced at lower mass flux, where larger and more extended vapor structures are more likely to intersect the edge of the imaging window. As a result, the computed wavelength and wetting front statistics may deviate from their true values, which in turn affects the calculated b parameter and CHF prediction. This limitation is especially relevant in low-flow-rate conditions, where elongated and partially visible vapor structures occupy a larger fraction of the observable field of view.

This interpretation is also consistent with the interfacial feature trends presented in Section 3.2. The spatial analysis of wetting front ratio, vapor layer thickness, and interfacial wavelength shows that these quantities vary significantly with mass flow rate and heat flux, confirming that CHF-relevant interfacial conditions are inherently non-uniform and condition-dependent. Such variations are neglected in the classical formulation when b is prescribed as a constant, but are partially recovered in the feature-informed model through direct measurement from the visual data. Similarly, the use of image-derived wavelength in the *Hydrodynamic Instability-based Model* allows the instability criterion to reflect the actual spatial evolution of vapor structures rather than an assumed representative scale.

Overall, these results demonstrate that incorporating image-derived interfacial features into the *Interfacial Lift-off Model* leads to a more physically grounded prediction of CHF, while the remaining error at lower mass flow rates highlights the importance of wider imaging windows and improved post-processing for future refinement. More broadly, the comparison between the two mechanistic models shows that vision-derived interfacial descriptors can improve CHF prediction by replacing empirically fixed parameters with experimentally resolved quantities. In this way, the present framework establishes a more direct connection between interfacial dynamics and CHF behavior under microgravity flow boiling conditions.

3.5 Conclusion

This chapter develops a vision-based heat transfer modeling framework using image-derived flow boiling features. Building on the vision-based digitization framework introduced in Chapter 2, high-speed flow visualization data are converted into quantitative descriptors of bubble dynamics, phase distribution, wetting behavior, and vapor accumulation. The analysis focuses on microgravity flow boiling conditions, where suppressed buoyancy promotes prolonged bubble residence, enhanced coalescence, and persistent vapor structures near the heated surface.

The image-derived feature analysis demonstrates that local thermal behavior is strongly linked to the spatial and temporal evolution of vapor and liquid structures. Void fraction, wetting front length, interfacial wavelength, vapor layer thickness, and bubble velocity provide complementary information about vapor accumulation, liquid replenishment, and dry-out development. In particular, the downstream increase in vapor fraction and the reduction in wetting-related descriptors indicate progressive loss of liquid contact along the heated channel. These trends show that visual descriptors can provide direct physical insight into mechanisms that are difficult to infer from bulk measurements alone.

A vision-based HTC model is developed by incorporating image-derived wetting and dry-out behavior into a time-weighted heat transfer formulation. Rather than assuming uniform surface exposure, the model represents the heated wall as alternating between vapor-covered and liquid-wetted states. The resulting formulation links dry and wet exposure times to image-derived vapor and wetting lengths, allowing local heat transfer degradation to be interpreted through the balance between vapor coverage and liquid contact. Compared with classical correlations, the revised model better captures the downstream decline in local heat transfer coefficient observed under microgravity flow boiling conditions.

This chapter also applies image-derived interfacial descriptors to critical heat flux prediction. Two mechanistic CHF frameworks, *the Interfacial Lift-off Model* and the *Hydrodynamic Instability-based Model*, are revisited using visual measurements of wetting front ratio, vapor layer thickness, and critical wavelength. Replacing fixed or assumed parameters with experimentally extracted descriptors allows the models to reflect condition-dependent vapor structures and interfacial instability scales. The *Hydrodynamic Instability-based Model* shows closer agreement overall with the experimental CHF measurements, particularly at higher mass flow rate, while remaining discrepancies at lower mass flow rate are associated in part with viewing-window limitations and uncertainty in measuring elongated or cut-off vapor structures.

Overall, the results demonstrate that image-derived features provide a useful bridge between visual observation and boiling heat transfer modeling. By incorporating directly measured interfacial descriptors into HTC and CHF frameworks, the analysis improves physical interpretability and reduces reliance on empirically fixed assumptions. Although the present validation is based on microgravity flow boiling datasets and should be extended to broader operating conditions, the approach establishes a foundation for feature-informed heat transfer modeling in two-phase flow systems. This chapter therefore links the vision-based measurements developed in Chapter 2 to vision-based modeling of boiling performance, while the following chapters extend visual sensing toward event-based activity analysis and real-time flow regime classification.

CHAPTER 4: Event-Based Activity Descriptors for Flow Boiling Diagnostics

4.1 Introduction

The previous chapter uses high-speed imaging, Mask R-CNN-based segmentation, and KD-tree-based tracking to extract bubble-level descriptors for flow boiling heat transfer analysis. This frame-based approach provides direct information on bubble morphology and motion, including bubble size, shape, count, centroid location, trajectory, and velocity. These image-derived descriptors are useful for linking local bubble behavior with macroscopic heat transfer performance and critical heat flux characteristics. Conventional high-speed imaging has therefore been widely used to visualize bubble morphology and vapor structure evolution in boiling flows. When combined with image processing and tracking methods, frame-based images provide intuitive and physically meaningful information about liquid-vapor interfacial behavior.[7,8,68]

However, high-speed imaging records dense image frames at fixed sampling intervals, including static background regions and slowly varying areas that may contain limited dynamic information.[69] This produces substantial data redundancy, especially when high frame rates are required to capture rapid two-phase flow dynamics. In addition, extracting reliable quantitative features from boiling images typically requires segmentation, tracking, and post-processing. Although this workflow is effective for morphology-based analysis, it can be computationally demanding when applied to long-duration recordings or real-time monitoring tasks. These challenges become more pronounced because liquid-vapor interfaces often exhibit irregular shapes, reflections, overlapping structures, rapid deformation, and changing contrast.

Flow boiling is governed by transient and localized liquid-vapor activity. Bubble growth, coalescence, sliding, elongation, vapor redistribution, and intermittent dryout-related behavior occur over short time and length scales. Although conventional high-speed images provide direct visualization of these processes, the full-frame acquisition strategy does not selectively emphasize the most dynamically active regions of the flow. Therefore, a complementary sensing approach is needed to capture dynamic flow boiling activity with reduced data redundancy and improved temporal responsiveness.

Neuromorphic event cameras provide an alternative strategy for sensing dynamic visual information. Unlike conventional cameras that record full image frames at fixed intervals, event cameras asynchronously detect pixel-level brightness changes and generate sparse event streams with precise timestamps.[70–72] Each event represents a local intensity change at a specific pixel location and time, rather than a complete image of the scene. This sensing mechanism reduces redundant background information, preserves fine temporal features, minimizes motion blur, and enables low-power continuous operation. In flow boiling, where rapid interfacial motion occurs within a largely stationary experimental background, event-based sensing naturally emphasizes dynamic structures such as moving bubble boundaries, vapor-liquid interface motion, bubble deformation, coalescence, and rapid phase redistribution.

Despite these advantages, the use of event cameras for quantitative flow boiling analysis remains relatively unexplored. Most boiling visualization studies rely on conventional high-speed images, while event camera studies have mainly focused on motion detection,[73,74] robotics,[75,76] autonomous vision,[77,78] and general dynamic scene analysis.[79] For flow boiling applications, it remains necessary to establish how sparse event streams can be transformed into physically interpretable descriptors of two-phase activity under changing operating conditions. Rather than using event data to directly measure bubble morphology or replace high-speed imaging, this chapter treats the event stream as a compact representation of brightness-change activity generated by evolving two-phase structures.

This chapter investigates the use of event-camera measurements for activity-based analysis of flow boiling dynamics. The event stream is converted into temporal and spatial representations to quantify event intensity, event rate fluctuation, burst-like activity, temporal persistence, spatial coverage, spatial dispersion, and streamwise distribution. Specifically, the analysis includes event rate signals, relative event rate fluctuation, normalized event-density maps, high-density coverage ratio, spatial entropy, and streamwise event-density profiles. These event-derived descriptors are used to examine how interfacial activity evolves with heat flux and mass flow rate.

The objective of this chapter is to establish an event-based descriptor framework that connects sparse neuromorphic measurements with physically meaningful flow boiling activity. The event-derived descriptors are integrated into a PCA-based activity regime map that summarizes changes in interfacial activity across operating conditions. Representative descriptors are also evaluated for pressure drop prediction to examine their connection to measurable thermofluidic behavior. This analysis provides an intermediate step between frame-based image analysis and real-time event-driven classification. By demonstrating that event streams contain systematic temporal and spatial information about flow boiling dynamics, this chapter highlights the potential of event cameras as complementary diagnostic tools for dynamic two-phase flows, particularly where reduced data redundancy, high temporal sensitivity, and real-time monitoring capability are needed. The resulting event-based activity representation provides the foundation for the real-time flow regime classification framework developed in Chapter 5.

4.2 Event-Based Sensing Principle and Descriptor Framework

This section presents the event-based sensing principle and descriptor framework used to analyze flow boiling activity. In contrast to the high-speed imaging approach used in the previous chapter, which records full image frames at fixed sampling intervals, neuromorphic event cameras operate asynchronously and record only local brightness changes at individual pixels. This sensing mechanism generates sparse event streams with high temporal resolution and low data redundancy, making event cameras suitable for capturing rapidly evolving activity in two-phase flow boiling.

Conventional high-speed imaging records the boiling process as a sequence of full intensity frames, $I(x, y, t)$, where I is the image intensity at pixel location (x, y) and frame time t. This frame-based approach provides direct visual information on bubble morphology, vapor structure, and flow development. However, because the entire field of view is recorded at every frame, high-speed imaging also captures static background regions and slowly varying areas that may contain limited dynamic information. This leads to substantial data redundancy, particularly when high frame rates are required to resolve rapid liquid-vapor motion.

Event cameras provide a complementary sensing approach by recording only local brightness changes. Instead of acquiring dense image frames at fixed time intervals, an event camera generates an event when the change in logarithmic intensity at an individual pixel exceeds a predefined contrast threshold. Each event is represented as (x_i, y_i, p_i, t_i), where x_i and y_i are the pixel coordinates, t_i is the timestamp, and p_i is the polarity indicating whether the local brightness increases or decreases. Depending on the sign of the brightness change, the event is assigned either positive or negative polarity. In flow boiling, these brightness changes are associated with moving bubble boundaries, vapor-liquid interface motion, bubble deformation, coalescence, and rapid phase redistribution.

The advantages of this sensing modality are illustrated in Figure 29, which compares the operating principles and system-level performance of high-speed and event-based cameras. Event cameras emit asynchronous brightness-change events at each pixel and therefore capture motion-driven visual changes rather than continuously recording the entire image field. This sparsity substantially reduces memory usage, power consumption, and bandwidth relative to conventional high-speed imaging. For example, a 5 s recording at 2,000 frames per second using a conventional high-speed camera can require approximately 1.2 GB of data and about 55 W of power, whereas a comparable event camera recording can be reduced to approximately 150 MB with a power consumption of about 4.5 W. These characteristics make event cameras attractive for continuous monitoring and low latency diagnostics in dynamic thermal-fluid systems. The key differences between the two imaging modalities are summarized in Table 4. High-speed cameras provide dense frame-based visual information that is well suited for morphology-based analysis, such as segmentation, tracking, and bubble-size measurement. In contrast, event-based cameras generate sparse asynchronous event streams only when local brightness changes occur. This distinction makes event-based cameras less suited for direct morphology measurement, but more suitable for capturing rapid dynamic activity with reduced data volume, low bandwidth, and low latency. Therefore, the two imaging approaches are treated as complementary tools in this dissertation: high-speed imaging is used for bubble morphology and feature extraction, while event-based imaging is used for activity analysis and real-time diagnostic development.

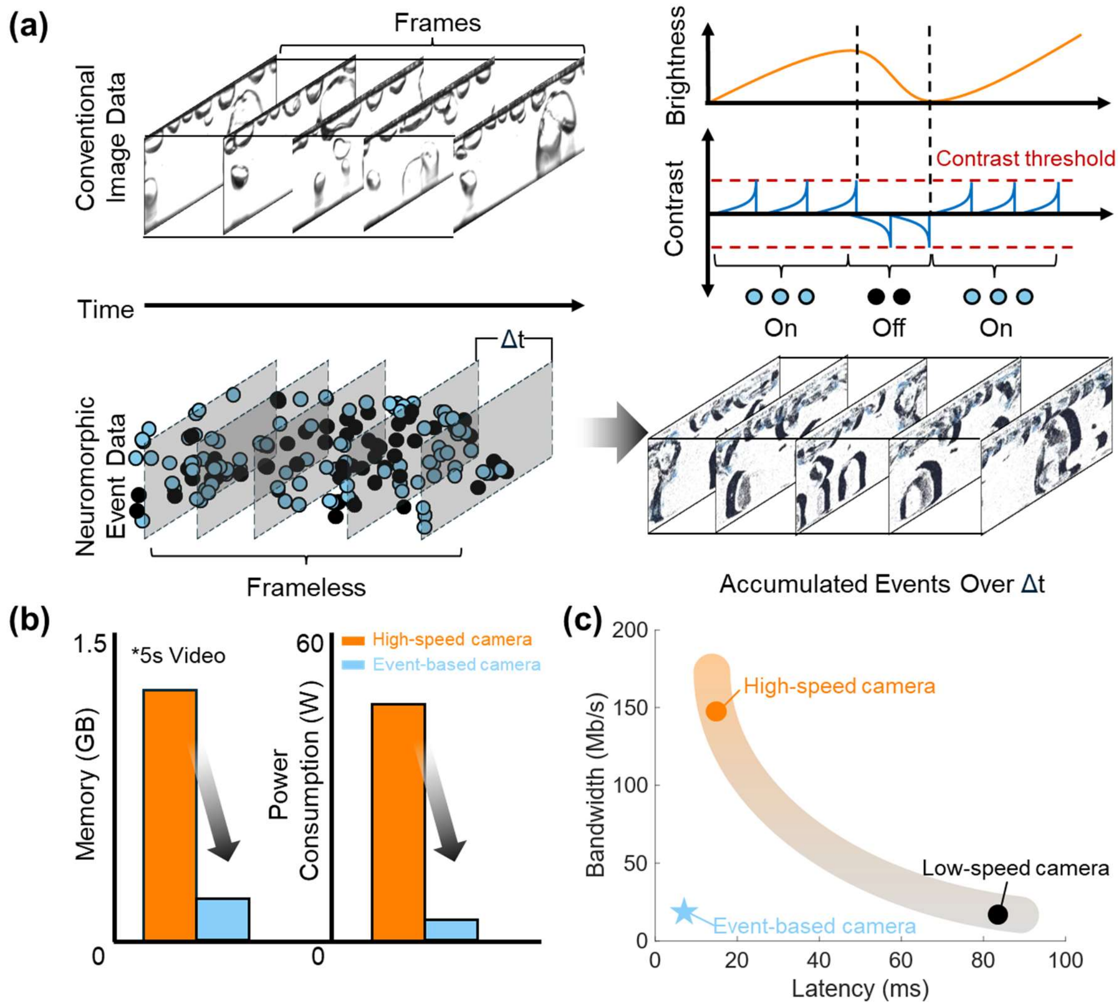

Figure 29. Comparison of high-speed and event cameras for flow boiling analysis. (a) Event cameras emit asynchronous brightness change events at each pixel, capturing motion only and enabling sparse frame reconstruction over a chosen time window (Δt). (b) This sparsity greatly reduces resource use. A 5-s recording at 2000 frames per second (fps) decreases from roughly 1.2 GB and 55 W (FASTCAM Mini AX100) to about150 MB and 4.5 W (Prophesee EVK3). (c) Sub-millisecond latency and a 45 fps-

equivalent data rates give event cameras responsiveness comparable to a 5000 fps system while keeping the computational load low.

Table 4. Comparison of high-speed and event-based cameras.

Feature	High-speed Camera	Event-based Camera
Latency	~0.1–1 ms (frame-based)	~1–10 μs (asynchronous)
Bandwidth	Dense (hundreds of MBps–GBps)	Sparse (kbps–Mbps)
Data generation	Constant, even if static	Only on change
Ideal for	Offline analysis, detailed frames	Real-time, fast motion

It is important to distinguish event-based sensing from conventional morphology-based image analysis. Event camera data do not directly represent void fraction, vapor volume, or bubble shape. Instead, event streams provide a motion- and contrast-sensitive representation of brightness-change activity. A high event density indicates strong local visual activity, which may be associated with moving vapor structures, bubble deformation, coalescence, or rapid phase redistribution. Therefore, in this chapter, event data are not used to replace high-speed images for bubble morphology measurement. Instead, they are used to quantify dynamic flow boiling activity through temporal and spatial descriptors.

Figure 30 summarizes the event-based descriptor framework used in this chapter. As shown in Figure 30a, the asynchronous event stream is accumulated into short time bins to generate image-like event frames and a time-binned event rate signal. Figure 30b shows that temporal and spectral descriptors are extracted from the event rate signal, including mean event rate, relative event rate fluctuation, and spectral entropy. Figure 30c illustrates the spatial descriptor framework, where events are accumulated over the observation window to construct a globally scaled event-density map. From this map, high-density coverage ratio and spatial entropy are calculated to quantify the spatial extent and dispersion of event activity. Finally, Figure 30d shows how operating conditions and selected event-derived descriptors are evaluated as inputs to a multilayer perceptron for pressure drop prediction.

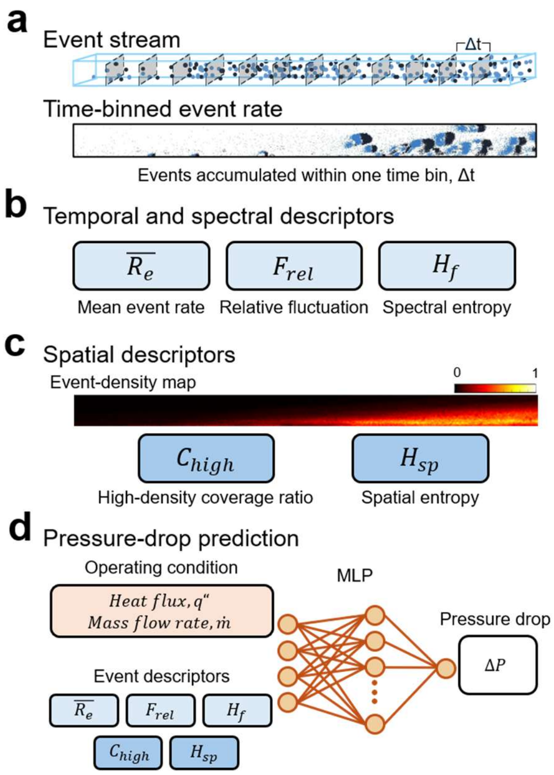

Figure 30. Event-based descriptor framework for flow boiling activity analysis.
(a) The event stream is accumulated into short time bins to generate image like event frames and a time binned event rate signal. (b) Temporal and spectral descriptors are extracted from the event rate signal, including mean event rate, relative event rate fluctuation, and spectral entropy. (c) Events are accumulated over the observation window to construct a globally scaled event density map, from which high-density coverage ratio and spatial entropy are calculated. (d) Operating conditions and selected event derived descriptors are evaluated as inputs to a multilayer perceptron for pressure drop prediction.

Following the event-based sensing principle described above, the asynchronous event stream is converted into a time-binned event rate signal for temporal analysis. Because raw event data are not organized as conventional image frames, events are accumulated within short time intervals using a selected bin width, Δt. Each time bin represents the brightness-change activity occurring within the selected region of interest during that interval.

The event rate is calculated by counting the number of events in each bin and normalizing it by the bin duration:

$$R_e(t_k) = \frac{N_e(t_k)}{\Delta t} \tag{8}$$

where t_k is the start time of the *k*-th time bin, and $N_e(t_k)$ is the total number of events occurring within the selected region of interest during that bin. The event count is summed over all spatial locations (x, y) and both event polarities. In this study, a bin width of Δt = 5 ms is used to capture short time-scale event activity while maintaining a sufficiently smooth event rate signal. The sensitivity of the temporal descriptors to the selected bin width is evaluated in the supplementary analysis.

The condition-level mean event rate is calculated as the temporal average of $R_e(t)$ over the observation window and is denoted by $\bar{R_e}$. The relative event rate fluctuation is calculated as the coefficient of variation of the event rate signal:

$$F_{rel} = \frac{\sigma_{R_e}}{\bar{R_e}} \tag{9}$$

where σ_{R_e} and $\bar{R_e}$ are the standard deviation and mean of the event rate signal, respectively. This metric quantifies the strength of temporal fluctuation relative to the mean event activity. A high

F_{rel} indicates that event generation is concentrated into intermittent high-amplitude intervals, whereas a low F_{rel} indicates a more sustained event response over the observation window

To examine the temporal structure of the event rate signal beyond condition-averaged descriptors, frequency-domain descriptors are extracted from the Fourier spectrum of $R_e(t)$. Before the Fourier transform, the mean event rate is subtracted, and a Hann window is applied to reduce spectral leakage caused by the finite recording window. The single-sided FFT amplitude spectrum is denoted as $A(f)$.

The normalized spectral entropy of the event rate signal is defined using the normalized Shannon entropy form[80–82], applied here to the FFT amplitude distribution, and is calculated as:

$$H_{f,n} = -\frac{\sum_i p_i \log(p_i)}{\log N_f} \tag{10}$$

where

$$p_i = \frac{A(f_i)}{\sum_j A(f_j)} \tag{11}$$

and N_f is the number of frequency components included in the selected frequency range. Here, p_i is the normalized amplitude weight of the i-th frequency component, while j is a summation index used to calculate the total FFT amplitude over all frequency components in the selected range. Spectral entropy quantifies how broadly the event rate fluctuation spectrum is distributed across frequencies. A low value indicates that the event rate fluctuation is concentrated around a limited number of frequency components, whereas a high value indicates broadband, multi-frequency temporal activity. Therefore, f_c and H_f provide frequency-domain descriptors of event-generating interfacial motion.

For spatial analysis, events are accumulated over a selected time window to construct an event density map. The event count at each pixel location is normalized as:

$$\widetilde{D}(x,y) = \frac{D(x,y)}{D_{max,all}} \tag{12}$$

where $D(x,y)$ is the number of events occurring at pixel location (x,y) during the 3 s accumulation window and $D_{\mathrm{max,all}}$ is the maximum raw event density observed across all pixel locations and all tested operating conditions. Thus, $\widetilde{D}(x,y)$ is a globally scaled event-density map with values between 0 and 1.

The high-density coverage ratio is defined as

$$C_{high} = \frac{A(\widetilde{D}(x,y) > \theta)}{A_{\mathrm{window}}} \tag{13}$$

where $A(\widetilde{D}(x,y) > \theta)$ is the area occupied by pixels with scaled event density greater than the threshold θ, and A_{window} is the total area of the observation window. Because C_{high} is an area fraction, it is inherently bounded between 0 and 1. The observed values are substantially smaller than unity because highly active event regions occupy only a limited portion of the observation window.

In the present analysis, the threshold θ = 0.5 is used as a stringent threshold to identify regions with event density greater than 50% of the global maximum density observed across all tested conditions. The sensitivity to the selected threshold is evaluated in the *Appendix*.

Spatial entropy is calculated from the event-density distribution using Shannon entropy and normalized by $\ln(N_{\text{pix}})$, which corresponds to the maximum possible entropy for N_{pix} pixel locations.

$$H_{sp} = -\frac{\sum_{m=1}^{N_{pix}} w_{m,sp} \ln(w_{m,sp})}{\ln(N_{pix})} \tag{14}$$

where $w_{m,sp}$ is the fraction of the total event density contained at the m-th pixel location, and N_{pix} is the total number of pixels within the region of interest. Here, the region of interest is defined as the region above the 10 cm heated section, where boiling-induced interfacial motion and brightness-change activity are most directly associated with wall heating. Division by $\ln(N_{pix})$bounds H_{sp} between 0 and 1. A lower H_{sp} indicates localized event activity, whereas a higher H_{sp} indicates a more spatially distributed event-density pattern.

Pressure drop prediction is performed to evaluate whether event-derived descriptors provide information relevant to the thermofluidic response beyond the imposed operating conditions. A multilayer perceptron (MLP) model is used to predict the measured time-averaged pressure drop from different combinations of operating variables and event-derived descriptors.

Four input-feature groups are evaluated: operating conditions only, event-derived descriptors only, operating conditions combined with temporal instability descriptors, and operating conditions combined with all selected event-derived descriptors. The *operating variables* are mass flow rate, $\dot{m}$ and heat flux, q''. The *event-derived descriptors* include the mean event rate, $\overline{R_e}$, relative event rate fluctuation, F_{rel}, high-density coverage, C_{high}, spatial entropy, H_{sp}, and spectral entropy, H_f, depending on the tested feature group.

The operating-only model serves as the baseline, the event-only model evaluates whether event-derived descriptors alone contain pressure-relevant information, the operating plus temporal instability descriptor model tests the added value of F_{rel}, and H_f beyond operating conditions, and the operating plus all event descriptor model evaluates whether the broader descriptor set further improves prediction or introduces redundant variables.

The MLP consists of an input layer, two fully connected hidden layers with rectified linear unit (ReLU) activation functions, and a single linear output neuron for pressure drop regression. Candidate hidden-layer architectures of [8, 4], [12, 6], and [16, 8] are evaluated within each leave-one-out cross-validation fold, where each pair represents the number of neurons in the first and second hidden layers. All predictor variables are standardized using the training data within each fold to prevent variables with larger numerical ranges from dominating the learning process. The hidden-layer architecture is selected using training-data validation within each fold, allowing the model to remain compact while capturing nonlinear relationships between operating conditions, event-derived temporal unsteadiness, and pressure drop response.

In this analysis, relative event rate fluctuation, F_{rel} represents the amplitude of temporal variation in the event rate signal, while spectral entropy, H_f characterizes the spectral distribution and degree of frequency-domain spreading of the event rate fluctuations. These descriptors are selected because they are expected to reflect local interfacial unsteadiness associated with pressure drop variation. The measured pressure drop standard deviation is used to represent condition wise pressure drop fluctuation. Prediction uncertainty is estimated from the spread of predictions obtained from the tested MLP candidate architectures within each leave one out cross validation fold. A full comparison of the tested MLP models, together with the the Ridge regression[86] baseline is provided in the *Appendix.*

The descriptor framework is then applied to event-camera measurements acquired from the closed-loop flow boiling facility described in Chapter 1. Experiments are performed at mass flow rates of 12, 15, and 18 g/s, with eight heat flux conditions for each mass flow rate: 10.7, 13.92, 16.27, 20.04, 22.74, 26.98, 29.98, and 34.70 W/cm^2. A fixed region of interest and identical processing procedure are used across all cases to enable consistent comparison of event activity. The following sections examine the temporal, spatial, and streamwise characteristics of the resulting event response.

This chapter therefore focuses on event-based activity characterization rather than direct morphology measurement or flow regime classification. By demonstrating that sparse event streams contain systematic information about flow boiling activity, the analysis provides a foundation for the real-time event-driven flow regime classification framework developed in Chapter 5.

4.3 Temporal and Spatial Event Activity Descriptors

4.3.1 Temporal Event Activity

The temporal characteristics of event activity are first examined to evaluate how the event response changes with heat flux and mass flow rate. Since the event camera records asynchronous brightness-change events, the time-binned event rate signal provides a direct measure of how rapidly event-generating activity occurs within the selected region of interest.

Figure 31a shows representative event-accumulated visualizations for each operating condition, arranged by increasing heat flux and by mass flow rate. These images provide a qualitative overview of how event-generating interfacial activity changes with heat flux and mass flow rate. As heat flux increases, the event activity becomes more pronounced and spatially extended, indicating stronger brightness-change activity associated with bubble motion, vapor-interface deformation, and interfacial redistribution.

The corresponding total event counts accumulated over a 3 s recording period are shown in Figure 31b. Error bars represent within-recording temporal variability estimated by dividing each 3 s recording into six non-overlapping 0.5 s sub-windows and converting each sub-window count to an equivalent 3 s total count. For all mass flow rates, the total number of events increases with heat flux, demonstrating that stronger wall heating produces more intense event activity. The error bars are smaller than the overall heat-flux-dependent increase, indicating that the increasing event-count trend is preserved even when temporal variability within each recording is considered. The increase is most pronounced at the lower mass flow rate, where event activity becomes more broadly distributed over the imaging window. In contrast, the higher mass flow rate case exhibits a lower total event count within the observation window. Rather than directly indicating suppressed nucleation, this lower count may reflect shorter residence time of bubbles and vapor interfaces due to stronger convective transport, which moves event-generating structures more rapidly through or beyond the observed region.

Figure 31c shows the mean event rate calculated from the time-binned event rate signal within each 3 s recording. Error bars represent the standard deviation of the time-binned event rate signal within each recording, indicating within-recording temporal fluctuation rather than independent repeated-trial uncertainty. The mean event rate increases with heat flux for all mass flow rates, consistent with the total event-count trend in Figure 31b. Physically, this increase indicates more frequent optical intensity changes caused by liquid-vapor interfacial dynamics, including bubble growth, departure, interface deformation, and vapor redistribution. The response also depends on mass flow rate. The lower mass flow rate cases generally show stronger event activity than the 18 g/s case, suggesting that slower convective transport allows event-generating vapor and interface structures to remain longer within the observation window.

Figure 31d shows the relative event rate fluctuation, defined as the coefficient of variation of the time-binned event rate signal. Error bars represent the standard deviation of relative event rate fluctuation values calculated from six non-overlapping 0.5 s sub-windows within each 3 s recording. Unlike the mean event rate, the relative fluctuation generally decreases as heat flux increases. This indicates that the event rate signal becomes less dominated by isolated high-amplitude fluctuations and more continuously active over time. The decrease in relative fluctuation suggests that the event response transitions from sparse, intermittently fluctuating activity toward more sustained interfacial activity as heat flux increases.

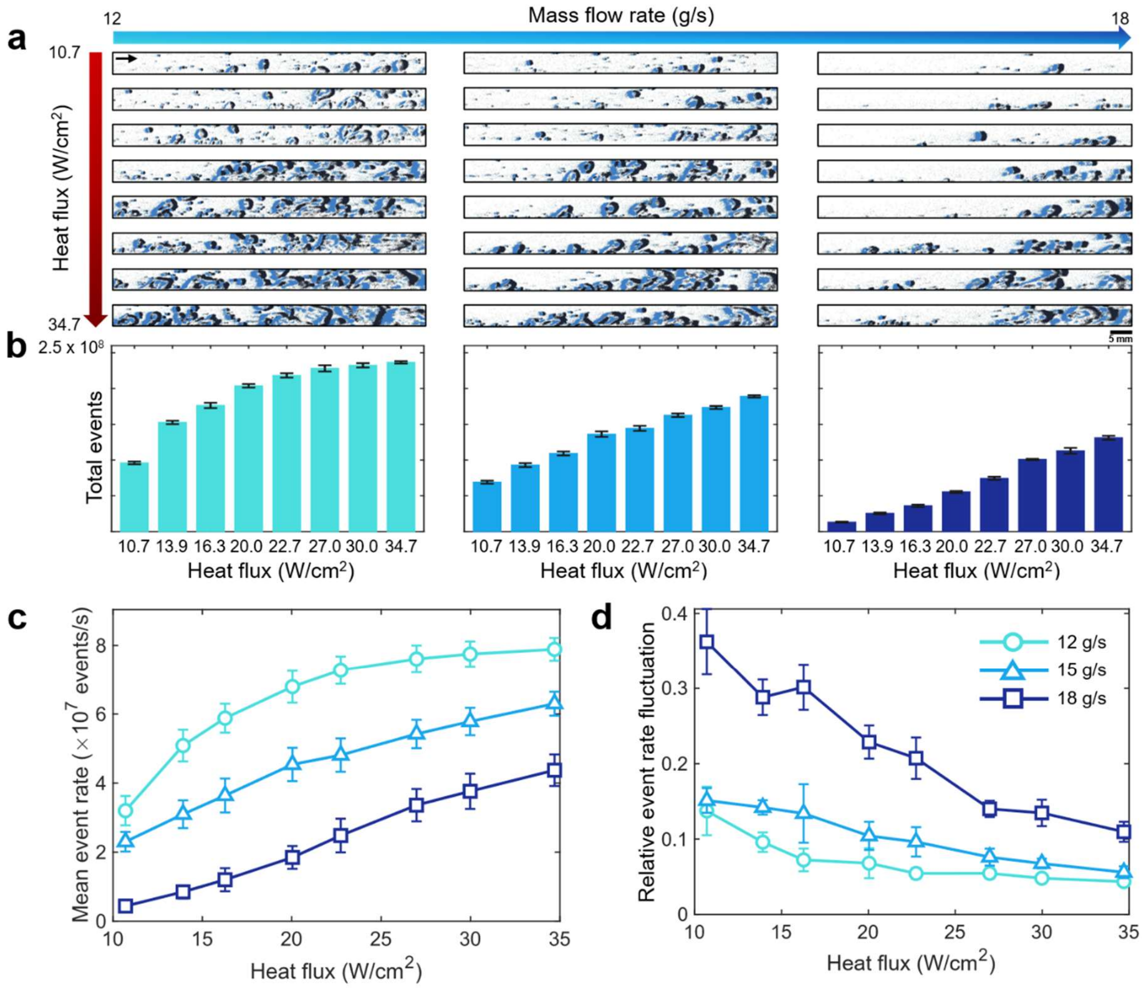

Figure 31. Event camera response under different mass flow rate and heat flux conditions. (a) Representative event accumulated visualizations for mass flow rates of 12, 15, and 18 g/s over heat fluxes from 10.7 to 34.7 W/cm². (b) Total event counts accumulated over 3 s for each condition. Error bars represent within-recording temporal variability estimated from six non-overlapping 0.5 s sub-windows and converted to equivalent 3 s total counts. (c) Mean event rate calculated from the time-binned event rate signal within each 3 s recording. Error bars represent the standard deviation of the time-binned event rate signal, indicating within-recording temporal fluctuation rather than independent repeated-trial uncertainty. (d) Relative event rate fluctuation as a function of heat flux and mass flow rate. The results show that event activity generally increases with increasing heat flux, while mass flow rate modifies the event-count magnitude, mean event rate, and temporal fluctuation characteristics.

After quantifying the condition-averaged event response, the time-binned event rate signal is analyzed in the frequency domain to capture its temporal fluctuation structure. While the mean event rate and relative event rate fluctuation describe the average intensity and relative temporal variability of the event response, spectral descriptors provide additional information on how event activity is distributed across temporal frequencies. Specifically, spectral entropy quantifies the degree of frequency-domain spreading.

To illustrate these temporal characteristics more directly, representative event rate traces are shown in Figure 32a for low, intermediate, and high heat flux cases at 12 g/s. These traces demonstrate that the event camera captures the temporal evolution of event-generating interfacial activity within the 3 s observation window. The corresponding FFT spectra in Figure 32b reveals the frequency-domain content of the event rate fluctuations. For the representative 12 g/s cases, the dominant FFT peak increases from 3.33 Hz at 10.70 W/cm² to approximately 9 Hz at intermediate and high heat fluxes, indicating that stronger boiling activity introduces faster event rate fluctuation components.

Figures 32c quantifies the frequency-domain temporal structure of the event rate signal using spectral entropy, H_f. Spectral entropy quantifies how broadly the event rate fluctuation energy is distributed across frequencies. A signal with a clear dominant frequency has spectral energy concentrated within a narrow frequency band, resulting in lower spectral entropy. In contrast, more irregular or broadband temporal fluctuations distribute spectral energy over a wider frequency range, resulting in higher spectral entropy.

At 12 g/s, the spectral entropy increases from 0.900 to 0.953 as heat flux increases, indicating that the event rate fluctuation spectrum becomes more broadly distributed at higher heat flux. This trend is larger than the sub-window variability for most 12 g/s cases, suggesting that the change in spectral entropy reflects an operating-condition-dependent shift in temporal event activity rather than only short-time fluctuation within a single recording. These results show that event-based sensing captures frequency-domain temporal structure beyond condition-averaged event counts.

The spectral trends are most pronounced at 12 g/s and are partially observed at 15 g/s, while the 18 g/s condition shows a less monotonic response. This suggests that the temporal spectral structure of event activity is governed by both heat flux and mass flow rate. The spectral descriptors do not necessarily follow a simple monotonic ordering with mass flow rate because they quantify the frequency-domain structure of event rate fluctuations rather than the total magnitude of event activity. At higher mass flow rate, stronger convective transport may suppress or modify the heat-flux-dependent spectral shift observed at lower flow rates. These results indicate that FFT-based event descriptors characterize the temporal structure of event-generating interfacial activity and provide instability-relevant signatures of local interfacial unsteadiness.

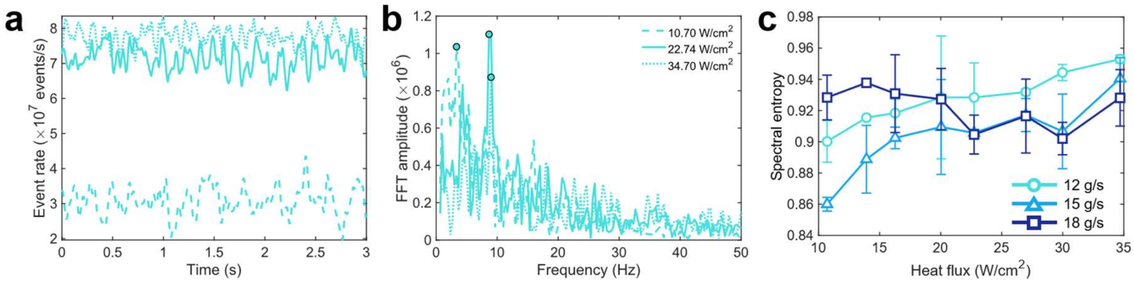

Figure 32. Temporal event activity and spectral structure across flow boiling conditions. (a) Representative event rate time traces and (b) corresponding FFT spectra for low, intermediate, and high heat flux cases at 12 g/s. Markers in (a) indicate the dominant FFT peak frequencies. (c) Spectral entropy, H_f, calculated from the event rate FFT spectra across all operating conditions. Spectral entropy quantifies the frequency-domain spreading of event rate fluctuations, providing a measure of temporal interfacial activity beyond condition-averaged event counts. Error bars represent the standard deviation calculated from three non-overlapping 1 s sub-windows within each 3 s recording.

Together, these temporal descriptors demonstrate that the event camera captures systematic changes in flow boiling activity. Mean and peak event rates quantify the intensity of event generation, relative event rate fluctuation describes the degree of temporal intermittency. The combined trends indicate that increasing heat flux strengthens event activity and promotes a transition from intermittent to more persistent temporal behavior. This temporal and spectral sensitivity supports the use of event-based sensing as a compact diagnostic representation of flow boiling dynamics and provides an important basis for real-time event-driven classification in the following chapter.

4.3.2 Spatial Event Activity

The spatial distribution of event activity is analyzed using the descriptors defined in previous section, including the globally scaled event density map, high density coverage ratio, and spatial entropy. While the temporal descriptors in previous section describe how event activity changes over time, the spatial descriptors identify where event generating interfacial activity is concentrated within the observation window. Figure 33a shows representative globally scaled event density maps accumulated over 3 s for mass flow rates of 12, 15, and 18 g/s across increasing heat flux. These maps visualize the spatial distribution of event activity and show that both the extent and localization of activity vary with operating condition.

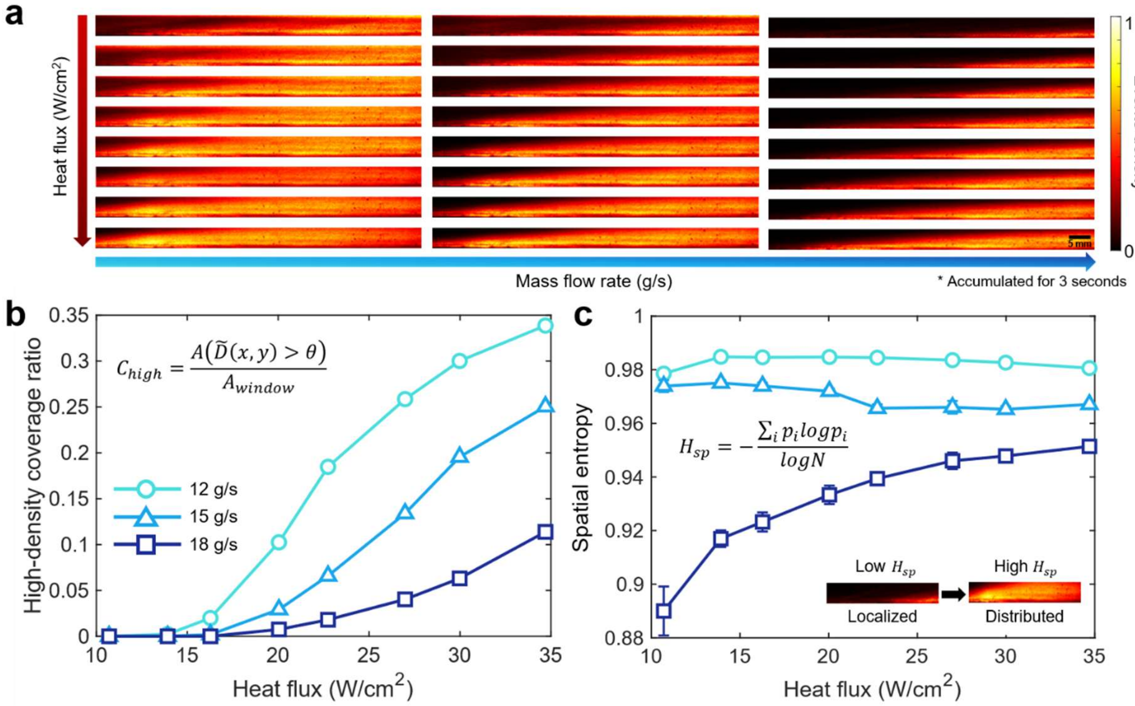

Figure 33. Spatial redistribution of event activity under different heat flux and mass flow rate conditions. (a) Representative globally scaled event density maps accumulated over 3 s for different mass flow rates and heat fluxes. (b) High-density coverage ratio, C_{high}, defined as the area fraction of pixels with globally scaled event density greater than the threshold. Higher C_{high}, indicates spatial expansion of high-density event regions. (c) Spatial entropy, H_{sp}, calculated from the Shannon entropy of the event-density distribution and normalized by the maximum entropy corresponding to a uniform distribution over the observation window. Values close to 1 indicate broadly distributed event activity, whereas lower values indicate more localized activity. Increasing heat flux generally increases high-density coverage while producing more modest changes in spatial dispersion.

As heat flux increases, the event density maps show a clear expansion of high activity regions. At lower heat flux, high event density regions are relatively weak and localized. With increasing heat flux, these regions become more spatially extended, indicating stronger interfacial motion, vapor generation, and redistribution of liquid vapor boundaries. This trend is particularly evident at the lower mass flow rate, suggesting that reduced convective transport allows vapor and interface structures to remain longer within the observation window and develop into more spatially distributed event-active regions.

The high-density coverage ratio, C_{high}, is used to quantify this spatial expansion. As shown in Figure 33b, C_{high} increases monotonically with heat flux for all mass flow rates, indicating that the area occupied by strongly active event regions becomes larger as wall heating increases. Error bars represent within recording temporal variability estimated from six non-overlapping 0.5 s sub windows. For C_{high}, the error bars are negligible on the plotted scale because the metric is calculated from a thresholded area fraction of strongly active pixels.

The increase becomes more pronounced above 20.04 W/cm². At the highest heat flux of 34.70 W/cm², C_{high} reaches 0.339, 0.250, and 0.114 for the 12, 15, and 18 g/s conditions, respectively. Thus, the lower mass flow rate conditions exhibit a larger fraction of the observation window occupied by high density event regions, whereas the 18 g/s condition remains more spatially localized over the tested heat flux range. This flow rate dependence is consistent with the lower overall event activity observed at 18 g/s. Stronger convective transport may move vapor structures and liquid vapor interfaces more rapidly through the observation window, reducing the time available for high density event regions to expand spatially. In contrast, lower mass flow rates may allow event generating interfacial structures to persist longer within the observation window, leading to greater high-density coverage at elevated heat flux.

Spatial entropy, H_{sp}, is used to evaluate the degree of spatial dispersion in the event density distribution. As shown in Figure 33c, H_{sp} remains close to 1 for most conditions, indicating that event activity is broadly distributed across the observation window rather than concentrated at only a few pixel locations. Therefore, the relatively small changes in H_{sp} are interpreted as modest spatial redistribution within an already broadly distributed event density field. Error bars represent the standard deviation of H_{sp} calculated from the same 0.5 s subwindows and indicate within recording variability in the spatial dispersion of event density.

The 18 g/s condition shows a noticeable increase in H_{sp} with heat flux, from 0.938 at 10.7 W/cm^2 to 0.951 at 34.7 W/cm^2, suggesting a modest increase in the spatial dispersion of event activity. In contrast, the 12 and 15 g/s conditions maintain relatively high entropy values across the tested heat flux range, indicating that event activity is already broadly distributed within the observation window.

These spatial descriptors reveal that event activity is governed by the combined effects of heat flux and mass flow rate. Increasing heat flux enhances vapor generation and liquid-vapor motion, causing high-density event regions to expand. Increasing mass flow rate, however, strengthens convective transport and can shift or suppress sustained event activity within the observation window. Therefore, the spatial event response provides information that is not captured by temporal descriptors alone. While event rate metrics quantify the intensity and intermittency of the event stream, event-density maps, coverage ratio, and spatial entropy describe how dynamic boiling activity is organized spatially.

Overall, the spatial analysis demonstrates that event cameras can capture systematic redistribution of flow boiling activity under varying operating conditions. The normalized event-density map provides a direct visualization of where brightness-change activity occurs, while C_{high} and H_{sp} convert this spatial information into quantitative descriptors. These results support the use of event-based sensing as a compact diagnostic approach for identifying changes in the spatial organization of two-phase activity.

4.3.3 Streamwise Event Density Profile

To further examine the spatial organization of event activity along the flow direction, the normalized event density maps are projected into one-dimensional streamwise profiles. The resulting profiles describe how event generating interfacial activity is distributed from the upstream region, $x/L = 0$, to the downstream region, $x/L = 1$. While the high-density coverage ratio and normalized spatial entropy provide scalar measures of spatial spreading, the streamwise profile identifies where the relative event density is located along the channel.

At 12 g/s, shown in Figure 34a, the streamwise profiles vary with heat flux. At the lowest heat flux of 10.7 W/cm², the normalized event density increases gradually from the upstream region toward the downstream region. This indicates that the relative event density becomes larger along the flow direction within the observation window. At higher heat fluxes of 22.7 and 34.7 W/cm², elevated event density appears over a wider range of streamwise locations, especially between approximately $x/L = 0.2$ and $x/L = 0.8$. The profiles then decrease toward the downstream end. Since each profile is normalized by its own maximum value, this decrease does not indicate that event activity disappears downstream. Instead, it indicates that the downstream event density is lower relative to the maximum value within the same condition.

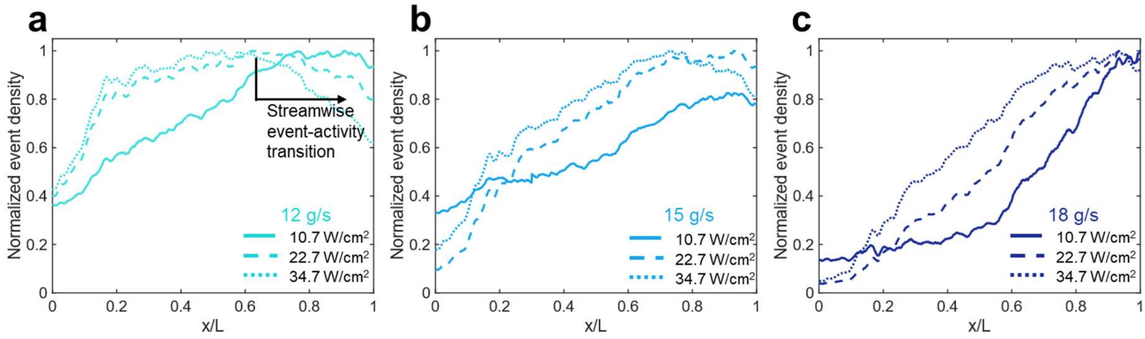

Figure 34. Streamwise event-density profiles extracted from normalized event-density maps. Streamwise event density profiles obtained from normalized event density maps at (a) 12 g/s, (b) 15 g/s, and (c) 18 g/s. The profiles are plotted as a function of normalized streamwise location, x/L, from the upstream to downstream regions of the observation window. Localized peaks indicate concentrated event activity, whereas broader profiles indicate elevated event density over a larger streamwise region.

As shown in Figure 34b, the 15 g/s profiles show a gradual increase along the streamwise direction. Compared with the 12 g/s case, the relative event density is less elevated over the full observation window and tends to become larger toward the middle and downstream regions. This indicates that the location of relatively high event density changes with heat flux and mass flow rate.

Figure 34c shows the 18 g/s profiles, where the normalized event density increases more steeply toward the downstream region. The event density remains relatively low near the upstream side and becomes larger near the outlet side. This profile suggests that, at higher mass flow rate, event generating structures are observed more strongly toward the downstream portion of the viewing window.

Overall, the streamwise profiles show that mass flow rate and heat flux modify not only the total level of event activity, but also its relative streamwise distribution. Lower mass flow rate cases show elevated event density over a wider portion of the observation window at higher heat flux, whereas higher mass flow rate cases show relatively larger event density near the downstream side. These observations complement the scalar spatial descriptors discussed in previous section by identifying where event activity is relatively concentrated along the flow direction.

4.3.4 Event-derived Pressure Drop Prediction

The temporal and spatial analyses in the previous sections show that event-camera measurements capture systematic changes in liquid–vapor interfacial activity with heat flux and mass flow rate. The extracted descriptors quantify complementary aspects of the event response, including mean activity intensity, temporal stability, spatial coverage, and spatial dispersion. To examine whether these event-derived characteristics are related to a measurable thermofluidic response, pressure drop is used as an independent system-level reference quantity.

Pressure drop is not treated as a direct target of visual measurement or as a replacement for pressure sensing. Instead, it is used to evaluate whether event-derived descriptors contain information associated with the global hydrodynamic response of the flow-boiling system. Because pressure drop reflects the integrated effects of vapor generation, phase distribution, flow resistance, and interfacial motion within the channel, its relationship with event activity provides a practical test of the thermofluidic relevance of event-camera measurements.

Figure 35a compares the mean pressure drop with the mean event rate for each mass flow rate condition. Within each mass flow rate group, the mean pressure drop increases with mean event rate as heat flux increases. This result indicates that stronger event generating interfacial activity is associated with a larger system level hydrodynamic response within the tested conditions. The dashed lines indicate linear fits within each mass flow rate group. Horizontal error bars represent the standard deviation of the time binned event rate within each condition, whereas vertical error bars represent the standard deviation of the pressure drop within each condition.

Although mean event rate provides a condition-level measure of overall event activity, pressure drop may also be influenced by the temporal unsteadiness of the interfacial response. Therefore, pressure drop prediction is performed using operating conditions together with event-derived temporal descriptors to evaluate whether the event signal provides pressure-relevant information beyond mass flow rate and heat flux alone.

Figure 35b illustrates the multilayer perceptron architecture used for pressure drop prediction. The model receives operating conditions and event-derived temporal descriptors as input and outputs the predicted time-averaged pressure drop. The model architecture and candidate hidden-layer configurations are described in previous section.

Figure 35c compares the measured and predicted mean pressure drop for the best performing model among the tested feature groups. The selected model combines mass flow rate, heat flux, relative event rate fluctuation, F_{rel}, and spectral entropy, H_f. It achieves $R^2 = 0.992$ and an

RMSE of 0.094 kPa. The operating only model serves as a baseline because mean pressure drop is strongly governed by mass flow rate and heat flux. Results for all tested feature groups are provided in the *Appendix.*

F_{rel} quantifies the relative temporal variation of the event rate signal, whereas H_f characterizes how broadly these fluctuations are distributed across frequencies. The improved prediction obtained by including these descriptors suggests that temporal event characteristics contain information associated with interfacial unsteadiness and pressure drop variation. These descriptors therefore refine pressure drop prediction based on operating conditions, rather than replace direct pressure measurements.

Measured mean pressure drop values are obtained from the corresponding pressure drop time series. Representative pressure drop traces for all operating conditions are provided in the *Appendix*. Horizontal error bars represent the standard deviation of the measured pressure drop within each condition. Vertical error bars represent prediction variability associated with model architecture and are estimated from the spread of predictions across the tested MLP candidates within each leave one out cross validation fold.

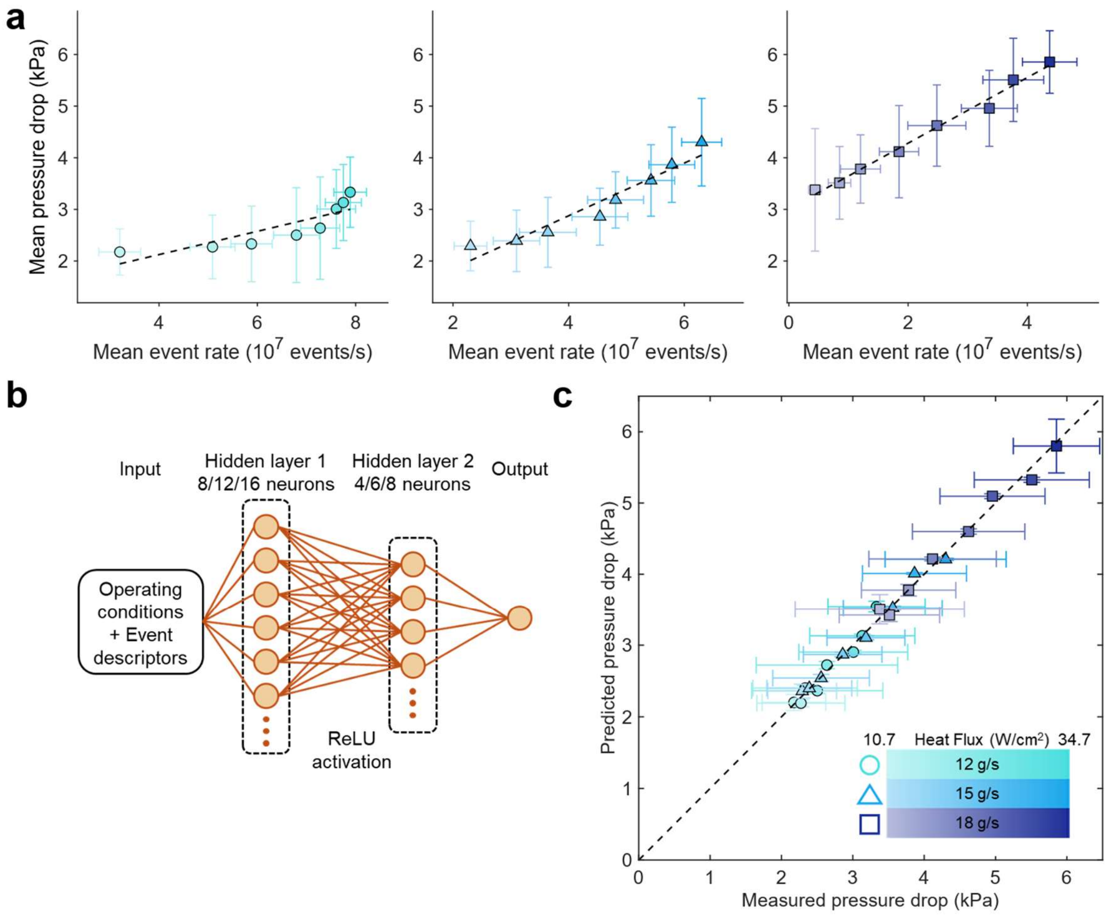

Figure 35. Event activity and pressure drop prediction. (a) Condition-level relationship between mean pressure drops and mean event rate for each mass flow rate. Dashed lines denote linear fits within each mass flow rate group. Horizontal and vertical error bars indicate the within-condition standard deviations of mean event rate and pressure drop, respectively. (b) Schematic of the multilayer perceptron (MLP) used for pressure drop prediction. The model combines operating conditions with event-derived temporal instability descriptors, including relative event rate fluctuation and spectral entropy, to predict the time-averaged pressure drop. (c) Comparison between measured and predicted time-averaged pressure drop for the best performing MLP model evaluated using leave-one-out cross-validation. Horizontal error bars indicate measured pressure drop standard deviations, vertical error bars indicate architecture-induced prediction variability, and the dashed line denotes ideal agreement.

4.4 Conclusion

This chapter establishes an event camera-based framework for analyzing liquid–vapor interfacial activity in flow boiling. Unlike conventional high-speed imaging, which records dense image frames at fixed sampling rates, the event camera records sparse asynchronous brightness-change events generated by dynamic liquid–vapor interfaces. The objective of this chapter is to establish a quantitative methodology for describing event-generating interfacial activity, temporal unsteadiness, and spatial organization in flow boiling.

The event stream is converted into temporal, spectral, and spatial descriptors that characterize boiling dynamics from different perspectives. The temporal descriptors show that increasing heat flux strengthens event generation and changes the response from isolated intermittent activity toward more temporally sustained event activity. The FFT-based spectral descriptors further show that the event rate signal contains frequency-domain temporal information. Spectral entropy reveals changes in the spectral spreading of event rate fluctuations, indicating that event-based sensing captures temporal-unsteadiness-related signatures of local interfacial activity beyond condition-averaged event counts. The spatial descriptors show that heat flux and mass flow rate modify the extent and dispersion of event activity within the observation window. Together, these results demonstrate that event camera measurements can quantify the intensity, temporal structure, and spatial organization of liquid–vapor interfacial activity.

The pressure drop prediction analysis further supports the thermofluidic relevance of the event-derived temporal descriptors. The best prediction performance is achieved when operating conditions are combined with temporal instability descriptors, including relative event rate fluctuation and spectral entropy. This result suggests that event-derived temporal unsteadiness contains pressure-relevant information that complements heat flux and mass flow rate. The pressure drop analysis therefore links event camera measurements to a system-level thermofluidic response without implying replacement of conventional pressure measurements.

Overall, this chapter demonstrates that sparse event streams contain systematic information about flow boiling dynamics. Because event cameras record only local brightness changes rather than dense image frames, they provide a compact and low latency sensing modality for monitoring dynamic boiling activity with reduced data redundancy relative to frame-based imaging. This chapter therefore provides the foundation for the next chapter, where event-based sensing is extended from activity characterization to real-time flow regime classification.

Future work will connect event-derived descriptors with additional thermofluidic measurements, including wall temperature, heat transfer coefficient, pressure drop oscillations, and critical heat flux. Future studies will also integrate event cameras with high-speed optical and infrared imaging to develop multimodal boiling diagnostics for monitoring local interfacial activity and temporal unsteadiness in flow boiling.

CHAPTER 5: Real-Time Flow Regime Classification

5.1 Introduction

Boiling systems are widely used for compact thermal management because liquid-vapor phase change enables high heat flux dissipation with relatively small temperature rise.[1–3,87] In flow boiling, the working fluid is driven through a heated channel, where heat removal is governed not only by imposed operating conditions but also by the evolving distribution and motion of liquid and vapor phases.[88–90] Therefore, real-time identification of flow regimes is important for monitoring heat transfer performance, pressure variation, and operational stability in high-power-density cooling systems.

Flow regimes define the arrangement and movement of liquid and vapor phases within the channel, directly influencing heat transfer efficiency, pressure drop, and system stability.[91–93] These regimes include bubbly, elongated bubbly, slug, stratified, annular, unstable, and dryout-related patterns, each of which exhibits distinct phase distribution and dynamic behavior.[94,95] However, accurate classification remains challenging because several regimes can be visually similar or appear as transitional states. Stratified smooth, stratified wavy, and annular flows, for example, share a similar layered structure in which liquid remains near the wall while vapor occupies a larger portion of the channel. Their differences may appear only through subtle interface motion, wave formation, or temporal fluctuation.[96–98] These unstable or transitional states are particularly important because delayed or incorrect detection can affect heat transfer performance and operational safety.[99]

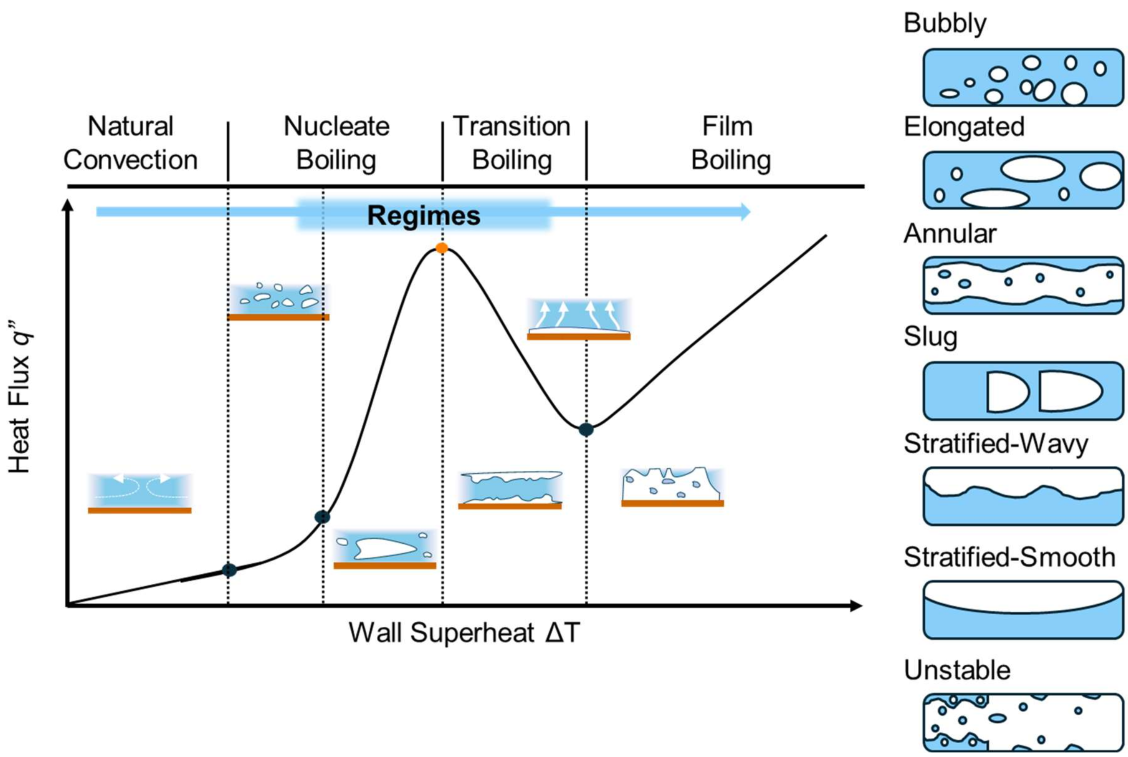

Figure 36. Boiling curve and flow boiling regimes. The boiling curve illustrates the relationship between surface heat flux and temperature difference, highlighting seven distinct flow boiling regimes that influence heat transfer performance and stability.

Several diagnostic and machine learning approaches have been explored for flow regime classification, including sensor-based methods, acoustic measurements, optical imaging, and data-driven models.[100–106] Sensor-based approaches can capture pressure, temperature, vibration, or impedance responses, but they often provide indirect information and may depend strongly on the experimental configuration. Acoustic methods can detect instability-related signatures, but their performance may be affected by background noise and signal interference. Optical imaging provides direct visualization of two-phase structures and has enabled learning-based flow classification, but frame-based image sequences can introduce substantial data redundancy when high temporal resolution is required.

Optical imaging, particularly when combined with deep learning-based convolutional neural networks (CNNs), has been widely used for bubble detection and flow regime classification. [7,8,107–109] High-speed cameras can capture rapid boiling phenomena with microsecond precision, but their data-intensive outputs significantly increase computational overhead. These methods record every pixel at every timestep, often across multiple color channels, resulting in excessive data redundancy because many pixels merely capture static backgrounds.[69] Moreover, short recording durations during high-speed imaging and high-power consumption make high-speed cameras impractical for continuous operation in industrial applications. Deep learning methods have attempted to address these challenges using encoder-decoder architectures, achieving competitive classification accuracy.[109] However, such models often suffer from low recall and frequent misclassification, particularly under unstable or transitional flow conditions.

Neuromorphic event cameras present a promising alternative by providing real-time visual sensing with low power consumption, minimal data redundancy, and high temporal resolution.[71,72] Instead of producing full image frames, event cameras generate sparse data streams with precise timestamps by recording local brightness changes at individual pixels. This event-based sensing mechanism preserves fine temporal features, reduces motion blur, and focuses on dynamic interfacial activity rather than static background information. These characteristics make event cameras well suited for capturing fast, localized variations in dynamic two-phase flows. However, the event-based approach still requires optical access and is therefore limited to environments where transparent sections, inspection windows, or endoscopic views are available. Within these constraints, event cameras can serve as a complementary modality that augments embedded sensors by providing high-fidelity spatiotemporal information for boiling diagnostics.[110,111]

Chapter 4 demonstrates that neuromorphic event-camera measurements contain systematic information about flow boiling activity. The event-derived descriptors capture temporal intensity, burst-like intermittency, spatial redistribution, streamwise activity organization, and activity-state transitions. These results show that event streams provide a compact representation of dynamic boiling activity rather than simply serving as sparse visual data. Building on this finding, the present chapter extends event-based sensing from activity characterization to real-time flow regime classification.

In this chapter, a real-time event-driven classification framework is developed and evaluated for flow boiling regimes. Multiple learning architectures are tested using optical and event-based representations to compare how different sensing modalities and data formats affect classification performance. These approaches include optical frame-based models, event-frame-based models, frequency-domain methods, spiking neural networks, and event-sequence models.

Overall, this chapter shifts the dissertation from event-based activity characterization to real-time diagnostic prediction. While Chapter 4 uses event-camera data to quantify temporal and spatial activity descriptors, Chapter 5 uses event data as direct input for flow regime classification. This progression establishes event-based learning as a pathway toward continuous monitoring and intelligent control of flow boiling systems.

5.2 Event-Based Learning Framework for Flow Regime Classification

This section presents the learning framework developed for real-time flow regime classification in flow boiling systems. Building on the event-based sensing and activity analysis introduced in Chapter 4, the present framework uses both optical and event-based data representations as inputs to multiple classification models. The objective is to evaluate how different sensing modalities and learning architectures represent flow regime dynamics and to identify a model structure suitable for low latency regime prediction.

The overall framework consists of four main components: dataset construction, data representation, model training, and real-time inference. First, optical videos and event-camera recordings are organized into regime-labeled datasets. Second, the visual data are converted into appropriate input formats depending on the model type, including optical image frames, accumulated event frames, frequency-domain representations, and raw event sequences. Third, multiple learning architectures are trained and evaluated using the same regime labels to enable direct comparison across sensing modalities. Finally, the selected model is implemented in a real-time inference pipeline to evaluate online classification performance.

Figure 37 presents the optical and event-based representations of seven different flow patterns. In Figure 37a, subcooled inlet flow boiling patterns are shown from bubbly and elongated bubbly flow to slug, stratified, annular flow, and dry-out, illustrating the broader progression of boiling conditions. In Figure 37b, the neuromorphic event representation captures dynamic brightness changes while suppressing redundant background information, thereby preserving critical flow structures. The red rectangles highlight the three most similar flow patterns, stratified smooth, stratified wavy, and annular, whose subtle differences are more distinctly revealed in the event-based representation. This comparison underscores the complementary strengths of optical and event-based sensing, where optical imaging provides high spatial resolution, while event data offer superior temporal sensitivity for detecting rapid transitions and unstable flow patterns.

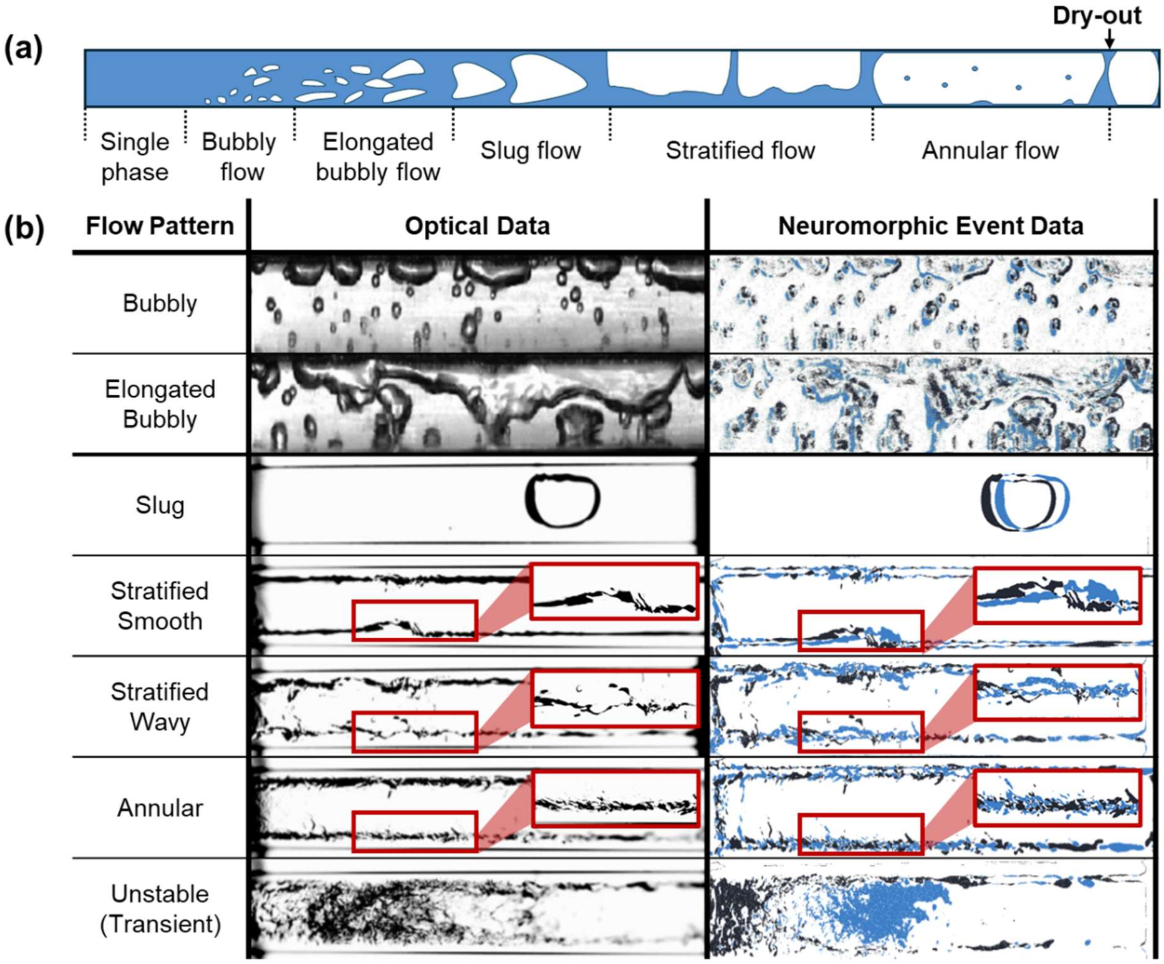

Figure 37. Visualization of optical and event representation of seven different flow patterns. (a) Subcoole d inlet flow boiling patterns showing bubbly, elongated bubbly, slug, stratified and annular flow followed by dry-out. (b) The neuromorphic event data captures dynamic brightness changes, effectively removing r edundant background information while preserving critical flow structures. The red rectangles highlight t he three most similar flow patterns: Stratified Smooth, Stratified Wavy, and Annular, whose subtle differe nces are more distinctly revealed in the event-based representation, demonstrating its advantage in enhanc ing flow pattern differentiation.

Due to heat flux and mass flux limitations, the present experimental rig directly captures only bubbly and elongated bubbly regimes in both optical and event formats. To build a more complete classification dataset, additional high-speed optical recordings of slug, stratified smooth, stratified wavy, annular, and unstable regimes are obtained from the Energy Transport Research Lab at UIUC. Since these recordings do not contain corresponding event-camera measurements, they are converted into synthetic event streams using the V2E emulation tool, which detects frame-to-frame brightness changes to approximate Dynamic Vision Sensor output. This approach expands the dataset across all seven flow regimes while maintaining compatibility with event-based learning models.

To make the dataset suitable for machine learning models, both real and emulated event streams are converted into model-specific input representations. For models requiring image-like inputs, event streams are accumulated over predefined time windows, Δt, to form event frames. This process preserves the temporal richness of the event data while aligning with frame-based architectures such as CNNs. For sequence-based models, raw event streams are used directly without event-frame reconstruction. By combining real event data from experiments with emulated event data from V2E, the dataset leverages the strengths of both sources: real event data provide hardware-accurate measurements, while emulated event data extend the dataset to flow regimes not directly captured by the present experimental rig.

The proposed framework integrates multiple machine learning architectures, each designed to use a specific optical or event-based representation, as illustrated in Figure 38. Optical frames are manually annotated based on observed flow characteristics and categorized into seven flow regimes: bubbly, elongated bubbly, slug, stratified smooth, stratified wavy, annular, and unstable patterns. This labeled dataset serves as the basis for training and evaluating the classification models.

Table 5. Summary of dataset with flow regimes.

Regime	Total Optical Frames	Total Event Frames	Total Accumulation Time (ms)
Bubbly	6,450	8,429	1.3
Elongated Bubbly	4,105	4,835	1.2
Slug	878	6,081	7.6
Stratified Smooth	668	3,721	14.4
Stratified Wavy	1,555	10,203	6.3
Annular	2,405	18,032	7.7
Unstable	750	2,471	4.6

Figure 38 summarizes the model architectures and data pathways used in this chapter. Optical data captured using high-speed cameras are used with optical CNN models, which extract spatial features from dense image frames. Reconstructed event data, generated by accumulating event streams over a fixed time window Δt, are used by both the Event CNN and the Fourier k-nearest-neighbor model. In contrast, raw event streams from both real event-camera measurements and V2E-emulated events are used directly by the Event SNN and Event LSTM models. These sequence-based models capture temporal dependencies and dynamic transitions without requiring event reconstruction.

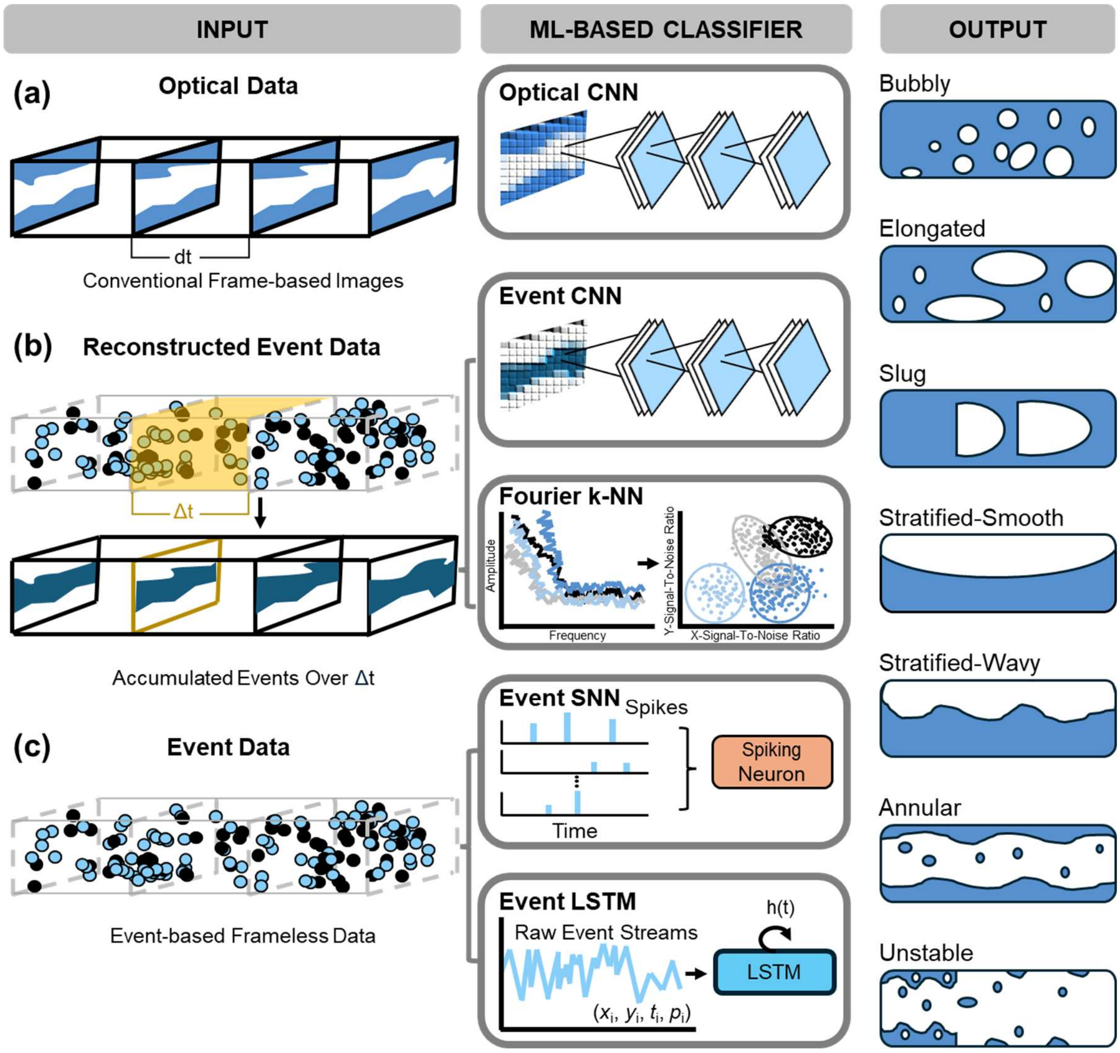

Figure 38. Machine learning (ML) model architectures for flow classification task. Both emulated and raw event data are processed identically, but their preprocessing differs significantly from optical data. (a) Optical data, captured using high-speed cameras, are used exclusively with the convolutional neural network (CNN), leveraging spatial features from densely packed image frames for classification. (b) Reconstructed event data, generated by accumulating event streams over a fixed time window (Δt), are used by both the Event-CNN and the Fourier k-nearest neighbor(k-NN) model. (c) Event data, collected from both real experiments and simulated using V2E, are processed as raw event streams in both the spiking neural network (SNN) and the long short-term memory (LSTM) models. These models directly capture temporal dependencies and sequential patterns without the need for event reconstruction, effectively modeling the dynamic transitions of flow regimes.

The Optical CNN serves as the frame-based baseline and evaluates how well flow regimes can be classified using optical morphology alone. In this chapter, CNN-based models include ConvNeXt, AlexNet, and a shallow CNN to compare different levels of frame-based spatial feature extraction. The Event CNN adapts conventional convolutional architectures to accumulated event frames, allowing spatial patterns in event activity to be used for classification.

The Fourier-based method applies Fast Fourier Transform to reconstructed event frames to extract frequency-domain features associated with regime-dependent oscillatory behavior. These features are grouped using k-means clustering and then classified using k-nearest neighbors. The Event SNN processes event-based temporal information using a spike-inspired architecture that is compatible with sparse event-driven computation. Finally, the Event LSTM processes raw event sequences directly and learns temporal dependencies through recurrent memory. Among these approaches, the Event LSTM is emphasized because it avoids dense image reconstruction and is well suited for low latency regime prediction.

To develop robust classification models, the dataset is split into 70% for training, 15% for validation, and 15% for testing, ensuring representation of all seven flow regimes. This structured split allows the models to generalize across diverse boiling conditions while reducing overfitting. Given the class imbalance across flow regimes, data augmentation techniques such as event flipping and temporal jittering are applied to improve model robustness. Model training and evaluation are conducted on an NVIDIA A30 GPU. Generic hyperparameter settings are used across all models, with slight variations tailored to each architecture, as summarized in Table 6.

Table 6. Generic hyperparameter settings for models.

Hyperparameter	Event CNN	Optical CNN	Event SNN	Event LSTM
Epochs	25	35	55	25
Batch Size	128	128	128	128
Optimizer	Adam	Adam	Adam	Adam
Learning Rate	1e-3	1e-3	1e-4	1e-3
SNN β	N/A	N/A	0.95	N/A
SNN Steps	N/A	N/A	15	N/A

The real-time classification pipeline is designed to operate continuously during event acquisition. Incoming events are collected, preprocessed, and passed to the trained Event LSTM model for regime prediction. To maintain low latency, the pipeline uses a single-item queue so that the most recent event sequence is prioritized and outdated data are discarded. This design prevents processing delays from accumulating during continuous operation. A majority-voting smoother is then applied over recent predictions to reduce short-term fluctuations and stabilize the displayed regime output.

The final dataset used in training consists of both real and emulated event data. The inclusion of real event data from the Prophesee neuromorphic event camera ensures hardware-accurate insight, while emulated event data from the V2E conversion tool expands coverage to flow conditions not experimentally recorded. A detailed condition-by-condition summary of the real and emulated event data is provided in *Appendix*. Overall, this framework provides a structured basis for comparing optical and event-based learning approaches for flow regime classification. The following sections present the model comparison results and real-time classification performance, with particular emphasis on the Event LSTM framework.

5.3 Model Comparison and Real-Time Event-Driven Classification

To evaluate the proposed event-based framework, five classification models are compared using both optical and neuromorphic representations: Optical CNN, Event CNN, Fourier k-nearest neighbor (k-NN), Event SNN, and Event LSTM. Each model is designed to exploit different characteristics of the input data, enabling systematic comparison between frame-based and event-based learning strategies under the same flow boiling classification task. The comparison focuses on computational efficiency, classification accuracy, and robustness across the seven representative flow regimes.

Figure 39 presents the overall comparison of the five models in terms of inference time, processing time, and classification accuracy. The results show that event-based models generally outperform the optical frame-based model in both speed and classification performance. Optical CNN captures high-resolution spatial features from conventional images and performs reliably in relatively steady regimes, but its computational burden is substantially larger because it processes dense frame-based data. In addition, its limited temporal sensitivity reduces its effectiveness in capturing unstable or rapidly evolving flow behavior.

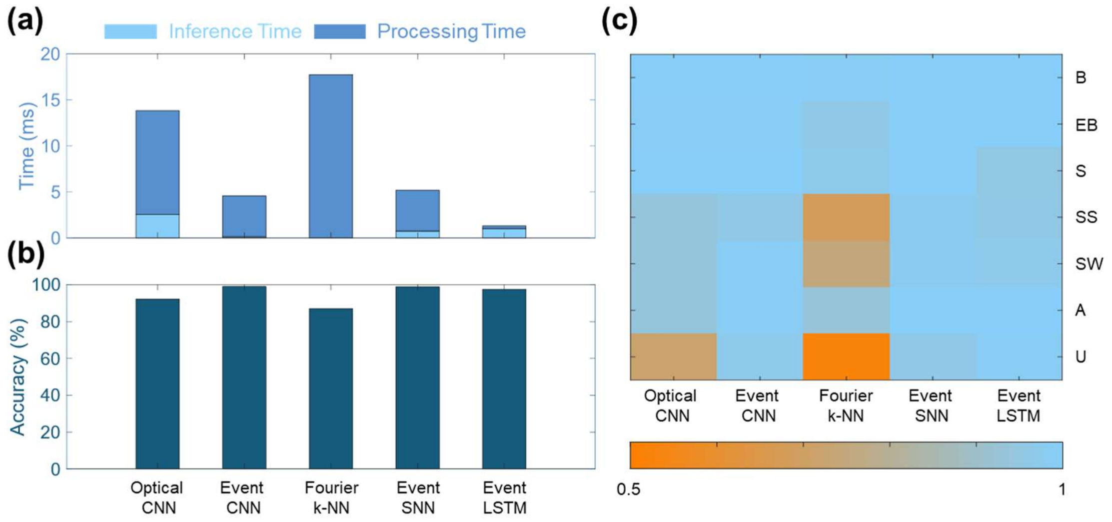

Figure 39. Model comparison: inference time, processing time, and accuracy. Comparison of Optical CNN, Event CNN, Fourier k-NN, Event SNN, and Event LSTM in terms of (a) inference time and processing time, (b) overall classification accuracy, and (c) regime wise performance across seven boiling flow regimes. Event-based models generally outperform the optical frame-based model in both efficiency and classification robustness, with Event LSTM providing the most balanced performance across all regimes.

Among the event-based approaches, Event CNN achieves strong classification accuracy by converting event streams into frame-like inputs and then applying convolutional feature extraction. However, the event-to-frame reconstruction step introduces additional computational overhead, which can increase latency and reduce suitability for resource-constrained real-time deployment. Fourier k-NN provides the fastest inference by compressing the input into compact frequency-domain features, but its classification performance is weaker in complex or unstable regimes because it emphasizes dominant spectral patterns rather than localized spatiotemporal structure.

Event SNN and Event LSTM both operate directly on raw event streams and therefore preserve the asynchronous nature of the neuromorphic signal. Event SNN aligns naturally with event-driven data and performs well for flows with strong temporal complexity, but the lack of native support for spiking operations on standard hardware increases simulation overhead and latency.

In contrast, Event LSTM provides the best overall trade-off between accuracy, inference speed, and processing efficiency. By operating directly on raw event sequences without reconstruction, it preserves temporal resolution, maintains low computational overhead, and performs robustly across all regimes, including unstable and transitional cases. The overall classification accuracy of Event LSTM reaches 97.6%, with a processing time of 0.28 ms, demonstrating its suitability for real-time flow boiling classification.

The regime wise accuracy comparison further highlights the importance of temporal event information as shown in Figure 39c. The most challenging regimes are those with overlapping or transitional characteristics, particularly stratified smooth, stratified wavy, annular, and unstable flow. These patterns share similar large-scale spatial organization and can therefore be difficult to distinguish using purely frame-based or frequency-compressed representations. Event-based models, especially Event LSTM, show more balanced accuracy across all seven regimes because they directly exploit the fine temporal structure of the event stream. This is particularly important for unstable flow, where short-lived and irregular interface motion plays a dominant role in distinguishing the regime.

Based on this comparison, Event LSTM is selected as the primary architecture for real-time deployment. The real-time framework is built around raw event inputs in the form (x, y, p, t), where x and y denote pixel coordinates, p is the event polarity, and t is the timestamp. Since timestamps are not used directly as classifier inputs, the real-time model processes sequences of (x, y, p) events, while temporal grouping parameters are used only for synchronization and sequence construction. Spatial coordinates are normalized relative to the flow channel, and an event rate limiter is introduced to maintain temporal consistency and prevent overload under high event rate conditions.

The Event LSTM classifier is implemented in PyTorch using a compact architecture optimized for real-time inference. Input vectors of spatial coordinates and polarity are first embedded into a 32-dimensional feature space, followed by a two-layer LSTM with 128 hidden units per layer. The output is processed through two fully connected layers with dropout and a final softmax classifier. This compact design enables efficient execution on general-purpose processors while preserving sufficient representational capacity to capture complex regime transitions.

To support online operation, a modular asynchronous processing pipeline is developed for event acquisition, inference, and visualization. The system runs three concurrent threads: a main thread for event processing, an inference thread for model evaluation, and a visualization thread for displaying predictions. The main thread streams event data into a first-in-first-out iterator and forwards sequences to a single-item queue. The inference thread processes only the most recent sequence and discards outdated data to avoid memory overflow and reduce bottlenecks. A majority voting smoother over the most recent 150 predictions is then used to stabilize outputs and reduce flickering. This asynchronous architecture enables continuous low latency predictions and robust operation under high event rate conditions.

Sequence length plays an important role in the real-time performance of the Event LSTM. Longer sequences provide richer temporal context, but they also increase latency and may introduce unnecessary redundancy. As shown in Figure 40, a sequence length of 2500 events achieves the best trade-off, yielding approximately 99.4% accuracy with 0.81 ms inference time and 0.19 ms processing time for bubbly and elongated bubbly flow. A length of 5000 events provides similarly high accuracy, approximately 99.7%, but with higher inference and processing times. These results indicate that an intermediate sequence length is sufficient to retain the relevant temporal dynamics while maintaining the responsiveness required for online classification.

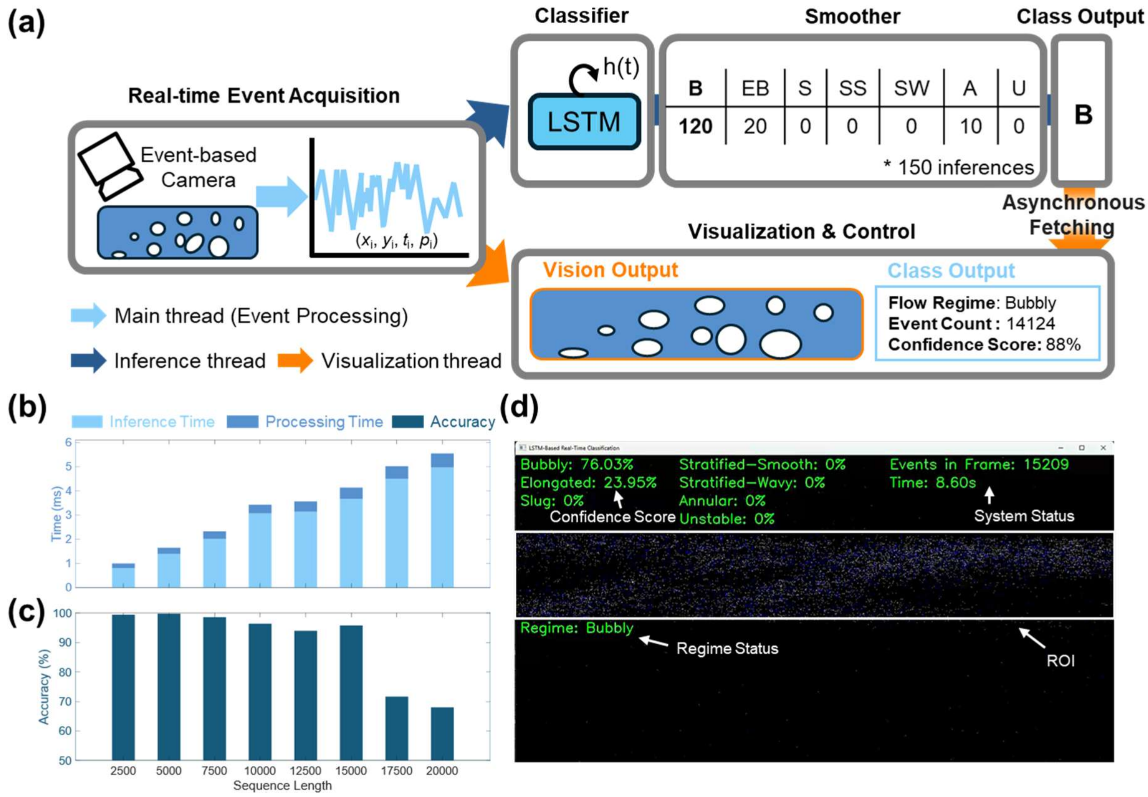

Figure 40. Real-time and online classification framework using Event LSTM. (a) Asynchronous system architecture for real-time flow regime classification using event-based data. (b) Inference time as a function of sequence length. (c) Accuracy as a function of sequence length. (d) Graphical user interface displaying event visualization, predicted regime, and confidence information during live operation. The Event LSTM enables stable low latency online classification through asynchronous processing and majority-vote smoothing.

The real-time system is further evaluated under actual flow boiling conditions. Although current hardware and experimental constraints limit live testing primarily to bubbly and elongated bubbly regimes, the deployed system demonstrates stable and responsive behavior. The graphical user interface displays real-time regime predictions together with polarity-coded event visualizations, confidence information, and system status. The majority voting smoother significantly improves temporal consistency by suppressing short-term output fluctuations, making the real-time predictions easier to interpret during continuous monitoring.

An additional advantage of the event-based sensing system is its resilience to environmental variability. Compared with conventional optical methods, the event sensor operates more robustly under changing lighting conditions, partial shadowing, and partial visual obstruction because it responds primarily to dynamic brightness changes rather than dense frame content. Offline tests using V2E-generated synthetic event data with abrupt lighting changes and partial occlusions confirm that the preprocessing pipeline and output smoother maintain stable predictions in many cases. However, abrupt lighting transitions can still generate spurious events, indicating that adaptive filtering or bias control will be important directions for future improvement.

Overall, the results establish that event-driven learning provides a practical and effective pathway for real-time boiling flow regime classification. Event-based models consistently outperform frame-based approaches in terms of temporal responsiveness and data efficiency, while Event LSTM provides the best balance between accuracy, speed, and robustness. By combining asynchronous neuromorphic sensing with sequential learning and modular software design, the proposed framework enables reliable low latency classification of two-phase flow regimes and provides a strong foundation for future closed-loop monitoring and intelligent thermal management systems.

5.4 Transformer-Based Extensions for Event-Driven Classification

The preceding results establish the raw event LSTM as the primary architecture for live real-time event-driven regime classification. The LSTM directly processes asynchronous event sequences and sequentially accumulates temporal information through recurrent hidden states. This structure is well matched to event streams, where regime-dependent information is encoded in both the instantaneous event distribution and the temporal development of interfacial activity.

However, flow boiling regimes also contain spatially distributed and temporally correlated features, such as vapor redistribution, wave motion, and annular film fluctuation. These features may extend across different regions of the observation window and over multiple time intervals. Therefore, Transformer-based models are evaluated to examine whether self-attention can better capture long-range spatial and temporal relationships in event-driven boiling data. Unlike recurrent models, self-attention directly compares spatial or temporal elements across the input representation without relying on sequential hidden-state propagation. This provides a complementary approach for examining regime-dependent relationships distributed across the observation window and over time.

Three Transformer-based extensions are considered. These include a frame-based Vision Transformer, a temporal Transformer, and a direct raw event Transformer. These models are not intended to replace the deployed LSTM framework. Instead, they are used to clarify how different attention-based representations affect classification accuracy, computational latency, and model complexity. The models are trained and evaluated using the same training, validation, and test split. Table 7 summarizes their classification accuracy, processing time, inference time, and model size under consistent evaluation conditions. The reported timing values represent computational execution after the required event data have been acquired. Therefore, they do not include the physical duration required to collect events over an accumulation window.

The frame-based Vision Transformer applies spatial self-attention to a single accumulated event frame. This representation converts sparse asynchronous events into an image-like structure, allowing the model to capture long-range spatial relationships among vapor structures, interfacial boundaries, and event-density patterns. The model achieves high classification accuracy of 98.0%, indicating that accumulated event frames contain strong regime-dependent spatial information. However, because the temporal evolution within the accumulation window is compressed into one frame, the model does not explicitly resolve how the interfacial structure changes over time. In addition, the event-frame construction step contributes to the overall processing latency, with a processing time of 3.11 ms and an inference time of 3.01 ms. Because the accumulation window is selected using known regime characteristics, the reported accuracy represents an offline assessment of the event-frame representation rather than a fully blind real-time classification result.

The temporal Transformer addresses this limitation by processing a sequence of event frames. By applying attention across temporally ordered event-frame representations, the model captures both spatial morphology and temporal evolution. This is particularly effective for flow boiling, where regime identity is governed by dynamic processes such as bubble growth, coalescence, vapor redistribution, wave propagation, and annular film fluctuation. As a result, the temporal Transformer provides the highest classification accuracy among the Transformer-based models, reaching 99.2% under the present offline evaluation. However, this accuracy advantage comes at the cost of increased latency. The model requires event-frame sequence construction before inference and attention-based processing across multiple temporal representations, resulting in a processing time of 4.72 ms and an inference time of 7.31 ms. The same accumulation-window limitation applies to this model because its input sequence is also constructed from regime-specific event frames. Therefore, although the temporal Transformer demonstrates strong spatiotemporal representation capability, its reported performance should not be interpreted as a direct measure of fully blind online deployment. Its event-frame construction and higher computational cost also make it less suitable than the raw event LSTM for continuous low latency inference.

The direct raw event Transformer represents the opposite design choice. Instead of reconstructing event frames, individual raw events are directly used as Transformer tokens. This preserves the native asynchronous format of the event stream and eliminates the preprocessing cost associated with event-frame generation. In the tested lightweight implementation, each raw event is treated as an individual Transformer token, and each input sequence contains 1000 temporally ordered event tokens. The model therefore applies self-attention directly across the raw event sequence without grouping events or reconstructing event frames. This compact configuration results in substantially lower latency, with a processing time of 0.15 ms and an inference time of 0.96 ms. The model achieves a classification accuracy of 64.3%, which is substantially lower than those of the event-frame-based Transformer models. This result indicates that the compact architecture does not extract sufficient regime-dependent spatial morphology and temporal organization from the short raw event sequence.

However, the low computational cost of the direct raw event Transformer should not be interpreted as evidence that direct raw event attention is automatically superior for real-time classification. The tested model is intentionally compact, using a short 1000 event sequence and a single Transformer block. Unlike event frame-based models, it learns spatial morphology and temporal organization directly from sparse point events. It also lacks the sequential accumulation bias of the LSTM. Consequently, achieving accuracy comparable to the frame-based Vision Transformer or temporal Transformer would likely require longer event sequences, stronger time-position encoding, or a larger architecture. These changes would increase inference costs and reduce the latency advantage observed in the compact implementation. Because only one compact configuration is evaluated, the present result does not establish the general performance limit of direct raw event Transformer architectures. A more complete assessment would require controlled evaluation of sequence length, temporal encoding, model depth, and regime-wise classification errors.

These comparisons highlight a central trade-off in event-driven flow regime classification. Event frame-based Transformers provide strong classification performance because they transform sparse event streams into structured spatial or spatiotemporal representations. However, this transformation introduces additional preprocessing and increases deployment complexity. The high offline accuracy of these models also depends on regime-specific accumulation, which is not directly available before classification during blind deployment. The direct raw event Transformer minimizes preprocessing by preserving the native event representation, but its accuracy is limited by the difficulty of learning regime morphology directly from sparse event tokens. The raw event LSTM remains the most practical real-time architecture because it directly operates on event sequences while naturally accumulating temporal information with relatively low computational cost. It also avoids both event-frame reconstruction and regime-informed accumulation-window selection.

Overall, the Transformer-based models demonstrate the value of attention mechanisms for event-driven flow regime classification. The temporal Transformer provides the strongest offline classification performance, while the frame-based Vision Transformer confirms the importance of spatial event morphology. The direct raw event Transformer demonstrates that event-level attention can be implemented with low computational latency, although the present compact architecture does not provide sufficient classification accuracy. Therefore, the LSTM remains the primary architecture for live real-time deployment, while the Transformer models are used to benchmark how different attention-based representations trade off accuracy, latency, and model complexity. Accordingly, the Transformer results are interpreted as a comparative representation study that examines the roles of spatial attention, temporal attention, and direct raw event attention in flow regime classification.

Table 7. Performance Comparison of Transformer Event Representations

Model	Accuracy	Processing time	Inference time	Model size
Frame-based Vision Transformer	98.0%	3.11 ms	3.01 ms	8.66 MB
Temporal Transformer	99.2%	4.72 ms	7.31 ms	2.77 MB
Direct raw event Transformer	64.3%	0.15 ms	0.96 ms	0.16 MB

5.5 Conclusion

This chapter presented a real-time flow regime classification framework based on neuromorphic event sensing and machine learning. Building on the event-based activity analysis developed in the previous chapter, the framework used event streams as direct inputs for regime prediction and compared multiple learning approaches across optical and event-based representations. By leveraging the sparse and asynchronous nature of event-camera data, the proposed approach reduced the reliance on dense frame-based inputs and provided a more temporally responsive representation of rapidly evolving boiling dynamics.

Among the evaluated models, the Event LSTM provided the best balance between classification accuracy, inference speed, and processing efficiency. Unlike event-frame-based approaches that require event accumulation or reconstruction, the Event LSTM directly processed raw event sequences and preserved the temporal ordering of event activity. This capability enabled low latency classification while maintaining stable performance across multiple flow regimes, including transitional and unstable patterns that are difficult to distinguish using static image information alone.

The Transformer-based extensions further demonstrate that attention mechanisms provide useful representations of spatial and temporal event information. The frame-based Vision Transformer achieves 98.0% accuracy, while the temporal Transformer provides the highest offline classification accuracy of 99.2% by combining event-frame morphology with temporal attention. However, both models depend on event-frame construction and the regime-specific accumulation procedure used in the present representation study. The compact direct raw event Transformer removes this requirement and achieves low computational latency, but its accuracy of 64.3% remains insufficient for deployment. These results distinguish offline classification performance from real-time implementation suitability and further support the selection of the raw event LSTM for live operation.

This chapter also demonstrated the feasibility of online deployment through an asynchronous real-time pipeline that integrates event acquisition, preprocessing, inference, output smoothing, and live visualization. The use of a single-item queue helped prioritize the most recent event sequence and prevented processing delays from accumulating during continuous operation. In addition, majority-voting smoothing improved prediction stability by reducing short-term fluctuations in the output. Although the real-time experimental demonstration is currently limited to a subset of regimes available in the present facility, the framework shows strong potential for extension to broader operating conditions and more diverse flow patterns.

Overall, the findings of this chapter demonstrate that event-based sensing can support both high-accuracy offline regime representation and low latency real-time classification in boiling systems. In contrast to conventional frame-based approaches that rely on dense image sequences, the proposed event-driven framework captures dynamic flow information through sparse temporal measurements. This work advances the dissertation from offline image-based analysis and event-derived activity characterization toward real-time boiling diagnostics, providing a foundation for future closed-loop thermal control, instability detection, and intelligent multiphase flow monitoring.

CHAPTER 6: Summary and Conclusions

This dissertation presents a vision-based and event-based framework for analyzing flow boiling heat transfer through image-derived interfacial features, vision-based modeling, neuromorphic activity representation, and real-time flow regime classification. The central objective of this work is to move boiling analysis beyond conventional bulk measurements by directly extracting physically meaningful information from visual and event-based data. Across the dissertation, high-speed imaging, computer vision, machine learning, and neuromorphic sensing are used to quantify bubble morphology, interfacial dynamics, heat transfer behavior, boiling activity, and flow regime evolution.

The work begins by establishing a flow boiling experimental platform for high-speed optical and neuromorphic event-based visualization. This platform provides controlled hydrodynamic and thermal conditions for studying vapor generation, bubble transport, and interfacial activity in a confined channel. While the microgravity heat transfer modeling in Chapter 3 is performed using flow boiling datasets obtained from Purdue University, the experimental platform developed in this dissertation provides the basis for the event-camera activity analysis and real-time classification studies presented in Chapters 4 and 5.

Building on high-speed flow visualization data, a vision-based bubble digitization framework is developed to convert raw boiling images into quantitative interfacial descriptors. The framework combines segmentation, tracking, motion estimation, and feature extraction to identify bubbles and vapor structures across time. Compared with conventional manual or threshold-based image processing, the proposed approach enables more scalable and systematic extraction of bubble-level and interface-level information. These descriptors provide a direct link between visual observations and the underlying physical behavior of boiling flows.

The image-derived feature concept is then applied to vision-based modeling of microgravity flow boiling heat transfer. Under microgravity conditions, buoyancy-driven bubble departure is suppressed, causing vapor structures to remain near the heated surface, coalesce, and slide along the channel. This makes interfacial dynamics especially important for determining heat transfer performance. The dissertation shows that conventional heat transfer coefficient correlations can estimate average behavior but generally fail to capture the downstream decline in local heat transfer coefficient caused by vapor accumulation and reduced liquid contact. To address this limitation, a revised HTC model is developed by incorporating image-derived wetting and dry-out exposure times. By explicitly accounting for alternating wet and dry surface states, the model provides a more physically consistent representation of local heat transfer behavior.

The same feature-informed perspective is applied to critical heat flux prediction. Classical CHF models often rely on prescribed constants or idealized assumptions regarding interfacial structure. In this dissertation, image-derived quantities such as wetting front ratio, vapor layer thickness, and critical wavelength are incorporated into mechanistic CHF models, including the Interfacial Lift-off Model and the Hydrodynamic Instability-based Model. The results show that replacing fixed or assumed parameters with experimentally measured interfacial descriptors improves the physical interpretability of CHF prediction. Remaining discrepancies, particularly at lower mass flow rates, highlight the importance of imaging-window limitations and post-processing accuracy when extracting wavelength and wetting statistics from visual data.

In addition to frame-based imaging, this dissertation investigates neuromorphic event sensing as a new modality for flow boiling analysis. Event cameras record asynchronous brightness changes rather than dense image frames, producing sparse data streams with high temporal resolution and reduced redundancy. Chapter 4 demonstrates that event-camera measurements contain systematic information about flow boiling activity. Event-derived descriptors capture temporal intensity, burst-like intermittency, spatial redistribution, streamwise organization, and activity-state transitions. These results show that event streams are not merely sparse visual data, but compact representations of dynamic boiling activity.

Finally, the dissertation extends event-based sensing from activity characterization to real-time flow regime classification. Multiple learning architectures are evaluated using optical, event-frame, and raw event representations. These models include optical CNNs, event-frame CNNs, Fourier-based methods, spiking neural networks, event-sequence models, and Transformer-based extensions. The frame-based Vision Transformer and temporal Transformer demonstrate that spatial and temporal attention can provide strong offline classification performance, achieving accuracies of 98.0% and 99.2%, respectively. However, these models require event-frame construction and are evaluated using the regime-specific accumulation procedure developed for representation analysis. The compact direct raw event Transformer removes frame reconstruction but achieves lower accuracy of 64.3%, indicating that additional temporal context and representational capacity are needed for direct event-level attention. Among the evaluated approaches, the Event LSTM provides the best balance between classification accuracy, processing speed, and real-time feasibility because it directly processes raw event sequences without requiring event-frame reconstruction. The real-time implementation integrates event acquisition, inference, output smoothing, and visualization in an asynchronous pipeline, demonstrating the potential of neuromorphic sensing for continuous boiling diagnostics and intelligent thermal management.

Taken together, the results of this dissertation establish a unified pathway from visual observation to quantitative and actionable boiling diagnostics. High-speed imaging and computer vision provide access to bubble morphology, wetting behavior, vapor accumulation, and interfacial structure that are not directly resolved by conventional bulk measurements. These image-derived features improve the interpretation of heat transfer coefficient degradation and critical heat flux behavior by connecting local liquid-vapor dynamics with macroscopic thermal performance. Complementing this frame-based approach, neuromorphic event sensing provides a sparse and temporally resolved representation of dynamic interfacial activity. The event-derived descriptors capture changes in boiling activity and support low latency flow regime classification, demonstrating that event streams can serve as an informative sensing modality rather than simply a data-efficient alternative to conventional images.

More broadly, this dissertation shows that the value of visual sensing in flow boiling lies not only in observing interfaces, but in converting their evolving structures and dynamics into measurable descriptors that can support physical interpretation, prediction, and monitoring. The proposed methods are intended as feature-informed and experimentally grounded frameworks rather than universal correlations. Their broader contribution is to provide a transferable methodology for linking visual and event-based measurements with thermal-fluid behavior in systems where interfacial motion, vapor accumulation, wetting, and instability govern performance.

Several opportunities remain for future work. Broader datasets spanning different working fluids, channel geometries, heat fluxes, mass fluxes, and gravity conditions are needed to assess the generality of the proposed frameworks. Wider fields of view, multi-view imaging, and improved feature-extraction methods could reduce uncertainty for elongated, overlapping, or partially visible vapor structures. For event-based sensing, adaptive filtering, sensor-bias control, and direct event-based flow measurement may further improve robustness under changing illumination and high-activity conditions. In addition, the event-driven classification framework can be deployed on FPGA platforms, neuromorphic processors, or edge-AI hardware to enable low power, low latency inference directly from event streams without conventional frame reconstruction. Integrating this hardware implementation with regime-aware feedback control could enable thermal systems that detect developing instability and respond before performance degradation or dry-out occurs.

In conclusion, this dissertation advances flow-boiling analysis from bulk-condition-based interpretation toward interface-resolved, data-informed, and real-time diagnostics. By integrating high-speed visualization, computer vision, mechanistic heat-transfer modeling, neuromorphic event sensing, and event-driven learning, this work demonstrates how boiling interfaces can be transformed from qualitative visual phenomena into quantitative physical information. This capability provides a foundation for more interpretable thermal-fluid models, more responsive monitoring systems, and ultimately more reliable high-power thermal-management technologies.

REFERENCES

1. Qu W, Mudawar I. Flow boiling heat transfer in two-phase micro-channel heat sinks—I. Experimental investigation and assessment of correlation methods. *Int J Heat Mass Transf*. 2003;46(15):2755-2771.
2. Kharangate CR, O'Neill LE, Mudawar I, et al. Flow boiling and critical heat flux in horizontal channel with one-sided and double-sided heating. *Int J Heat Mass Transf*. 2015;90:323-338. doi:10.1016/j.ijheatmasstransfer.2015.06.073
3. Pop E. Energy dissipation and transport in nanoscale devices. *Nano Res*. *Tsinghua University Press*. 2010;3(3):147-169. doi:10.1007/s12274-010-1019-z
4. Kakaç S, Bon B. A review of two-phase flow dynamic instabilities in tube boiling systems. *Int J Heat Mass Transf*. 2008;51(3-4):399-433.
5. Collier JG, Thome JR. *Convective Boiling and Condensation*. Clarendon Press; 1994.
6. Prajapati YK, Bhandari P. Flow boiling instabilities in microchannels and their promising solutions–A review. *Exp Therm Fluid Sci*. 2017;88:576-593.
7. Chang S, Suh Y, Shingote C, et al. BubbleMask: Autonomous visualization of digital flow bubbles for predicting critical heat flux. *Int J Heat Mass Transf*. 2023;217:124656.
8. Suh Y, Chang S, Simadiris P, et al. VISION-iT: A framework for digitizing bubbles and droplets. *Energy and AI*. 2024;15:100309.
9. Suh Y, Chandramowlishwaran A, Won Y. Recent progress of artificial intelligence for liquid-vapor phase change heat transfer. *NPJ Comput Mater*. 2024;10(1):65.
10. Kandlikar SG. Fundamental issues related to flow boiling in minichannels and microchannels. *Exp Therm Fluid Sci*. 2002;26(2-4):389-407.
11. Dhir VK. Boiling heat transfer. *Annu Rev Fluid Mech*. 1998;30(1):365-401.
12. Thome JR, Consolini L. Mechanisms of boiling in micro-channels: critical assessment. *Heat Transfer Engineering*. 2010;31(4):288-297.
13. Yuan D, Chen D, Yan X, Xu J, Lu Q, Huang Y. Bubble behavior and its contribution to heat transfer of subcooled flow boiling in a vertical rectangular channel. *Ann Nucl Energy*. 2018;119:191-202.
14. Ren T, Zhu Z, Zhang R, Shi J, Yan C. Visualization experiment of bubble coalescence in a narrow vertical rectangular channel. *Front Energy Res*. 2020;8:96.
15. Liang G, Mudawar I. Pool boiling critical heat flux (CHF)–Part 1: Review of mechanisms, models, and correlations. *Int J Heat Mass Transf*. 2018;117:1352-1367.
16. Liu H, Chen D, Qin J, Zhao E, Yan P, Liu H. Visual experimental study on bubble behavior from nucleation site in vertical rectangular channel. *Appl Therm Eng*. 2022;201:117811.
17. Sadaghiani AK, Altay R, Noh H, et al. Effects of bubble coalescence on pool boiling heat transfer and critical heat flux–A parametric study based on artificial cavity geometry and surface wettability. *Int J Heat Mass Transf*. 2020;147:118952.
18. Paz C, Conde M, Porteiro J, Concheiro M. On the application of image processing methods for bubble recognition to the study of subcooled flow boiling of water in rectangular channels. *Sensors*. 2017;17(6):1448.
19. Xiao J, Zhang J. Experimental investigation on flow boiling bubble motion under ultrasonic field in vertical minichannel by using bubble tracking algorithm. *Ultrason Sonochem*. 2023;95:106365.

20. Seong JH, Ravichandran M, Su G, Phillips B, Bucci M. Automated bubble analysis of high-speed subcooled flow boiling images using U-net transfer learning and global optical flow. *International Journal of Multiphase Flow*. 2023;159:104336.
21. He Y, Hu C, Li H, et al. A flexible image processing technique for measuring bubble parameters based on a neural network. *Chemical Engineering Journal*. 2022;429:132138.
22. Soibam J, Scheiff V, Aslanidou I, Kyprianidis K, Fdhila RB. Application of deep learning for segmentation of bubble dynamics in subcooled boiling. *International Journal of Multiphase Flow*. 2023;169:104589.
23. Xiao J, Zhu M, Zhang J, Luo X. Characteristics of confined bubble behavior and enhanced flow boiling heat transfer in vertical minichannels under ultrasonic field by using bubble edge detection method. *Int J Heat Mass Transf*. 2026;255:127779.
24. Leong KC, Ho JY, Wong KK. A critical review of pool and flow boiling heat transfer of dielectric fluids on enhanced surfaces. *Appl Therm Eng*. 2017;112:999-1019.
25. Mudawar I. Two-phase microchannel heat sinks: theory, applications, and limitations. Published online 2011.
26. Kejia L, Xiong Z, Shuqi M, et al. Prediction of critical heat flux in a rod bundle channel with spacer grids based on the Eulerian two-fluid model. *Front Energy Res*. 2025;12:1366902.
27. Xie S, Beni MS, Cai J, Zhao J. Review of critical-heat-flux enhancement methods. *Int J Heat Mass Transf*. 2018;122:275-289.
28. Kim SJ, Bang IC, Buongiorno J, Hu LW. Effects of nanoparticle deposition on surface wettability influencing boiling heat transfer in nanofluids. *Appl Phys Lett*. 2006;89(15).
29. O'Hanley H, Coyle C, Buongiorno J, et al. Separate effects of surface roughness, wettability, and porosity on the boiling critical heat flux. *Appl Phys Lett*. 2013;103(2).
30. Chu KH, Soo Joung Y, Enright R, Buie CR, Wang EN. Hierarchically structured surfaces for boiling critical heat flux enhancement. *Appl Phys Lett*. 2013;102(15).
31. Kim HD, Kim MH. Effect of nanoparticle deposition on capillary wicking that influences the critical heat flux in nanofluids. *Appl Phys Lett*. 2007;91(1).
32. Rahman MM, Olceroglu E, McCarthy M. Role of wickability on the critical heat flux of structured superhydrophilic surfaces. *Langmuir*. 2014;30(37):11225-11234.
33. Nazari A, Saedodin S. Critical heat flux enhancement of pool boiling using a porous nanostructured coating. *Experimental Heat Transfer*. 2017;30(4):316-327.
34. Tan L, Chen C, Dong X, Gong Z, Wang M. Experimental study on CHF of R134a flow boiling in a horizontal helically-coiled tube near the critical pressure. *Exp Therm Fluid Sci*. 2017;82:472-481.
35. Weisman J, Pei BS. Prediction of critical heat flux in flow boiling at low qualities. *Int J Heat Mass Transf*. 1983;26(10):1463-1477.
36. Lee CH, Mudawwar I. A mechanistic critical heat flux model for subcooled flow boiling based on local bulk flow conditions. *International Journal of Multiphase Flow*. 1988;14(6):711-728.
37. Kutateladze SS, Leont'ev AI. Some applications of the asymptotic theory of the turbulent boundary layer. In: *International Heat Transfer Conference Digital Library*. Begel House Inc.; 1966.
38. Galloway JE, Mudawar I. CHF mechanism in flow boiling from a short heated wall—II. Theoretical CHF model. *Int J Heat Mass Transf*. 1993;36(10):2527-2540.
39. Galloway JE, Mudawar I. CHF mechanism in flow boiling from a short heated wall-part 1. Examination of near-wall conditions with the aid of photomicrography and high-speed video imaging. *Int J Heat Mass Transfer*. 1993;36:2511-2526.

40. Armand AA, Treščev GG. *Investigation of the Resistance during the Movement of Steam-Water Mixtures in a Heated Boiler Pie at High Pressure*. Atomic Energy Research Establishment; 1959.
41. Zivi SM. Estimation of steady-state steam void-fraction by means of the principle of minimum entropy production. Published online 1964.
42. Fauske H. Critical two-phase, steam–water flows. *Proceedings of the 1961 Heat Transfer and Fluid Mechanics Institute Stanford University Press, Stanford, CA*. Published online 1961:79-89.
43. Smith SL. Void fractions in two-phase flow: a correlation based upon an equal velocity head model. *Proceedings of the Institution of Mechanical Engineers*. 1969;184(1):647-664.
44. Zuber N, Findlay JA. Average volumetric concentration in two-phase flow systems. Published online 1965.
45. Rouhani SZ, Axelsson E. Calculation of void volume fraction in the subcooled and quality boiling regions. *Int J Heat Mass Transf.* 1970;13(2):383-393.
46. Kawahara A, Chung PY, Kawaji M. Investigation of two-phase flow pattern, void fraction and pressure-drop in a microchannel. *International journal of multiphase flow*. 2002;28(9):1411-1435.
47. Huq R, Loth JL. Analytical two-phase flow void prediction method. *J Thermophys Heat Trans*. 1992;6(1):139-144.
48. Zhang H, Mudawar I, Hasan MM. Assessment of dimensionless CHF correlations for subcooled flow boiling in microgravity and Earth gravity. *Int J Heat Mass Transf.* 2007;50(23-24):4568-4580.
49. Lazarek GM, Black SH. Evaporative heat transfer, pressure-drop and critical heat flux in a small vertical tube with R-113. *Int J Heat Mass Transf.* 1982;25(7):945-960.
50. Tran TN, Wambsganss MW, France DM. Small circular-and rectangular-channel boiling with two refrigerants. *International Journal of Multiphase Flow*. 1996;22(3):485-498.
51. Warrier GR, Dhir VK, Momoda LA. Heat transfer and pressure-drop in narrow rectangular channels. *Exp Therm Fluid Sci*. 2002;26(1):53-64.
52. Yu W, France DM, Wambsganss MW, Hull JR. Two-phase pressure-drop, boiling heat transfer, and critical heat flux to water in a small-diameter horizontal tube. *International Journal of Multiphase Flow*. 2002;28(6):927-941.
53. Shah MM. Chart correlation for saturated boiling heat transfer: equations and further study. *ASHRAE Trans;(United States)*. 1981;88(CONF-820112-).
54. Agostini B, Bontemps A. Vertical flow boiling of refrigerant R134a in small channels. *Int J Heat Fluid Flow*. 2005;26(2):296-306.
55. Cooper MG. Saturation nucleate pool boiling-a simple correlation. In: *IChemE Symp. Ser.* Vol 86. 1984:786.
56. Hamdar M, Zoughaib A, Clodic D. Flow boiling heat transfer and pressure-drop of pure HFC-152a in a horizontal mini-channel. *International Journal of Refrigeration*. 2010;33(3):566-577.
57. Kenning DBR, Cooper MG. Saturated flow boiling of water in vertical tubes. *Int J Heat Mass Transf.* 1989;32(3):445-458.
58. Sun L, Mishima K. An evaluation of prediction methods for saturated flow boiling heat transfer in mini-channels. *Int J Heat Mass Transf.* 2009;52(23-24):5323-5329.
59. Naphon P, Wiriyasart S, Arisariyawong T. Artificial neural network analysis the pulsating Nusselt number and friction factor of TiO2/water nanofluids in the spirally coiled tube with magnetic field. *Int J Heat Mass Transf.* 2018;118:1152-1159.

60. Mehrabi M, Sharifpur M, Meyer JP. Modelling and multi-objective optimisation of the convective heat transfer characteristics and pressure-drop of low concentration TiO2–water nanofluids in the turbulent flow regime. *Int J Heat Mass Transf*. 2013;67:646-653.
61. Hughes MT, Kini G, Garimella S. Status, challenges, and potential for machine learning in understanding and applying heat transfer phenomena. *J Heat Transfer*. 2021;143(12):120802.
62. Lee J, Suh Y, Dubey PP, Barako MT, Won Y. Capillary wicking in hierarchically textured copper nanowire arrays. *ACS Appl Mater Interfaces*. 2018;11(1):1546-1554.
63. Suh Y, Lee J, Simadiris P, et al. A Deep Learning Perspective on Dropwise Condensation (Adv. Sci. 22/2021). *Advanced Science*. 2021;8(22):2170153.
64. Kim SM, Mudawar I. Universal approach to predicting saturated flow boiling heat transfer in mini/micro-channels–Part II. Two-phase heat transfer coefficient. *Int J Heat Mass Transf*. 2013;64:1239-1256.
65. Li W, Wu Z. A general criterion for evaporative heat transfer in micro/mini-channels. *Int J Heat Mass Transf*. 2010;53(9-10):1967-1976.
66. Oh HK, Son CH. New correlation to predict the heat transfer coefficient in-tube cooling of supercritical CO2 in horizontal macro-tubes. *Exp Therm Fluid Sci*. 2010;34(8):1230-1241.
67. Liu Z, Winterton RHS. A general correlation for saturated and subcooled flow boiling in tubes and annuli, based on a nucleate pool boiling equation. *Int J Heat Mass Transf*. 1991;34(11):2759-2766.
68. Huang CN, Chang S, Suh Y, Mudawar I, Won Y, Kharangate CR. Machine learning boiling prediction: From autonomous vision of flow visualization data to performance parameter theoretical modeling. *International Journal of Multiphase Flow*. 2024;179:104928.
69. Wang Y, Lv K, Huang R, Song S, Yang L, Huang G. Glance and focus: a dynamic approach to reducing spatial redundancy in image classification. *Adv Neural Inf Process Syst*. 2020;33:2432-2444.
70. Chang S, Arani S, Nuthalapati NS, et al. EventFlow: Real-time neuromorphic event-driven classification of two-phase boiling flow regimes. *Droplet*. Published online 2026:e70066.
71. Furmonas J, Liobe J, Barzdenas V. Analytical review of event-based camera depth estimation methods and systems. *Sensors*. 2022;22(3):1201.
72. Lu D, Suh Y, Won Y. Rapid identification of boiling crisis with event-based visual streaming analysis. *Appl Therm Eng*. 2024;239:122004.
73. Vasco V, Glover A, Mueggler E, Scaramuzza D, Natale L, Bartolozzi C. Independent motion detection with event-driven cameras. In: *2017 18th International Conference on Advanced Robotics (ICAR)*. IEEE; 2017:530-536.
74. Xu L, Xu W, Golyanik V, Habermann M, Fang L, Theobalt C. Eventcap: Monocular 3d capture of high-speed human motions using an event camera. In: *Proceedings of the IEEE/CVF Conference on Computer Vision and Pattern Recognition*. 2020:4968-4978.
75. Iaboni C, Patel H, Lobo D, Choi JW, Abichandani P. Event camera based real-time detection and tracking of indoor ground robots. *IEEE Access*. 2021;9:166588-166602.
76. Glover A, Bartolozzi C. Robust visual tracking with a freely-moving event camera. In: *2017 IEEE/RSJ International Conference on Intelligent Robots and Systems (IROS)*. IEEE; 2017:3769-3776.
77. Chen G, Cao H, Conradt J, Tang H, Rohrbein F, Knoll A. Event-based neuromorphic vision for autonomous driving: A paradigm shift for bio-inspired visual sensing and perception. *IEEE Signal Process Mag*. 2020;37(4):34-49.

78. Li J, Dong S, Yu Z, Tian Y, Huang T. Event-based vision enhanced: A joint detection framework in autonomous driving. In: *2019 Ieee International Conference on Multimedia and Expo (Icme)*. IEEE; 2019:1396-1401.
79. Zhang J, Yang K, Stiefelhagen R. Exploring event-driven dynamic context for accident scene segmentation. *IEEE Transactions on Intelligent Transportation Systems*. 2021;23(3):2606-2622.
80. Shannon CE. A mathematical theory of communication. *The Bell system technical journal*. 1948;27(3):379-423.
81. Pielou EC. The measurement of diversity in different types of biological collections. *J Theor Biol*. 1966;13:131-144.
82. Vranken I, Baudry J, Aubinet M, Visser M, Bogaert J. A review on the use of entropy in landscape ecology: heterogeneity, unpredictability, scale dependence and their links with thermodynamics. *Landsc Ecol*. 2015;30(1):51-65.
83. Wold S, Esbensen K, Geladi P. Principal component analysis. *Chemometrics and intelligent laboratory systems*. 1987;2(1-3):37-52.
84. Jolliffe I. Principal Component Analysis. In: *International Encyclopedia of Statistical Science*. Springer; 2025:1945-1948.
85. Abdi H, Williams LJ. Principal component analysis. *Wiley Interdiscip Rev Comput Stat*. 2010;2(4):433-459.
86. Thome JR. The new frontier in heat transfer: Microscale and nanoscale technologies. *Heat Transfer Engineering*. 2006;27(9):1-3. doi:10.1080/01457630600845283
87. Mudawar I. *Assessment of High-Heat-Flux Thermal Management Schemes*. Vol 24. 2001.
88. Zhang Q, Mo D, Moon S, et al. Bubble nucleation and growth on microstructured surfaces under microgravity. *NPJ Microgravity*. 2024;10(1):13.
89. Lee HJ, Lee SY. Heat transfer correlation for boiling flows in small rectangular horizontal channels with low aspect ratios. *International Journal of Multiphase Flow*. 2001;27(12):2043-2062.
90. Gungor KE, Winterton RHS. A general correlation for flow boiling in tubes and annuli. *Int J Heat Mass Transf*. 1986;29(3):351-358.
91. Reid RS, Pate MB, Bergles AE. *Evaporation of Refrigerant 113 Flowing inside Smooth Tubes*. American Society of Mechanical Engineers, New York, NY; 1987.
92. Carey VP, Tervo P, Shollenberger K. Partial dryout in enhanced evaporator tubes and its impact on heat transfer performance. In: *International Congress & Exposition*. 1992.
93. Hewitt G. Gas-liquid flow. In: *Thermopedia*. Begel House Inc.; 2011.
94. Kim SM, Mudawar I. Theoretical model for local heat transfer coefficient for annular flow boiling in circular mini/micro-channels. *Int J Heat Mass Transf*. 2014;73:731-742.
95. Kong R, Kim S. Characterization of horizontal air–water two-phase flow. *Nuclear Engineering and Design*. 2017;312:266-276.
96. Emamzadeh M, Issa RI. A model for predicting the transition between stratified and annular flow in horizontal pipes. *Multiphase Science and Technology*. 2013;25(1).
97. Wang Y, Yu Y, Liu Z, Chang Y, Zhao X, Wang Q. Experimental Study on Gas-Liquid Two-Phase Stratified Flow at High Pressure in a Horizontal Pipe. *Energies (Basel)*. 2024;17(5):1056.
98. O'Neill LE, Mudawar I. Review of two-phase flow instabilities in macro-and micro-channel systems. *Int J Heat Mass Transf*. 2020;157:119738.
99. Hernández L, Enrique Julia J, Ozar B, Hibiki T, Ishii M. Flow regime identification in boiling two-phase flow in a vertical annulus. Published online 2011.

100. Huo X, Chen L, Tian YS, Karayiannis TG. Flow boiling and flow regimes in small diameter tubes. *Appl Therm Eng*. 2004;24(8-9):1225-1239.
101. Ooi ZJ, Zhu L, Bottini JL, Brooks CS. Identification of flow regimes in boiling flows in a vertical annulus channel with machine learning techniques. *Int J Heat Mass Transf*. 2022;185:122439.
102. Nnabuife SG, Pilario KES, Lao L, Cao Y, Shafiee M. Identification of gas-liquid flow regimes using a non-intrusive Doppler ultrasonic sensor and virtual flow regime maps. *Flow Measurement and Instrumentation*. 2019;68:101568.
103. Hobold GM, da Silva AK. Machine learning classification of boiling regimes with low speed, direct and indirect visualization. *Int J Heat Mass Transf*. 2018;125:1296-1309.
104. Hervieu E. Identification of gas-liquid flow regimes from a space-frequency representation by use of an impedance probe and a neural network. In: *Fluids Engineering Division Summer Meeting*. Vol 36169. 2002:685-691.
105. Jombo G, Zhang Y. Acoustic-based machine condition monitoring—methods and challenges. *Eng*. 2023;4(1):47-79.
106. Kadish S, Schmid D, Son J, Boje E. Computer vision-based classification of flow regime and vapor quality in vertical two-phase flow. *Sensors*. 2022;22(3):996.
107. Nie F, Wang H, Song Q, Zhao Y, Shen J, Gong M. Image identification for two-phase flow patterns based on CNN algorithms. *International Journal of Multiphase Flow*. 2022;152:104067.
108. Schepperle M, Junaid S, Woias P. Computer-Vision-and Deep-Learning-Based Determination of Flow Regimes, Void Fraction, and Resistance Sensor Data in Microchannel Flow Boiling. *Sensors*. 2024;24(11):3363.
109. Rusch A, Rösgen T. TrackAER: real-time event-based quantitative flow visualization. *Exp Fluids*. 2023;64(8):136.
110. Willert CE, Klinner J. Event-based imaging velocimetry: an assessment of event-based cameras for the measurement of fluid flows. *Exp Fluids*. 2022;63(6):101.

APPENDIX A

A1. ML Vision Modeling

i. *Video Processing*

To create consistent image datasets, the videos are preprocessed of size and brightness. Image cropping is performed at the beginning and end of the channel where bubbles are not located, and the brightness of the video is adjusted to a fixed value to optimize a bubble contrast.

ii. *Model Training*

Table A1 summarizes the parameters used to train the Mask R-CNN model. Further discussions are provided elsewhere.[112]

Table A1. Model training process of Mask R-CNN

Modeling	Training Set	Test Set	Epoch	Learning Rate	Momentum	Test Loss
	3,440	860	100	0.0008	0.9	0.02

iii. *Model Evaluation*

To understand the model's prediction, the model performance is evaluated by analyzing standard evaluation metrics such as recall, precision, accuracy, F1 Score. These evaluate the segmentation performance through different combination of possible outcomes of predicted instances. In this study, we define a metric called MAPE defined elsewhere.[112–115] According to their respective definitions:[116]

$$Recall = \frac{\sum TP}{\sum(TP + FN)} \tag{A1}$$

$$Precision = \frac{\sum TP}{\sum(TP + FP)} \tag{A2}$$

$$Accuracy = \frac{\sum(TP + TN)}{\sum(TP + TN + FN + FP)} \tag{A3}$$

$$F - 1\,score = 2 \times \frac{Precision \times Recall}{Precision + Recall} \tag{A4}$$

where TP, FP, TN, and FN are true positive, false positive, true negative, and false negative, respectively.

In addition to these performance evaluation metrics, we define another metric called mean average pixel accuracy (MAPA) to evaluate the model prediction accuracy at the pixel-wise level. To define MAPA, we calculate a pixelwise error (PE) between the ground truth (GT) and predicted mask (PM) by subtracting the two images.[112–115,117]

$$PE_i = (GT_i - PM_i) \tag{A5}$$

where *i* is the number of instances in an image. Then, the mean average pixel error (MAPE) is calculated by dividing each PE by its respective GT:

$$MAPE = \frac{1}{n}\sum_{i=1}^{n} \left|\frac{PE_i}{GT_i}\right| \times 100 \tag{A6}$$

where n is the total number of images. Finally, MAPA is calculated as follows:

$$MAPA = 100 - MAPE \tag{A7}$$

The model demonstrated exceptional detection capabilities with values >87% for conventional metrics and an acceptably accurate indication as MAPA of >94%.

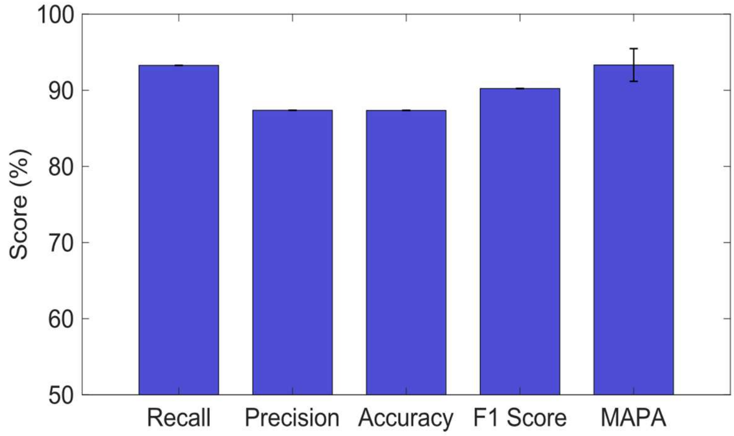

Figure A1. Instance-based prediction metrics including recall, precision, accuracy, F-1 Score, and MAPA. MAPA represents mean average pixel accuracy. These help us to evaluate the performance of the classification model.

A2. Image-Derived Feature Definitions

Bubble count is enumerated by counting each bubble in high-resolution images. The images are taken by high-speed camera of 2,000 frames per second with total of 3,000 images which allowed prominent vapor features to be carefully tracked with time. Our algorithm clarifies the bubbles and counts the total number of bubbles frame by frame during 1.5 seconds of total experimental time. The average bubble count per frame and the total number of bubbles information are automatically extracted.

Aspect ratio of bubbles are determined by dividing the length over height of created bounding boxes. Region of Interest Align (RoIAlign) functions create the bounding box referring to the border's coordinates that enclose an image. They are used to bind or identify a target and serve as reference point for object detection. By refining the coordinates of each box of bubble, the width and the height can be obtained.

Wetting front and interfacial length are calculated from binarized images from Mask-RCNN. Binarized images from Mask R-CNN allow us to identify the vapor and liquid; vapor (bubble) in white pixel, and liquid (working fluid) in black pixel. By tabulating the number of black and white pixels at the bottom of the channel, the wetting front is calculated, while interfacial length is identified by creating the boundary between the vapor and liquid during flow by using MATLAB. After tabulating all pixels, we convert pixel-wise length into mm-scale length.

Wavelength of each bubble is extracted from the bounding boxes as same method of aspect ratio. While mean vapor layer thickness is validated by in-house function which can analyze the perpendicular distance between the bottom wall and interfacial length of vapor. As all bubbles have irregular shape, not constant hemispherical shape, the results of vapor layer thickness are averaged from all local vapor layer thicknesses.

Vapor fraction is calculated by tabulating the ratio between the white pixels (vapor) and total pixels after binarizing tracked image sets.

Bubble velocity is determined by quantifying the movements of the centroid for each bubble and the time related to that movement. Tracked x and y coordinates of bubbles' centroid with specific Ids are used to find the moving distance for each bubble, and the velocity of each bubble are numerated. Another method to determine a bubble velocity is to use the bounding box by following the border edge of each bubble. We adopt to use the centroid to calculate velocity due to the irregular shapes of bubbles under microgravity condition. Bounding boxes for irregular shapes of bubbles show sudden movements in direction of the working fluid, which yield major changes in velocity.

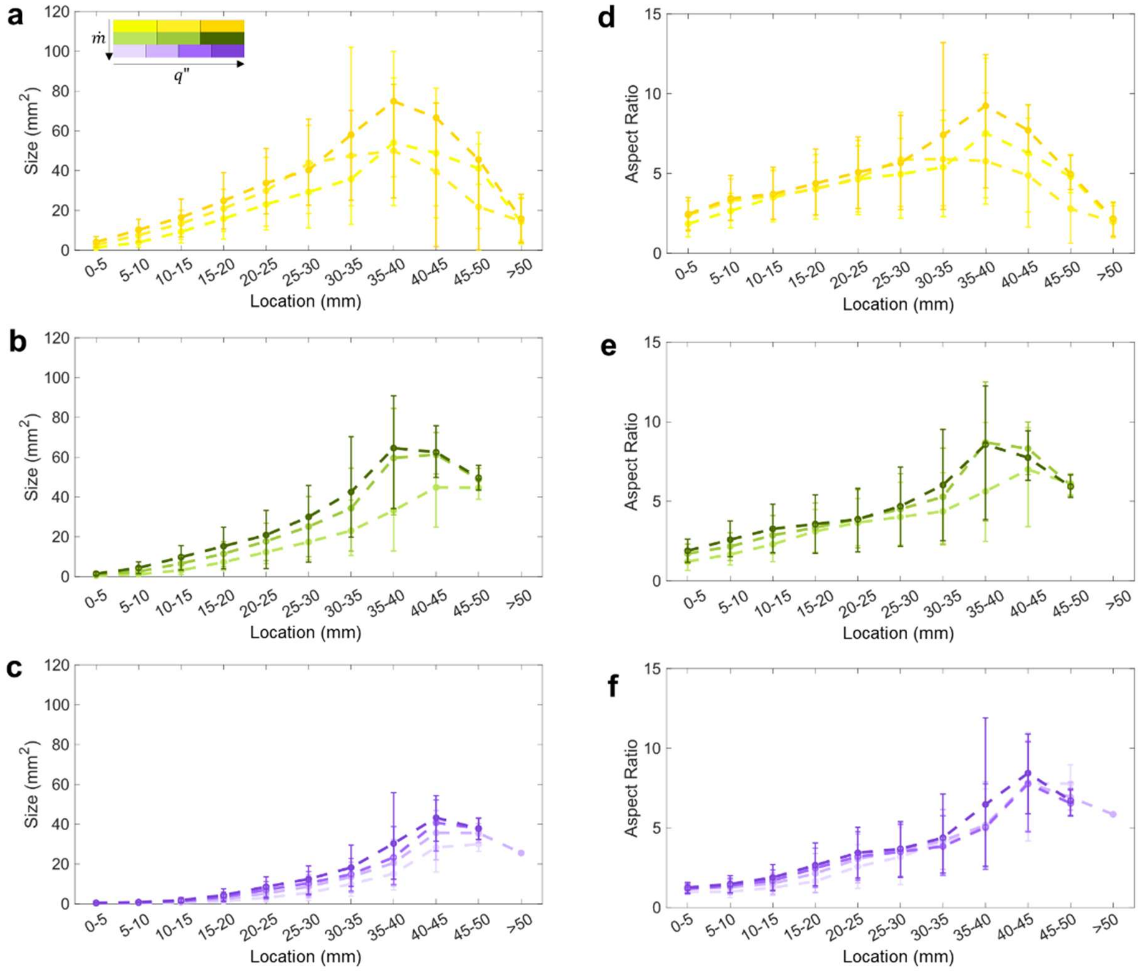

Figure A2. Local bubble sizes (a – c) and aspect ratio (d – f) for each mass flow rate (10 – 40 g/s). Showing an increasing trend until the cut-off point as the mass flow rates are increased. Error bars indicates 16th and 84th percentile of the data set.

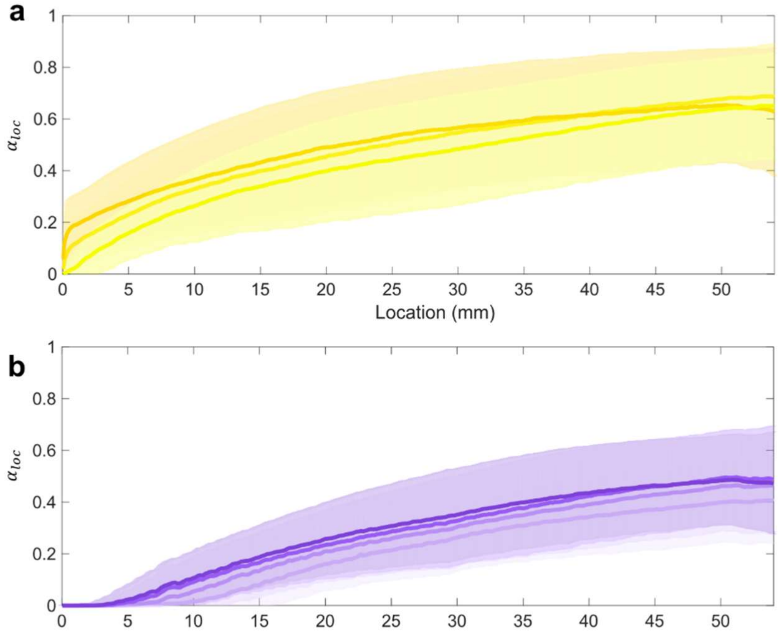

Figure A3. Local vapor fraction profile, α_{loc} of mass flow rate of (a) 10 g/s and (b) 40 g/s. The lines represent average values from 3,000 images, and planes represent one standard deviation for each heat flux.

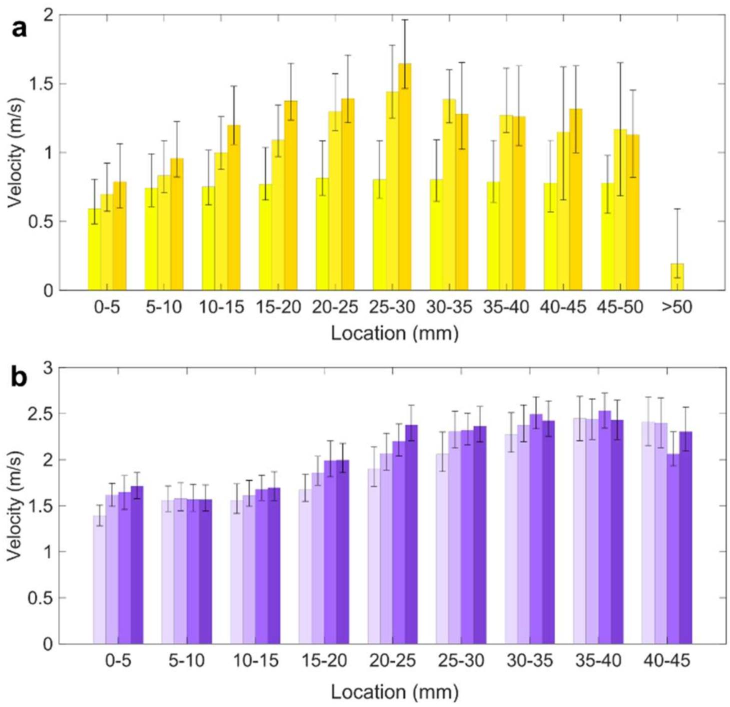

Figure A4. Local velocity profiles of mass flow rates of (a) 10 g/s and (b) 40 g/s based on centroid movements of bubbles. Individual bubble velocities increase in the direction of flow in the channel potentially due to bubble-bubble interactions. The filtered bubbles after 45 mm of channel are not depicted in (b). Error bars indicates 16th and 84th percentile of the data set.

A3. Review of Classical Void Fraction and Heat Transfer Coefficient Correlations

This appendix provides a literature review of classical void fraction and heat transfer coefficient correlations used in flow boiling analysis. The void fraction models include HEM, slip-ratio models, drift-flux models, empirical HEM-based correlations, and separated-flow formulations, which describe vapor-liquid phase distribution with different assumptions regarding phase velocity, slip, buoyancy, surface tension, and interfacial momentum transfer. The heat transfer coefficient correlations summarize widely used empirical and semi-empirical models based on dimensionless parameters such as Reynolds number, boiling number, Weber number, Prandtl number, density ratio, reduced pressure, and Martinelli parameter. These models serve as a conventional reference framework for CHF and HTC prediction and provide background for comparing physics-based correlations with vision- and event-based representations of boiling dynamics.

Homogeneous Equilibrium Model (HEM), the simplest and most widely used model, assumes that the vapor and liquid phases travel at the same velocity, which is generally valid for bubbly flows where velocity differences are minimal. [7]

$$\alpha = \frac{1}{1+\frac{\rho_g}{\rho_f}\left(\frac{1-x}{x}\right)S} \tag{A1}$$

where x is the quality and ρ is the density. In HEM, the velocities of the vapor phase and the liquid phase are assumed to be the same, leading to a velocity ratio, $S = u_g / u_f = 1$. This model is practical only when the velocity differences between phases is small or negligible usually in the bubbly regions of the flow.

Slip ratio models account for the velocity difference between vapor and liquid phases by introducing a phase velocity ratio based on kinetic energy or momentum flux principles. One widely used model defines the velocity ratio, S as $(\rho_f/\rho_g)^{1/3}$, derived from the assumption that a steady-state thermodynamic process minimizes entropy generation.[8] Another model estimates S as $(\rho_f/\rho_g)^{1/2}$, while an alternative approach equates the momentum fluxes of the two phases to determine the slip ratio.[9,10]

$$\alpha = \frac{1}{1+\left(\frac{1-x}{x}\right)\left(\frac{\rho_g}{\rho_f}\right)^{1/2}} \tag{A2}$$

Drift-flux models are considered more versatile than other void fraction models because they incorporate radial velocity distribution, surface tension, and buoyancy effects into their formulations. One foundational model in this category accounts for the effects of nonuniform flow and local relative velocity between the vapor and liquid phases.[11] Another formulation describes the detachment of vapor bubbles due to evaporation and includes calculations for the heat transfer rates in both phases, as well as the rate of vapor condensation within the liquid.[12]

$$\alpha = \frac{x}{\rho_g}\left\{[1+0.12(1-x)]\left(\frac{x}{\rho_g}+\frac{1-x}{\rho_f}\right)+\frac{1.18(1-x)\left[g\sigma(\rho_f-\rho_g)^{0.25}\right]}{G\rho_f^{0.5}}\right\}^{-1} \tag{A3}$$

Additional empirical correlations that are simple to apply have been developed as empirical calibrations of the *Homogeneous Equilibrium Mode*l (HEM).[13,14]

$$\alpha = 1-\frac{2(1-x)^2}{1-2x+\left[1+4x(1-x)\left(\frac{\rho_f}{\rho_{g-1}}\right)\right]^{0.5}} \tag{A4}$$

Besides these models, the *Separated Flow Model* (SFM) presents another approach, applying control volume analysis to separately solve the mass, momentum, and energy conservation equations for the vapor and liquid layers.[15] In SFM, the assumption of uniform axial velocities and pressure simplifies the analysis while allowing for velocity differences between the phases, making it particularly suitable for annular and stratified flow regimes. These theoretical frameworks provide important foundations for understanding and predicting void fraction behavior in flow boiling systems.

$$G^2 \frac{d}{dz}\left[\frac{{x_a}^2}{\rho_g \alpha_a}\right] = -\alpha_a \frac{dp}{dz} - \frac{\tau_{w,g} P_{w,g}}{A} \mp \frac{\tau_{ia} P_{ia}}{A} - \rho_g \alpha_a g \sin\theta \qquad \text{(A5)}$$

where $\tau_{w,k} = \frac{1}{2}\rho_k U_k^2 f_k$, $f_k = C_1 + \frac{C_2}{Re_{D_k}^{1/C_3}} = C_1 + \frac{C_2}{\left(\frac{\rho_k U_k D_k}{\mu_k}\right)^{\frac{1}{C_3}}}$, $k = f$ or g, and $D_k = 4A_k/P_k$

For laminar flow ($Re_{D_k} \leq 2100$), $C_1 = 0, C_2 = 16, C_3 = 1$

For transient flow ($2100 < Re_{D_k} \leq 4000$), $C_1 = 0.054, C_2 = 2.3 * 10^{-8}, C_3 = -\frac{2}{3}$

For turbulent flow ($Re_{D_k} > 4000$), $C_1 = 0.00128, C_2 = 0.1143, C_3 = 3.2154$

Table A2. Correlations for predicting heat transfer coefficient

References	Equations
Lazarek and Black[16]	$h_{Lazarek} = 30Bo^{0.714}\, Re_{fo}^{0.857} \frac{k_f}{D}$, $Re_{fo} = \frac{\rho_f u_f D}{\mu_f}$
Tran et al.[17]	$h_{Tran} = 8.4 \times 10^5 \left(Bo^2 We_f\right)^{0.3} \left(\frac{\rho_f}{\rho_g}\right)^{-0.4}$, $We_f = \frac{G^2 D}{\rho_f \sigma}$
Agostini and Bontemps[18]	$h_{Agostini} = \begin{cases} 28q''^{2/3} G^{-0.26} x^{-0.1}, \text{for } x < 0.43 \\ 28q''^{2/3} G^{-0.64} x^{-2.08}, \text{for } x > 0.43 \end{cases}$
Cooper[19]	$h_{Cooper} = 55P_R^{0.12}(-\log_{10} P_R)^{-0.55} M^{-0.5} q''^{0.67}$
Hamdar et al.[20]	$h_{Hamdar} = 6942.8\left(Bo^2 We_f\right)^{0.2415} \left(\frac{\rho_g}{\rho_f}\right)^{0.22652} \frac{k_f}{D}$
Kenning and Cooper[21]	$h_{Kenning} = (1 + 1.8X_{tt}^{-0.87})\left(0.023\, Re_f^{0.8}\, Pr_f^{0.4} \frac{k_f}{D}\right)$

Sun and Mishima[22]	$h_{Sun} = 6\left(Re_{fo}^{1.05}\, B\, o^{0.54} We_f^{-0.191}\right)\left(\frac{\rho_g}{\rho_f}\right)^{0.142}\frac{k_f}{D}$
Kim and Mudawar[23]	$h_{Kim} = \left(h_{nb}^2 + h_{cb}^2\right)^{0.5}$ $h_{cb} = \left[5.2\left(Bo\frac{P_H}{P_F}\right)^{0.08} We^{-0.54} + 3.5X_{tt}^{-0.94}\left(\frac{\rho_g}{\rho_f}\right)^{0.25}\right]\left(0.023\,\mathrm{Re}_f^{0.8}\,\mathrm{Pr}_f^{0.4}\frac{k_f}{D}\right)$ $h_{nb} = \left[2345\left(Bo\frac{P_H}{P_F}\right)^{0.7} P_R{}^{0.38}(1-x)^{-0.51}\right]\left(0.023\,Re_f^{0.8}\,Pr_f^{0.4}\frac{k_f}{D}\right)$ $Re_f = \frac{\rho_f u_f D_f}{\mu_f}\; Bo = \frac{q''}{Gh_{fg}}$
Li and Wu[24]	$h_{Li} = 334Bo^{0.3}\left(BdRe_f^{0.36}\right)^{0.4}\frac{k_f}{D}, Bd = \frac{g(\rho_f - \rho_g)D^2}{\sigma}$
Oh and Son[25]	$h_{Oh} = 0.034\,Re_f^{0.8}\,Pr_f^{0.3}(1.58X_{tt}^{-0.87})\left(\frac{k_f}{D}\right),$ $X_{tt} = \left(\frac{1-x}{x}\right)^{0.9}\left(\frac{\rho_f}{\rho_g}\right)^{0.5}\left(\frac{\mu_f}{\mu_g}\right)^{0.1}$
Warrier et al.[26]	$h_W = \left[1 + 6Bo^{\frac{1}{16}} - 5.3(1 - 855Bo)x^{0.65}\right]\left(0.023\,Re_f^{0.8}\,Pr_f^{0.4}\frac{k_f}{D}\right)$
Liu and Winterton[27]	$h_{Liu} = \left[\left(Eh_{sp}\right)^2 + (Sh_{nb})^2\right]^{0.5}$ $E = \left[1 + x\,Pr_f\left(\frac{\rho_f}{\rho_g} - 1\right)\right]^{0.35}$ $h_{sp} = 0.023\,Re_f^{0.8}\,Pr_f^{0.4}\frac{k_f}{D} S = \left(1 + 0.055E^{0.1}Re_f^{0.16}\right)^{-1},$ $h_{nb} = 55P_R^{0.12}(-\,log_{10}\,P_R)^{-0.55}M^{-0.5}q''^{0.67}$
Kew and Cornwell[28]	$h_{Kew} = 30\,\mathrm{Re}_{fo}^{0.857}\,Bo^{0.714}\left(\frac{1}{1-x}\right)^{0.143}\frac{k_f}{D}$

References

1. Suh, Y. *Deep Nuclei Tracking Framework for Phase-Change Heat and Mass Transfer*. (2023).
2. Suh, Y., Bostanabad, R. & Won, Y. Deep learning predicts boiling heat transfer. *Sci Rep* **11**, (2021).
3. Lee, J. *et al.* Computer vision-assisted investigation of boiling heat transfer on segmented nanowires with vertical wettability. *Nanoscale* **14**, 13078–13089 (2022).
4. Suh, Y. *et al.* A Deep Learning Perspective on Dropwise Condensation. *Advanced Science* **8**, (2021).
5. Fawcett, T. An introduction to ROC analysis. *Pattern Recognit Lett* **27**, 861–874 (2006).
6. Khodakarami, S., Fazle Rabbi, K., Suh, Y., Won, Y. & Miljkovic, N. Machine learning enabled condensation heat transfer measurement. *Int J Heat Mass Transf* **194**, (2022).
7. Armand, A. A. & Treščev, G. G. Investigation of the resistance during the movement of steam–water mixtures in a heated boiler pipe at high pressure. At. Energy Res. Establ. (1959).
8. Zivi, S. M. Estimation of steady-state steam void fraction by means of the principle of minimum entropy production. J. Heat Transfer 86, 247–251 (1964).
9. Fauske, H. Critical two-phase, steam–water flows. In Proc. Heat Transf. Fluid Mech. Inst. 79–89 (Stanford Univ. Press, 1961).
10. Smith, S. L. Void fractions in two-phase flow: a correlation based upon an equal velocity head model. Proc. Inst. Mech. Eng. 184, 647–664 (1969).
11. Zuber, N. & Findlay, J. A. Average volumetric concentration in two-phase flow systems. J. Heat Transf. 87, 453–468 (1965).
12. Rohuani, Z. & Axelsson, E. Calculation of volume void fraction in a subcooled and quality region. Int. J. Heat Mass Transf. 17, 383–393 (1970).
13. Kawahara, A., Chung, P. Y. & Kawaji, M. Investigation of two-phase flow pattern, void fraction and pressure-drop in a microchannel. Int. J. Multiphase Flow 28, 1411–1435 (2002).
14. Huq, R. & Loth, J. L. Analytical two-phase flow void prediction method. J. Thermophys. Heat Transf. 6, 139–144 (1992).
15. Zhang, H., Mudawar, I. & Hasan, M. M. Assessment of dimensionless CHF correlations for subcooled flow boiling in microgravity and Earth gravity. Int. J. Heat Mass Transf. 50, 4568–4580 (2007).
16. Lazarek, G. M. & Black, S. H. Evaporative heat transfer, pressure-drop and critical heat flux in a small vertical tube with R-113. Int. J. Heat Mass Transf. 25, 945–960 (1982).
17. Tran, T. N., Wambsganss, M. W. & France, D. M. Small circular- and rectangular-channel boiling with two refrigerants. Int. J. Multiphase Flow 22, 485–498 (1996).
18. Agostini, B. & Bontemps, A. Vertical flow boiling of refrigerant R134a in small channels. Int. J. Heat Fluid Flow 26, 296–306 (2005).
19. Cooper, M. G. Saturation nucleate pool boiling—a simple correlation. In IChemE Symp. Ser. 86, 786–793 (1984).
20. Hamdar, M., Zoughaib, A. & Clodic, D. Flow boiling heat transfer and pressure-drop of pure HFC-152a in a horizontal mini-channel. Int. J. Refrig. 33, 566–577 (2010).
21. Kenning, D. B. R. & Cooper, M. G. Saturated flow boiling of water in vertical tubes. Int. J. Heat Mass Transf. 32, 445–458 (1989).
22. Sun, L. & Mishima, K. An evaluation of prediction methods for saturated flow boiling heat transfer in mini-channels. Int. J. Heat Mass Transf. 52, 5323–5329 (2009).
23. Kim, S. M. & Mudawar, I. Universal approach to predicting saturated flow boiling heat transfer in mini/micro-channels – Part II: Two-phase heat transfer coefficient. Int. J. Heat Mass Transf. 64, 1239–1256 (2013).
24. Li, W. & Wu, Z. A general criterion for evaporative heat transfer in micro/mini-channels. Int. J. Heat Mass Transf. 53, 1967–1976 (2010).
25. Oh, H. K. & Son, C. H. New correlation to predict the heat transfer coefficient in-tube cooling of supercritical CO_2 in horizontal macro-tubes. Exp. Therm. Fluid Sci. 34, 1230–1241 (2010).
26. Warrier, G. R., Dhir, V. K. & Momoda, L. A. Heat transfer and pressure-drop in narrow rectangular channels. Exp. Therm. Fluid Sci. 26, 53–64 (2002).

27. Liu, Z. & Winterton, R. H. S. A general correlation for saturated and subcooled flow boiling in tubes and annuli, based on a nucleate pool boiling equation. Int. J. Heat Mass Transf. 34, 2759–2766 (1991).
28. Kew, P. A. & Cornwell, K. Correlations for the prediction of boiling heat transfer in small-diameter channels. Appl. Therm. Eng. 17, 705–715 (1997).

APPENDIX B

B1. Positive and Negative Event Counts vs. Heat Flux

Figure B1 separates the total event count into positive and negative polarities. Positive and negative events correspond to local brightness increases and decreases, respectively. Both polarities increase with heat flux, indicating that stronger boiling activity produces more frequent contrast changes. The polarity counts should not be interpreted as direct phase indicators. Instead, they provide complementary information on the direction of brightness changes associated with moving liquid vapor interfaces, reflections, and shadows. These results establish the global event-activity response across operating conditions before more detailed temporal and spatial descriptors are examined.

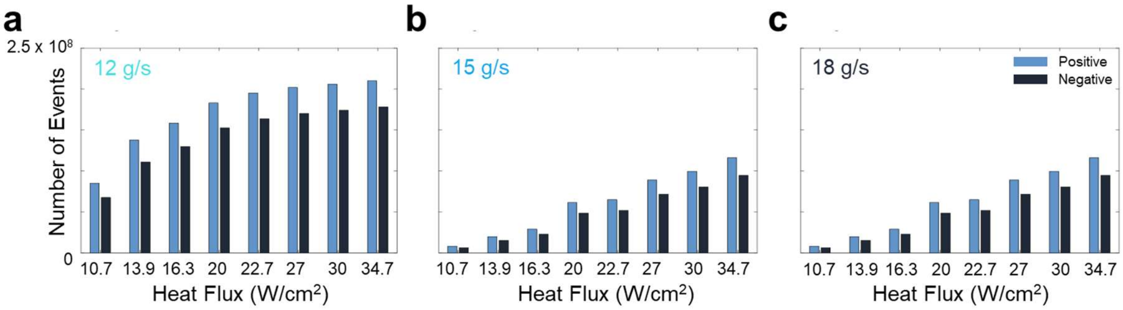

Figure B1. Polarity resolved event counts across flow boiling conditions. Positive and negative event counts are shown across heat flux conditions. Both polarities increase with heat flux, indicating more frequent brightness changes associated with liquid vapor interfacial activity. The polarity counts are not interpreted as direct phase indicators, but as complementary information on the direction of brightness changes.

B2. Representative Event Rate Traces

Representative event rate signals are shown in Figure S2 for selected low, intermediate, and high heat flux cases at mass flow rates of 12, 15, and 18 g/s. Each signal is obtained from the time-binned event stream using $\Delta t = 5$ms over a 3 s observation window. The dashed line indicates the mean event rate for each condition, and the red marker indicates the peak event rate within the observation window. These traces provide direct examples of the temporal event response used to calculate the mean event rate and relative event rate fluctuation in the main analysis.

At lower heat flux, the event rate signal is generally lower in magnitude and can be dominated by intermittent activity. As heat flux increases, the event rate level becomes higher and more sustained, indicating stronger event-generating liquid-vapor interfacial activity. The response also varies with mass flow rate. In particular, the 18 g/s case shows much weaker event activity at the lowest heat flux, while higher heat flux conditions produce more pronounced and sustained event rate signals. These representative traces support the interpretation that event-based sensing captures time-resolved changes in interfacial activity beyond condition-averaged event counts.

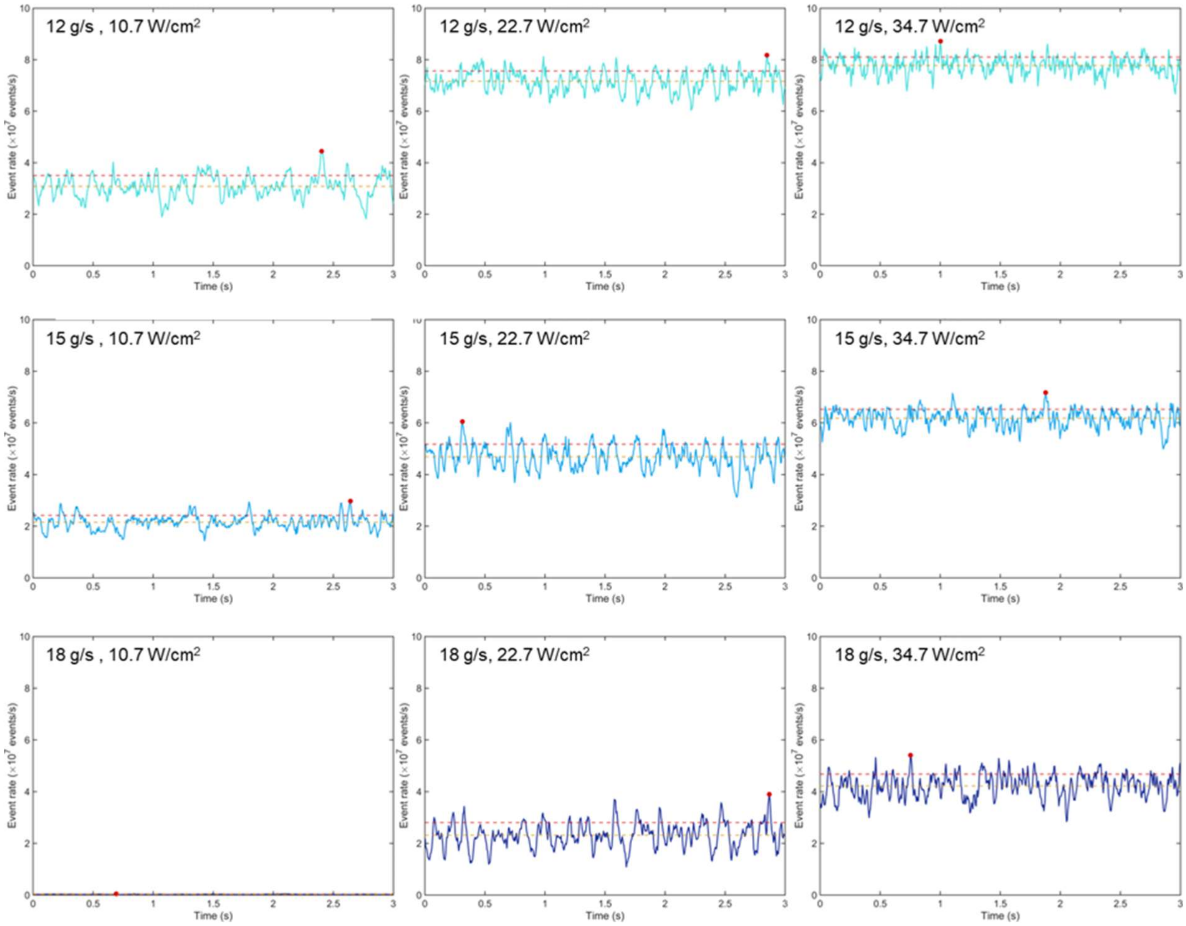

Figure B2. Representative event rate time traces across mass flow rate and heat flux conditions. Event rate signals are shown for selected low, intermediate, and high heat flux cases at mass flow rates of 12, 15, and 18 g/s. Each signal is calculated from time-binned events using Δt=5ms over a 3 s observation window. The dashed line indicates the mean event rate for each condition, and the red marker indicates the peak event rate within the observation window. The traces show that event activity increases and becomes more sustained with increasing heat flux, while mass flow rate modifies the event rate magnitude and fluctuation pattern.

B3. Time-Bin Sensitivity of Temporal Descriptors

To evaluate the effect of time-bin width on the temporal event rate analysis, representative low, intermediate, and high heat flux cases are reprocessed using $\Delta t = 1$, 2, 5, and 10 ms. The analysis focuses on peak event rate and computational time because these quantities are directly affected by the temporal binning scale. The computational time is measured using MATLAB on the same desktop workstation for all cases and includes event timestamp binning, event rate signal construction, and temporal descriptor extraction. Therefore, the values are intended for relative comparison across bin widths rather than as hardware-independent processing benchmarks. The mean event rate is not included in this sensitivity comparison because it is determined primarily by the total number of events divided by the total measurement duration and is therefore nearly independent of Δt.

As shown in Figure B2a, the peak event rate changes only modestly across the tested bin widths. For example, at the high heat flux condition, the peak event rate decreases from 5.65×10^7events/s at $\Delta t = 1$ms to 5.56×10^7events/s at $\Delta t = 5$ ms and 5.51×10^7events/s at $\Delta t = 10$ ms. Similar behavior is observed for the low and intermediate heat flux cases. This indicates that the strongest event-active periods remain consistently identifiable over the tested bin-width range.

The computational time for event rate binning and descriptor extraction is shown in Figure B2b. For each representative case, the processing time decreases as Δt increased because larger bin widths produce fewer time bins. However, the reduction from $\Delta t = 5$ ms to $\Delta t = 10$ ms is relatively small compared with the reduction from finer bin widths. Therefore, $\Delta t = 5$ ms is selected for the main analysis as an intermediate temporal scale that preserves transient event activity while reducing computational cost relative to finer bin widths and avoiding the stronger temporal smoothing associated with $\Delta t = 10$ms.

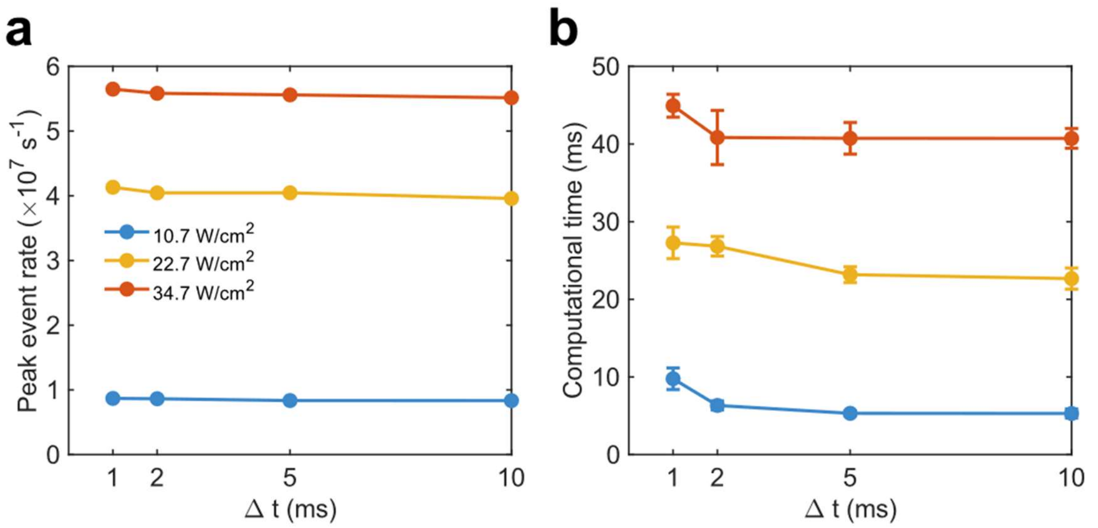

Figure B3. Time bin sensitivity of temporal descriptors. Representative low, intermediate, and high heat flux cases are reprocessed using bin widths of Δt = 1,2,5, and 10 ms. (a) Peak event rate and (b) computational time are compared across bin widths. Larger bins smooth short time fluctuations and reduce computational cost, while Δt = 5 ms provides a balance between temporal resolution, burst characterization, and processing efficiency.

B4. Threshold Sensitivity of Event Coverage

The sensitivity of the high-density coverage ratio, C_{high}, to the globally scaled event density threshold is examined in Figure S4. In the main analysis, high density event regions are identified using θ=0.50, which retains pixels with event density greater than 50% of the global maximum density observed across all tested conditions. The threshold is selected to provide a practical balance between spatial selectivity and a measurable coverage range across the operating conditions.

At lower thresholds of θ=0.30 and θ=0.40, a broader fraction of the observation window is identified as active. For example, at 12 g/s and 34.70 W/cm², C_{high}, reaches 0.640 at θ=0.30 and 0.522 at θ =0.40. These thresholds include moderately active regions in addition to the most concentrated event density regions. In contrast, strict thresholds of θ=0.80 and θ=0.90 retain only a very small fraction of the observation window. At 12 g/s and 34.70 W/cm², C_{high}, decreases to 0.00475 at θ=0.80 and 0.000380 at θ=0.90. At θ=0.90, the 18 g/s condition remains near zero across the tested heat flux range.

The selected threshold of θ=0.50 maintains sufficient selectivity for strongly active event regions while preserving a clear dynamic range across heat flux and mass flow rate. At 34.70 W/cm², C_{high} is 0.339, 0.250, and 0.114 for the 12, 15, and 18 g/s conditions, respectively. Thus, θ=0.50 captures the heat flux dependent spatial expansion of event activity and retains the flow rate dependent differences without the broad inclusion of moderate density regions at lower thresholds or the near zero coverage obtained at stricter thresholds.

Across all tested thresholds, the overall trend remains consistent. High density coverage generally increases with heat flux, and the lower mass flow rate conditions exhibit greater coverage than the 18 g/s condition. Increasing the threshold reduces the absolute coverage because only the most concentrated event density regions are retained. This sensitivity analysis supports θ=0.50 as a practical global threshold for comparing high density event coverage across the tested flow boiling conditions.

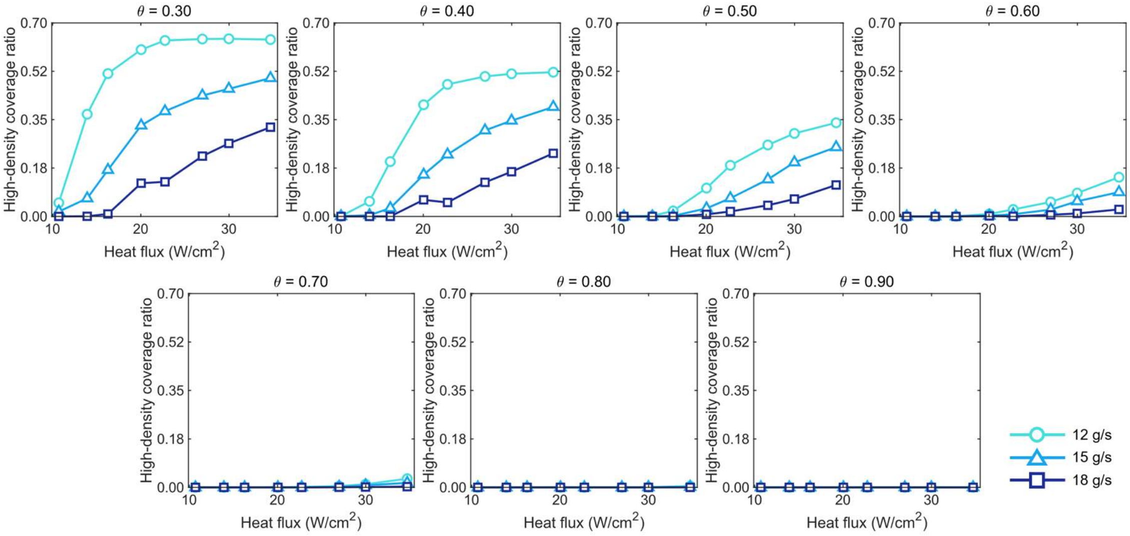

Figure B4. Threshold sensitivity of high-density event coverage. High density coverage ratio, C_{high} is calculated using thresholds of θ with 0.30 to 0.90. The main analysis uses θ=0.50. Lower thresholds include broader moderately active regions, whereas higher thresholds retain only strongly concentrated event density regions. All panels use the same vertical axis range to enable direct comparison of the absolute coverage ratio across thresholds.

B5. Activity Score and PCA Map Construction

This section presents an exploratory principal component analysis-based representation of integrated event activity across the tested flow boiling conditions. The PCA analysis combines selected temporal and spatial descriptors into a continuous condition level activity score. It is included as a supplementary visualization tool and is not used for pressure drop prediction or conventional flow regime classification.

Four descriptors are selected to represent complementary aspects of event generating interfacial activity. These descriptors include mean event rate, $\overline{R_e}$, temporal persistence, P_{temp}, high density coverage ratio, C_{high}, and spatial entropy, H_{sp}. Mean event rate represents the overall intensity of event generation. Temporal persistence represents the degree to which event activity remains sustained over the observation window. High density coverage ratio represents the spatial extent of strongly active event regions. Spatial entropy represents the spatial dispersion of the event density distribution.

Temporal persistence is then defined as:

$$P_{temp} = 1 - F_{rel} \tag{B1}$$

The activity score is defined as the first principal component:

$$S_{PCA} = PC1\left(\overline{R_e}, P_{temp}, C_{high}, H_{sp}\right) \tag{B2}$$

The first principal component explains 73.82% of the total descriptor variance and is used as the integrated event activity score. The PC1 direction is selected so that larger scores correspond to stronger event activity, greater temporal persistence, broader high density coverage, and higher spatial entropy.

The PC1 loading coefficients are listed in Table S1. All four loading coefficients are positive, indicating that the integrated score increases when the selected temporal and spatial descriptors increase together. The loading coefficients describe the contribution of each standardized descriptor to the PCA coordinate and should not be interpreted as causal importance values. For visualization, the PC1 score is linearly rescaled from 0 to 1. This final score normalization is used only to display relative activity levels across operating conditions. It does not change the explained variance, PC1 loadings, or condition ordering.

Table B1. PC1 loadings used to construct the integrated PCA activity score.

Descriptor		PC1 loading
Temporal	Mean event rate, $\overline{R_e}$	0.5609
Temporal	Temporal persistence, P_{temp}	0.5537
Spatial	High-density coverage ratio, C_{high}	0.3478
Spatial	Spatial entropy, H_{sp}	0.5078

Rather than dividing the normalized PCA activity score into equal statistical intervals, descriptive activity boundaries are defined using low activity and high activity reference conditions. These reference conditions are identified from the joint behavior of event density distributions, normalized high density coverage, temporal persistence, and corresponding boiling visualizations.

Low activity reference conditions exhibit sparse and localized event activity with weak temporal sustainment. High activity reference conditions exhibit broader spatial coverage and more temporally sustained activity. The remaining conditions are treated as transitional activity conditions.

The low-to-transitional activity-score boundary is calculated as:

$$S_{L-T} = \frac{[\max(S_{low}) + \min(S_{transitional})]}{2} \tag{B3}$$

where S_{low} and $S_{transitional}$ denote the normalized PCA scores of the low-activity reference conditions and transitional-activity conditions, respectively.

Similarly, the transitional-to-high activity-score boundary is calculated as:

$$S_{T-H} = \frac{[\max(S_{transitional}) + \min(S_{High})]}{2} \tag{B4}$$

where S_{high} denotes the normalized PCA scores of the high-activity reference conditions.

The resulting low to transitional activity boundary is 0.3043, and the transitional to high activity boundary is 0.7386, as listed in Table B2. These boundaries preserve the PCA score as a continuous activity measure while providing dataset specific reference values for interpretation. They are not universal flow regime transition criteria, independently optimized classification boundaries, or vapor morphology boundaries.

Table B2. Descriptive normalized PCA activity-score boundaries.

Boundary	Normalized PCA activity score
Low-to-transitional activity boundary	0.3043
Transitional-to-high activity boundary	0.7386

To visualize the continuous four descriptor PCA score in two dimensions, separate two variable PCAs are applied to the temporal and spatial descriptor pairs. The temporal event activity coordinate is obtained from $\overline{R_e}$ and P_{temp}. The spatial event dispersion coordinate is obtained from C_{high} and H_{sp}.

The temporal coordinate represents the combined variation in time averaged event intensity and temporal sustainment. The spatial coordinate represents the combined variation in high density coverage and spatial entropy. The PC1 loadings used to define the integrated four descriptor activity score are listed in Table B1.

The two-dimensional coordinates are used only to visualize the continuous four descriptor PCA score. They are not independently defined physical regime variables. The normalized four descriptor PCA activity score is represented as a linear function of the spatial event dispersion and temporal event activity coordinates. The locations satisfying the low to transitional and transitional to high activity score boundaries are plotted as dashed iso score lines.

This two-dimensional projection reproduces the normalized four descriptor PCA activity score with $R^2 = 0.9998$. Therefore, the dashed lines provide visual guides for interpreting low, transitional, and high event activity regions. They are projections of the continuous PCA score boundaries and are not independently defined geometric classification boundaries. Conditions located toward lower temporal activity and lower spatial dispersion exhibit weaker and more localized event activity. Conditions located toward higher temporal activity and higher spatial dispersion exhibit stronger, more sustained, and more broadly distributed event activity. Conditions located between these regions exhibit intermediate temporal and spatial characteristics.

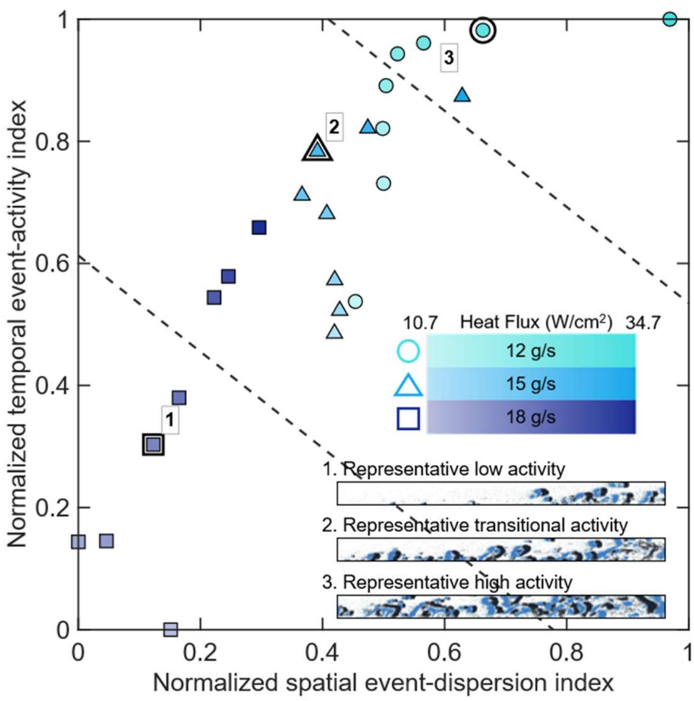

Figure B5. Exploratory spatial temporal activity map constructed from the integrated PCA activity score. The horizontal axis represents the spatial event dispersion coordinate obtained from C_{high} and H_{sp}. The vertical axis represents the temporal event activity coordinate obtained from $\overline{R_e}$ and P_{temp}. Dashed lines indicate the projected low to transitional and transitional to high normalized PCA activity score boundaries. The map is a continuous visualization of event derived activity and is not a conventional flow regime map.

Figure B6 presents the continuous normalized PCA activity score arranged by heat flux and mass flow rate. This supplementary view shows how the integrated event derived activity score varies across the tested operating conditions. Larger scores indicate stronger overall event activity, reflecting increased event intensity and temporal persistence together with broader spatial coverage and dispersion.

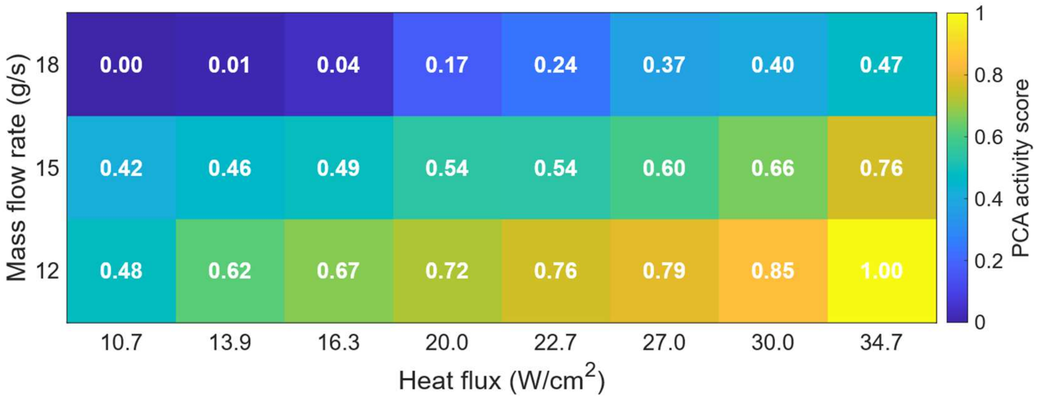

Figure B6. Continuous normalized PCA activity score arranged by heat flux and mass flow rate. The score is normalized from 0 to 1, where larger values indicate stronger, more spatially distributed, and more temporally sustained event-generating activity.

B6. Pressure Drop Time-Series Measurements

Pressure drop time-series measurements are obtained for all operating conditions to support the pressure-response analysis presented in the main text. The pressure drop is calculated as:

$$\Delta P(t) = P_1(t) - P_2(t) \tag{B5}$$

where $P_1(t)$ and $P_2(t)$ are the upstream and downstream pressure signals, respectively. Figures B6–B8 show the pressure drop traces for mass flow rates of 12, 15, and 18 g/s over the first 35 s of each measurement. Each subplot corresponds to a different heat flux condition, and the same y-axis scale is used across all cases to allow direct comparison of the pressure fluctuation magnitude. These time-dependent pressure traces confirm that the measured pressure response contains both the mean pressure drop level and temporal fluctuation behavior, which supports the use of pressure-related descriptors and the time-averaged pressure drop prediction analysis.

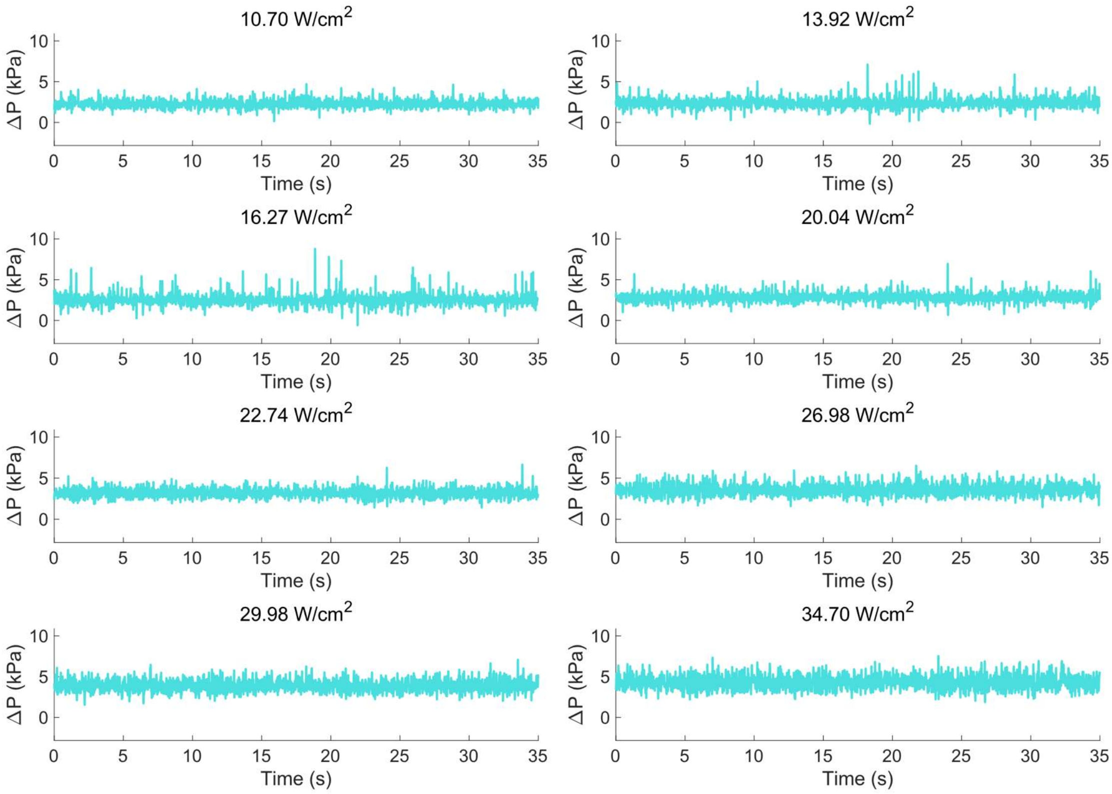

Figure B7. Pressure drop time-series measurements at 12 g/s.

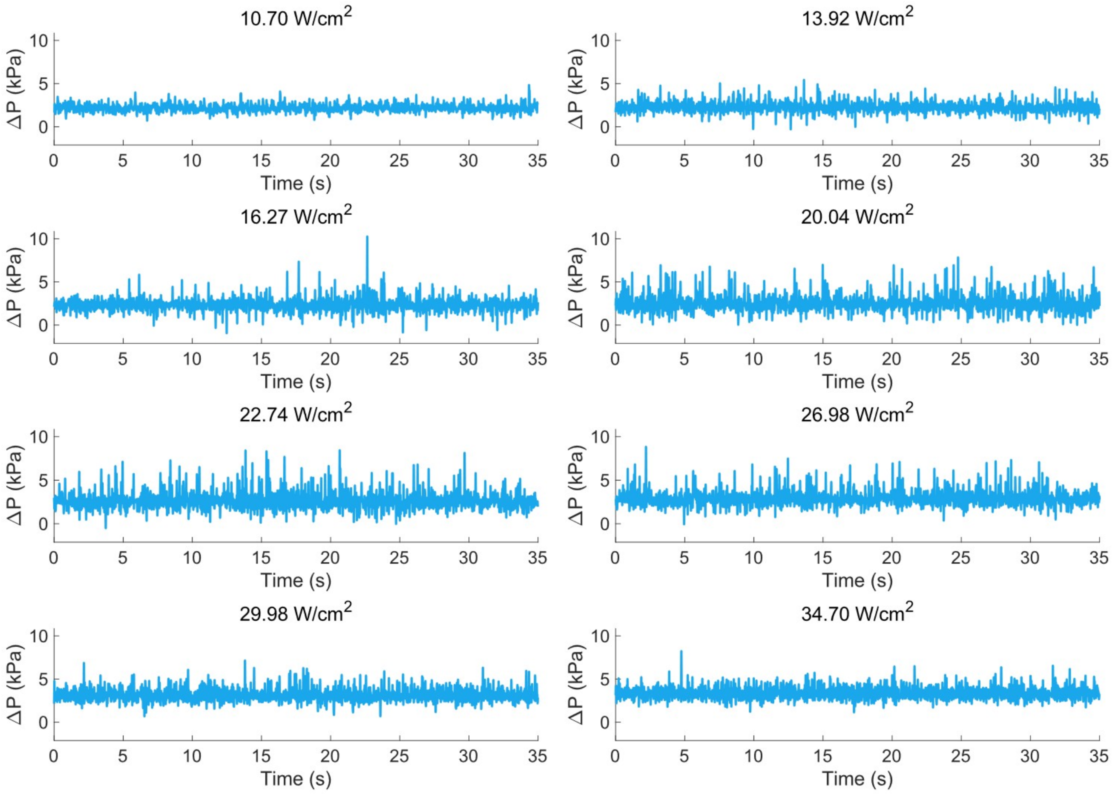

Figure B8. Pressure drop time-series measurements at 15 g/s.

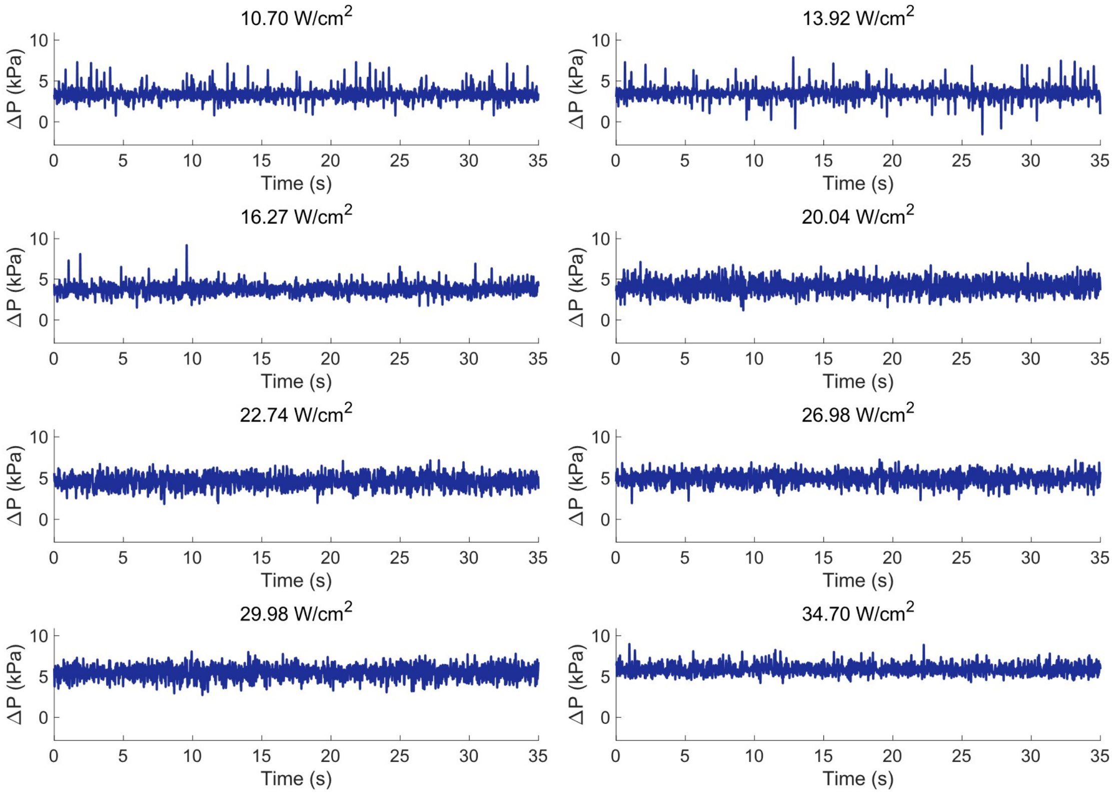

Figure B9. Pressure drop time-series measurements at 18 g/s.

B7. Pressure Drop Model and Feature Comparison

The pressure drop prediction analysis evaluates whether the event-derived temporal instability descriptors contain quantitative information related to the measured pressure drop and whether they improve prediction beyond operating conditions alone. The input definition, MLP architecture, model-selection procedure, and cross-validation strategy are described in Section 1.2. This supplementary section focuses on the feature-group comparison and the comparison with the Ridge regression baseline.

For the main MLP analysis, four feature groups are evaluated: operating conditions only, event descriptors only, operating conditions with temporal instability descriptors, and operating conditions with all event descriptors. The operating-only model uses mass flow rate and heat flux as the baseline input set. The event-only model tests whether event-derived descriptors contain pressure-relevant information without imposed operating conditions. The operating plus temporal instability descriptor model combines mass flow rate and heat flux with relative event rate fluctuation, and spectral entropy. The operating plus all event descriptor model evaluates whether adding the broader event descriptor set further improves prediction. The feature groups and prediction performance are summarized in Table B3.

Table B3. MLP-based Pressure drop prediction performance using operating conditions and event-derived descriptors.

Model	Input variables	RMSE	R^2
Operating only	$\dot{m}, q''$	0.1419 kPa	0.9780
Event only	$\overline{Re}, F_{rel}, C_{high}, H_f, H_{sp}$	0.2884 kPa	0.9199
Operating + temporal instability descriptors	$\boldsymbol{\dot{m}, q'', F_{rel}, H_f}$	**0.0940 kPa**	**0.9915**
Operating + all event descriptors	$\dot{m}, q'', \overline{Re}, F_{rel}, C_{high}, H_f, H_{sp}$	0.1371 kPa	0.9819

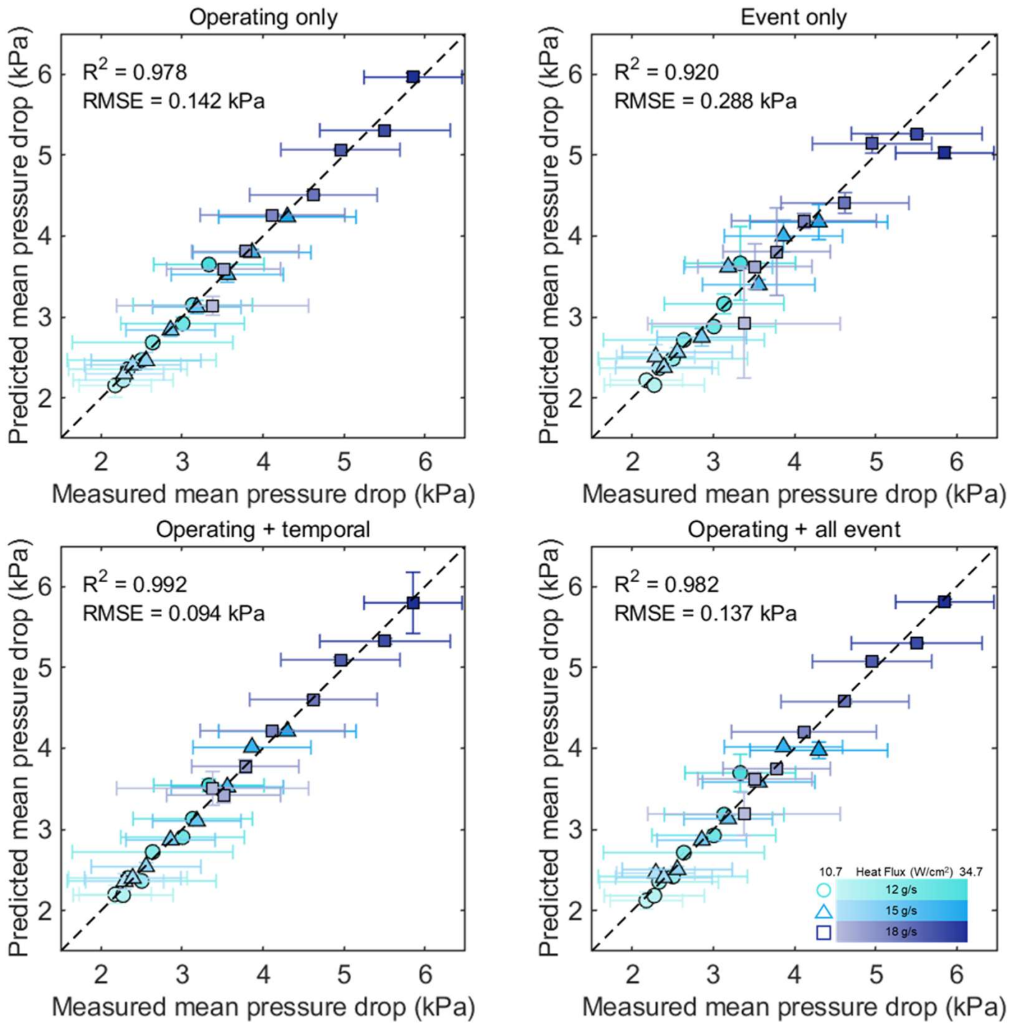

Figure B10. Feature-group comparison for MLP-based pressure drop prediction. Measured versus predicted time-averaged pressure drop for four input-feature groups. The subplots show the results obtained using operating conditions only, event-derived descriptors only, operating conditions combined with temporal instability descriptors, and operating conditions combined with all selected event-derived descriptors. The MLP model uses two fully connected hidden layers, with candidate architectures of [8, 4], [12, 6], and [16, 8], and is evaluated using leave-one-out cross-validation. Marker shape indicates mass flow rate, and color intensity within each flow rate color family indicates heat flux. Horizontal error bars represent the temporal standard deviation of the measured pressure drop signal within each condition, while vertical error bars represent prediction uncertainty estimated from the spread of tested MLP candidates. The dashed line indicates ideal agreement between measured and predicted pressure drop.

The operating-only model gives strong predictive performance, with RMSE = 0.1419 kPa and R^2 = 0.9780, confirming that mass flow rate and heat flux explain most of the pressure drop variation. The event-only model gives RMSE = 0.2884 kPa and R^2 = 0.9199, indicating that event descriptors contain pressure-relevant information but are not sufficient by themselves to replace operating-condition information.

The best performance is obtained when operating conditions are combined with event-derived temporal instability descriptors, giving RMSE = 0.0940 kPa, MAE = 0.0728 kPa, and R^2 = 0.9915. Compared with the operating-only model, adding temporal instability descriptors reduces the RMSE from 0.1419 to 0.0940 kPa, corresponding to an approximately 33.8% reduction. This improvement should be interpreted as a complementary refinement of the operating-condition-based prediction, rather than as evidence that event descriptors replace operating-condition information.

The model using all event descriptors does not further improve the prediction, giving RMSE = 0.1371 kPa and R^2 = 0.9819. This suggests that adding all available descriptors can introduce redundant or weakly pressure-relevant information for this small dataset. Therefore, the operating plus temporal instability descriptor group is used as the pressure drop prediction model in Figure 35b.

To compare the updated MLP approach with the previous regression-based analysis, the same feature-group comparison is also performed using a Ridge regression baseline. The Ridge regression results are summarized in Table B4.

Table B4. Pressure drop prediction performance of the Ridge regression baseline using different input feature groups.

Model	**Input variables**	**RMSE**	**R^2**
Operating only	$\dot{m}, q''$	0.2570 kPa	0.9364
Event only	$\overline{R_e}\ , F_{rel}, C_{high}, H_f, H_{sp}$	0.7763 kPa	0.4200
Operating + temporal instability descriptors	$\boldsymbol{\dot{m}, q'', F_{rel}, H_f}$	**0.2383 kPa**	**0.9453**
Operating + all event descriptors	$\dot{m}, q'', \overline{R_e}\ , F_{rel}, C_{high}, H_f, H_{sp}$	0.2664 kPa	0.9317

For the Ridge regression baseline, the operating-only model gives RMSE = 0.2570 kPa and R^2 = 0.9364, indicating that the operating conditions explain a substantial portion of the pressure drop variation. The event-only model gives RMSE = 0.7763 kPa and R^2 = 0.4200, showing that event-derived descriptors alone are not sufficient to predict pressure drop without the imposed operating conditions. The best Ridge regression performance is also obtained when operating conditions are combined with event-derived temporal instability descriptors, giving RMSE = 0.2383 kPa, MAE = 0.1825 kPa, and R^2 = 0.9453. Compared with the operating-only Ridge regression model, this corresponds to an RMSE reduction of 0.0187 kPa, or approximately 7.3%.

The Ridge regression model using all event descriptors does not further improve the prediction, giving RMSE = 0.2664 kPa and $R^2 = 0.9317$. This suggests that adding all descriptors can introduce redundant or weakly relevant variables for the limited dataset, rather than consistently improving the regression performance. This trend is consistent with the MLP comparison, where the temporal instability descriptor group provides the most useful additional pressure-relevant information, while the full event descriptor set can introduce redundant or weakly relevant variables for the limited dataset.

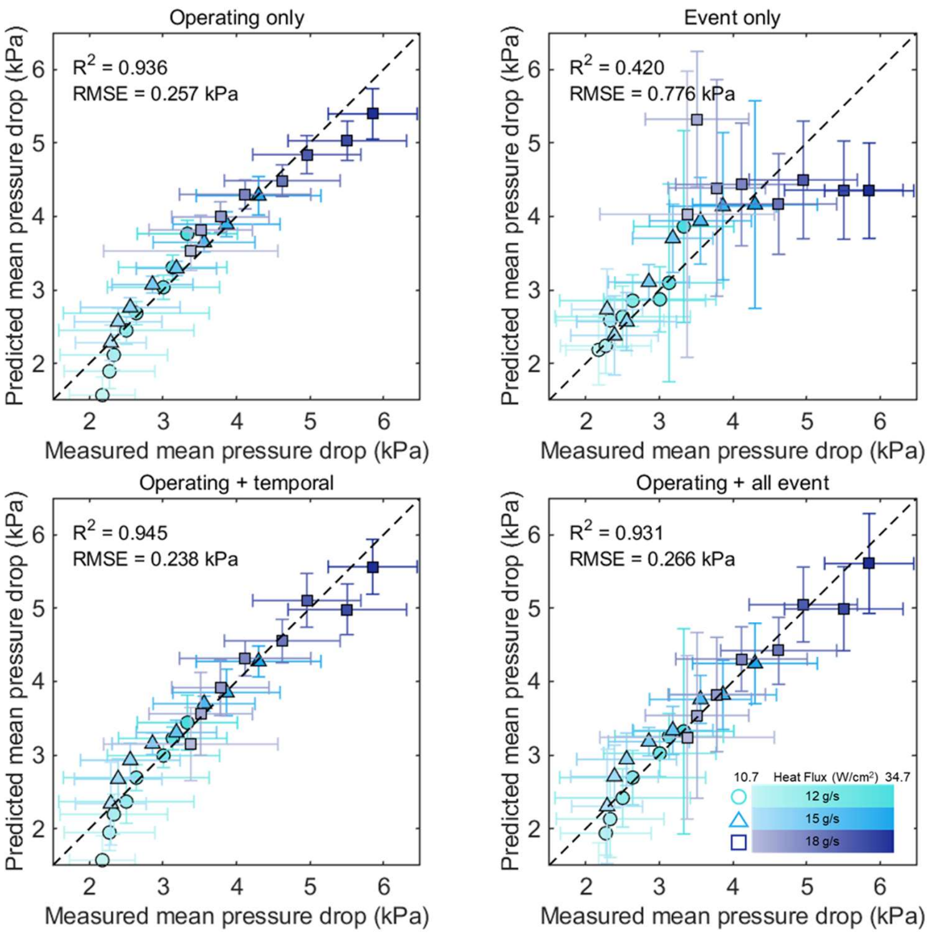

Figure B11. Feature-group comparison for Ridge regression-based pressure drop prediction. Measured versus predicted time-averaged pressure drop for four input-feature groups using Ridge regression with leave-one-out cross-validation. The subplots correspond to operating conditions only, event-derived descriptors only, operating conditions with temporal instability descriptors, and operating conditions with all selected event-derived descriptors. Marker shape indicates mass flow rate, and color intensity indicates heat flux. Horizontal error bars represent measured pressure drop fluctuation, while vertical error bars represent bootstrap-estimated prediction uncertainty. The dashed line indicates ideal agreement.

Overall, both the MLP and Ridge regression comparisons show that temporal instability descriptors provide complementary information beyond mass flow rate and heat flux. The MLP model gives lower prediction error than the Ridge regression baseline, suggesting that the pressure drop response is better captured when nonlinear relationships between operating conditions and event-derived temporal unsteadiness are considered.

APPENDIX C

C1. V2E Conversion

In the realm of event-based networks, many datasets have been created by converting existing frame-based datasets into event-based representations. Notable event datasets such as MNIST-DVS[1], CIFAR10-DVS[2], N-Caltech101[3], and N-MNIST[3] are derived from MNIST, CIFAR10, and Caltech101 by displaying the original images on a monitor, one at a time. In the case of N-MNIST and N-Caltech101, an event camera was moved slightly back and forth, whereas for MNIST-DVS and CIFAR10-DVS, the displayed images were moved while the event camera remained fixed. While this method has been effective, software-based emulators have emerged as an alternative for generating synthetic event data, providing a more flexible and scalable approach to dataset creation for event-based models.

One such emulator is V2E (Video-to-Event), an advanced Python-based tool designed to convert conventional frame-based video into synthetic Dynamic Vision Sensor (DVS) event streams.[4] It replicates the behavior of an event camera by detecting luminance changes between consecutive frames and generating event data in an Address-Event Representation (AER) format. This process incorporates a precise DVS pixel model, which accounts for the inherent non-idealities of real event cameras, ensuring the generated events closely mimic real-world sensor outputs. Additionally, V2E can leverage Super-SloMo synthetic slow-motion up-sampling to enhance the temporal resolution of standard frame-based videos, further improving the quality of the event data.

V2E plays a crucial role in computer vision and neuromorphic engineering research, where the high temporal resolution, low latency, and low power consumption of event-based data offer significant advantages. A key application of V2E is in transfer learning, where it facilitates the adaptation of frame-based datasets into event-based formats for training and evaluating event-based neural networks. In our study, we integrated V2E into this transfer-learning process, converting a total of 15 high-speed video recordings into event streams for in-depth analysis. By enabling efficient extraction of meaningful temporal features, V2E enhances the usability of video data, aligning with the growing demand for event-based vision in modern technological landscapes.

C2. Model Training

To develop robust and generalizable classification models, the dataset is divided into three subsets. 70% of the data is used for training, 15% for validation, and the remaining 15% for testing. This structured data split ensures that each of the seven flow regimes, including bubbly, elongated bubbly, slug, stratified smooth, stratified wavy, annular, and unstable, is adequately represented in all subsets. The inclusion of all regimes across the training, validation, and testing phases allows the models to learn the unique characteristics of each regime and generalize well to unseen data. Additionally, it helps to prevent overfitting by ensuring that the models are not overly tuned to any specific subset of the data.

Each model architecture follows a training pipeline specifically tailored to its input data representation. Convolutional neural network models are trained using reconstructed frames generated from both high-speed optical recordings and event-based data. The convolutional neural network architectures considered in this study include ConvNeXt, AlexNet, and a lightweight custom-designed shallow convolutional neural network. Preprocessing for all convolutional models involves resizing images to match the input dimensions of each model, normalization to maintain consistent input scales, and data augmentation techniques such as random cropping, flipping, and rotation to improve the generalization ability of the models. ConvNeXt and AlexNet benefit from fine-tuning with weights pre-trained on the ImageNet dataset, which provides a strong initialization based on a large and diverse visual dataset. In contrast, the shallow convolutional neural network is trained from the beginning using only the flow boiling data, allowing it to learn lightweight representations that are well-suited to the sparse and high-temporal-resolution characteristics of the event-based inputs. Among the convolutional models, the shallow convolutional neural network achieves the highest classification accuracy on the event dataset, with an accuracy of 99.04%. It also exhibits the lowest inference latency of 0.15 ms and the smallest model size of 1.90 MB, as detailed in Table C1.

Table C1. Performance Comparison of CNN Models on Optical and Event Datasets.

Model	Optical Dataset	Event Dataset	Event Model Latency	Event Model Size	Event Model Parameters
ConvNeXt (scratch)	81.46%	72.26%	0.23 ms	334.06 MB	88.6 M
ConvNeXt (fine-tuned)	87.64%	88.73%	0.23 ms	334.06 MB	88.6M
AlexNet (scratch)	87.01%	96.99%	0.17 ms	217.53 MB	61.1M
AlexNet (finetuned)	84.79%	85.08%	0.17 ms	217.53 MB	61.1M
Shallow CNN	92.24%	99.04%	0.15 ms	1.9 MB	0.5M

Event-driven models operate directly on raw event streams rather than reconstructed image frames. This includes both SNNs and recurrent models such as LSTM networks. The spiking neural network architecture leverages leaky integrate and fire neurons to process the sparse and asynchronous nature of the event stream data. These neurons integrate incoming input currents over time and fire a spike when the membrane potential exceeds a threshold, effectively capturing temporal dynamics over a series of discrete time steps. Training is conducted using surrogate gradient descent, a method designed to handle the non-differentiability of spike functions during backpropagation. The SNN processes data over 15 time steps and uses a learning rate of 0.0001. Despite its low complexity, this model achieves competitive performance while maintaining a compact memory footprint of 0.94 MB, making it highly suitable for resource-constrained applications such as edge computing or embedded systems.

The LSTM model processes raw event data formatted as sequential triplets of spatial coordinates and polarity, denoted as x, y, and polarity. The recurrent layers in the LSTM architecture are capable of capturing long-range temporal dependencies, which are critical for accurately classifying flow regimes that evolve gradually or transition between states. This includes challenging cases such as transitions between stratified smooth and annular flow regimes. Unlike convolutional models that require reconstructed frames, the LSTM model directly consumes raw event data, substantially reducing the need for preprocessing. It is trained using a learning rate of 0.001 and maintains a relatively compact model size of 1.27 MB, balancing classification performance with computational efficiency.

In addition to deep learning approaches, a classical Fourier-based method is implemented as a baseline for comparison. This method operates on reconstructed event frames by transforming the spatial domain images into the frequency domain using the fast Fourier transform. Features are extracted from the power spectrum of the transformed images and are subsequently classified using a two-step process involving k-means clustering followed by k-nearest neighbors classification. While this approach is computationally less intensive in terms of model depth and training, it has a larger storage requirement due to the need to retain frequency domain features and cluster assignments. The total model size for this method is 5.88 MB, which is the largest among the models evaluated. Furthermore, its classification performance is limited in scenarios with overlapping spectral characteristics between regimes, which is evident in Figure C1 where some flow regimes exhibit significant overlap in their signal-to-noise ratio clusters.

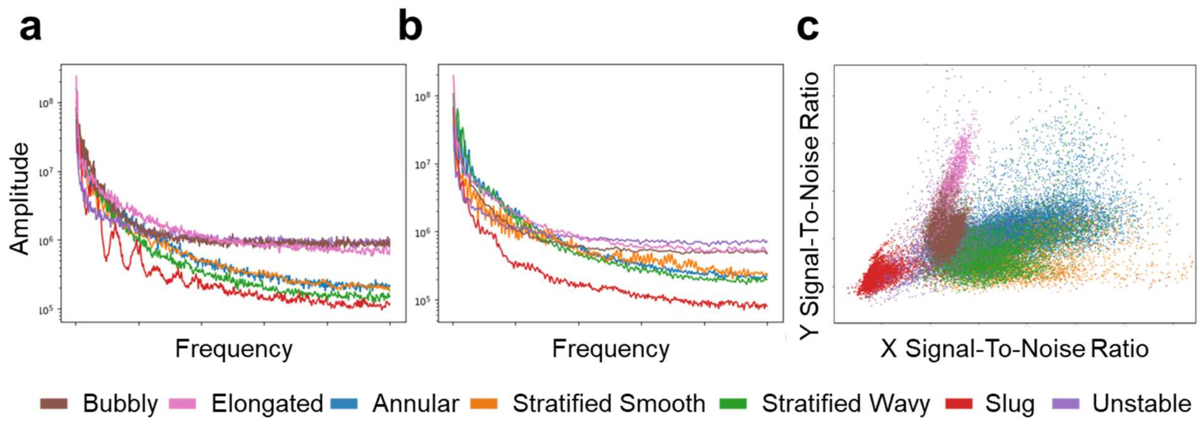

Figure C1. Clustering of Signal-to-Noise Ratios for Fourier-Based Classification. (a) and (b) show representative examples of the x and y power spectra derived from the Fourier-based method for different flow regimes. (c) illustrates clustering based on the x and y signal-to-noise ratios, highlighting the separation of regimes. The slug regime, depicted in red, demonstrates a dense and distinct cluster, showcasing the utility of signal-to-noise ratio as a feature for classification. These plots highlight the key features used in the Fourier-based analytical method to distinguish between flow regimes.

All models are trained and evaluated using an NVIDIA A30 graphics processing unit. A consistent set of generic hyperparameters is applied to all models, with slight adjustments based on the architecture. The Adam optimizer is used across all models, with momentum decay set to 0.9 and second-order moment decay set to 0.999. The batch size is fixed at 128 to ensure stable gradient estimates while maintaining efficient memory usage. The learning rate is set to 0.001 for convolutional models and the LSTM model, and 0.0001 for the SNN. The number of training epochs ranges from 25 to 55, depending on the model's convergence behavior and the complexity of the input data as shown in Table C2.

Table C2. Generic hyperparameter settings for models.

Hyperparameter	Optical CNN	Event CNN	Event SNN	Event LSTM
Epochs	35	25	55	25
Batch Size	128	128	128	128
Optimizer	Adam	Adam	Adam	Adam
Learning Rate	1e-3	1e-3	1e-4	1e-3
SNN β	N/A	N/A	0.95	N/A
SNN Steps	N/A	N/A	15	N/A

The dataset used in training consists of a combination of real and emulated event data to ensure both realism and comprehensive regime coverage. Real event data is acquired using a Prophesee neuromorphic event camera, which captures asynchronous brightness changes with high temporal resolution and accuracy. These recordings provide authentic hardware-based observations of dynamic flow boiling phenomena. However, due to experimental limitations in capturing certain flow regimes such as annular and stratified flows, additional data is generated by converting high-speed optical recordings into synthetic event streams using the V2E emulation tool. This tool simulates the behavior of dynamic vision sensors by detecting pixel-level brightness differences between consecutive frames and generating corresponding event streams. By combining real and emulated event data, the dataset includes complete coverage of all flow regimes, supporting model training and evaluation across a broad range of boiling conditions. Detailed information about the event accumulation times, spatial resolutions, and the number of frames per regime is provided in Table C3.

The number of event frames reported in Table C3 depends on the regime-specific accumulation time and temporal sampling procedure. Because different temporal windows are used according to the characteristic event activity of each regime, both the event density and the resulting number of frames vary across the dataset.

Table C3. Summary of Real and Emulated Event Data for Flow Regime Classification

Mass Flux (kg/m^2s)	Heat Flux (kW/m^2)	Event Frames	Total Events	Regime
880	3.75	3266	$1.63*10^8$	Bubbly
	5.4	1367	$6.83*10^7$	Bubbly
	7.35	1479	$7.39*10^7$	Bubbly
	9.6	1206	$6.03*10^7$	Bubbly
	12.15	1441	$7.20*10^7$	Bubbly
	15	1235	$6.17*10^7$	Elongated Bubbly

	18.15	1338	$7.14*10^7$	Elongated Bubbly
140	9.4	740	$3.7*10^7$	Stratified Smooth
	18	1726	$8.63*10^7$	Stratified Wavy, Stratified Smooth
	30.3	1860	$9.3*10^7$	Annular, Unstable
	43	17757	$8.79*10^7$	Annular
200	6.8	2308	$1.15*10^8$	Slug
	13	25577	$1.28*10^8$	Stratified Wavy, Stratified Smooth, Unstable
	22	3950	$1.98*10^8$	Stratified Wavy, Stratified Smooth, Unstable
	36.3	3474	$1.74*10^8$	Annular, Unstable
	53	3029	$1.51*10^8$	Annular, Unstable
	70	2606	$1.3*10^8$	Annular, Unstable

255	8	3773	$1.89*10^8$	Slug
	15.4	2767	$1.38*10^8$	Stratified Wavy, Stratified Smooth, Unstable
	28	3609	$1.8*10^8$	Stratified Wavy, Stratified Smooth, Unstable
	48	3408	$1.7*10^8$	Annular, Unstable
	69.5	2944	$1.47*10^8$	Annular, Unstable

C3. Event Accumulation Time Selection for Event-Frame Representations

Unlike conventional cameras, an event camera records asynchronous brightness-change events rather than images at a fixed frame rate. To construct inputs for frame-based models, including the Event CNN and Event SNN, the event stream is converted into event frames by accumulating events over a temporal window, Δt. Each event frame represents the spatial distribution of brightness changes occurring within the selected interval. The accumulation time therefore determines how much temporal event information is integrated into a single image-like representation.

A single accumulation time is not applied uniformly to all flow regimes in this study. Instead, the accumulation window ISs adjusted according to the characteristic event activity and interface dynamics of each regime. This regime-specific approach Is used because the vapor-liquid structures exhibit substantially different motion scales. For example, bubbly and elongated bubbly flows contain localized interfaces with relatively rapid bubble growth and motion, whereas stratified smooth flow contains more persistent and slowly evolving vapor-liquid boundaries. Similarly, annular and unstable flows can exhibit dense interfacial activity, wave motion, or rapidly changing vapor structures. Applying an identical temporal window to all regimes could therefore produce overly sparse representations for some regimes and excessive temporal superposition for others.

Short accumulation windows preserve rapid bubble growth, interface deformation, and transient vapor motion with high temporal resolution. However, fewer events are collected within a short interval, which can produce sparse event frames with incomplete bubble contours or isolated event clusters. In contrast, longer accumulation windows increase the event density and provide more continuous representations of vapor-liquid structures. This is beneficial for regimes with relatively persistent interfaces or lower local event activity. However, when the accumulation time becomes excessively long, events generated at different interface locations are combined into the same event frame. Moving bubbles and vapor-liquid boundaries can then appear spatially broadened, reducing the visibility of short-lived features.

The regime-specific accumulation times are selected through visual and quantitative examination of event-frame quality. Candidate windows are evaluated to identify a representation that retained recognizable vapor morphology while providing sufficient event density for model training. The selected values are not chosen solely to maximize the number of events in each frame. Instead, each window is selected to balance spatial continuity, preservation of transient interface behavior, and the avoidance of excessive motion blur caused by temporal accumulation. Figure C2 illustrates this tradeoff: shorter windows capture fast interface motion but may remain sparse, whereas longer windows reveal more continuous structures but can merge multiple interface positions.

Event-frame accumulation inherently compresses the raw asynchronous event stream. Although events occurring within the selected window are retained spatially, their exact temporal ordering is not explicitly preserved in the final two-dimensional frame. Therefore, some fine temporal information is lost relative to the original event sequence. This loss is minimized by selecting accumulation windows that remain short relative to the characteristic evolution time of the relevant vapor structures. The resulting event frames preserve the regime-dependent morphology and overall interfacial activity needed for frame-based classification, while enabling compatibility with convolutional and spiking neural-network architectures.

It should be noted that regime-specific accumulation is used here as a dataset-construction and representation study. Because the appropriate accumulation time is selected based on the known regime characteristics, this approach uses information that would not be available before classification during a fully blind real-time deployment. Therefore, a practical real-time system would require either a single common accumulation time, an event-rate-based adaptive accumulation rule independent of the regime label, or a raw event model that directly processes asynchronous event sequences. The Event LSTM model considered in this study provides the latter alternative because it operates on sequential event information without requiring a single accumulated event frame as its primary input.

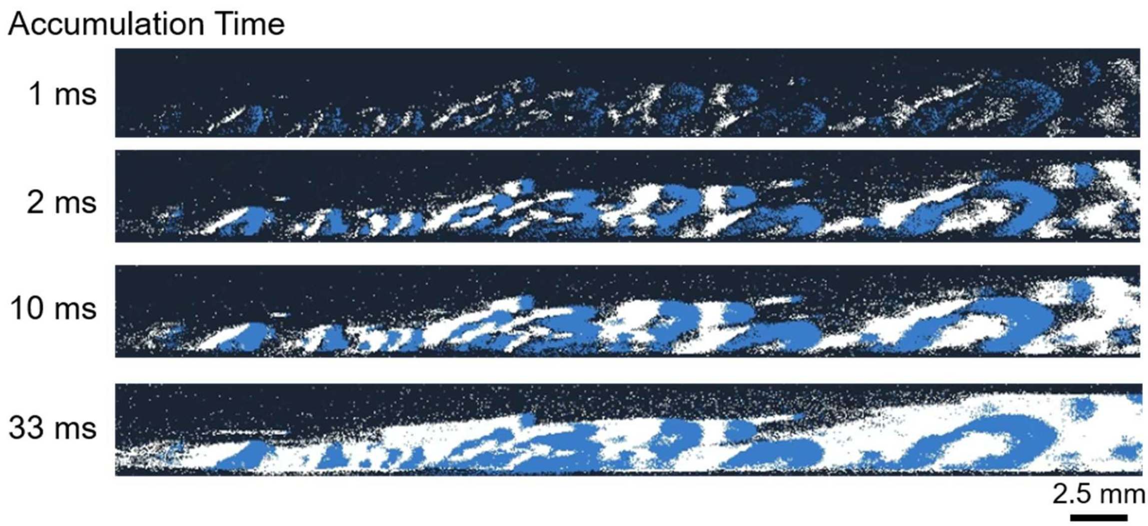

Figure C2. Effect of event accumulation time on event-frame representations of flow boiling. Short accumulation windows preserve fast bubble and interface motion but may produce sparse event frames with limited spatial continuity. Longer accumulation windows increase event density and improve the visibility of vapor-liquid structures; however, excessive accumulation can temporally superimpose moving interfaces and blur transient flow features. Accordingly, regime-specific accumulation times are selected to balance event density and temporal fidelity.

C4. Model Performance

The confusion matrices for Optical CNN, Event LSTM, Event SNN, Event CNN, and Fourier-based models reveal distinct differences in their ability to classify seven flow regimes as shown in Figure C3. Optical CNN achieves moderate accuracy but struggles with unstable flow, often misclassifying it as annular or stratified wavy. It also shows reduced precision in separating stratified smooth and stratified wavy regimes. Event LSTM performs better, accurately identifying early-stage and annular regimes, though it shows some confusion between slug and stratified patterns, suggesting limitations in capturing rapid transitions. Event SNN achieves high accuracy across all regimes with clear diagonal dominance and correctly classifies unstable flow in most cases. Event CNN performs the best overall, with nearly perfect classification and minimal confusion even in challenging transitions between regimes. In contrast, the Fourier model shows the weakest performance, frequently misclassifying unstable and stratified regimes and lacking the resolution needed to capture complex spatiotemporal variations. These results highlight the advantages of event-based learning approaches, especially in decoding dynamic and unstable flow patterns.

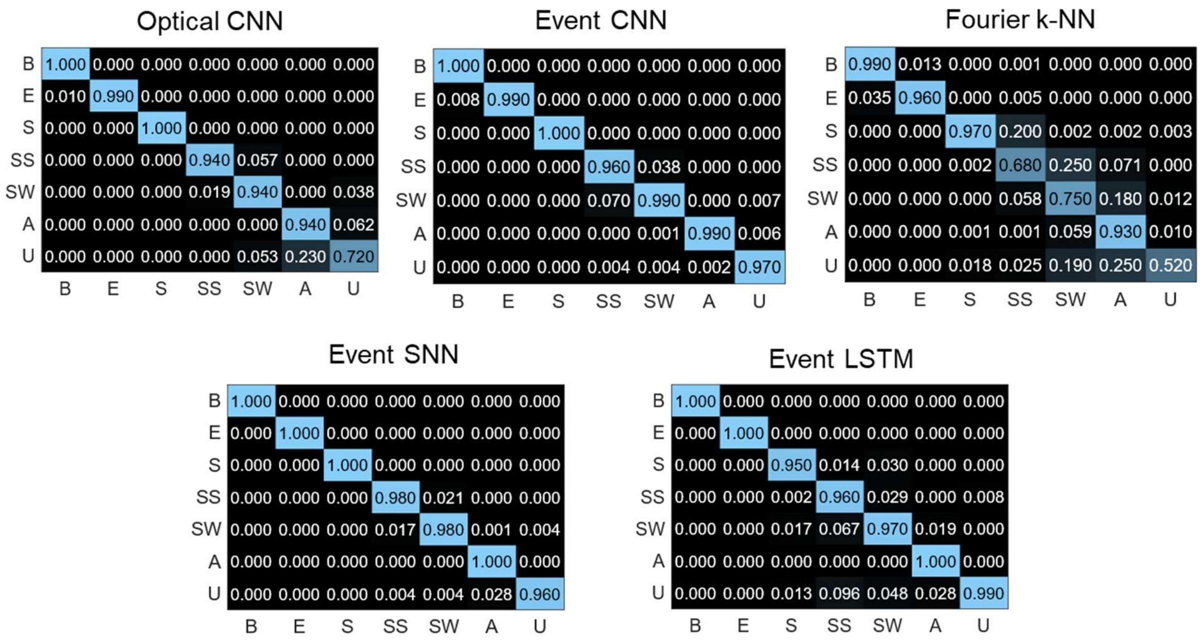

Figure C3. Confusion matrices for seven-class flow regime classification using five models. The heat maps compare the classification performance of Optical CNN, Event CNN, Fourier k-NN, Event SNN, and Event LSTM models on seven flow regimes. Optical CNN shows limited accuracy in unstable and stratified regimes. Event LSTM improves overall consistency but exhibits mild confusion in slug and stratified patterns. Event SNN and Event CNN achieve the highest accuracy with minimal misclassification across all regimes. The Fourier model displays the weakest performance with significant overlap among mid-transition regimes and unstable flow.

To comprehensively evaluate the performance of our model, we utilize precision, recall, and F1-score, which provide deeper insights beyond traditional accuracy metrics, particularly in imbalanced datasets. Precision measures the proportion of correctly predicted positive instances among all predicted positives, indicating the model's ability to minimize false positives. Recall, on the other hand, quantifies the proportion of correctly predicted positive instances out of all actual positives, reflecting the model's ability to detect relevant instances while minimizing false negatives. The F1-score, which represents the weighted average of precision and recall, serves as a balanced metric, particularly useful when there is a trade-off between precision and recall. According to their respective definitions:[5]

$$Recall = \frac{\sum TP}{\sum(TP + FN)} \tag{C1}$$

$$Precision = \frac{\sum TP}{\sum(TP + FP)} \tag{C2}$$

$$F - 1\ score = 2 \times \frac{Precision \times Recall}{Precision + Recall} \tag{C3}$$

where TP, FP, TN, and FN are true positive, false positive, true negative, and false negative, respectively.

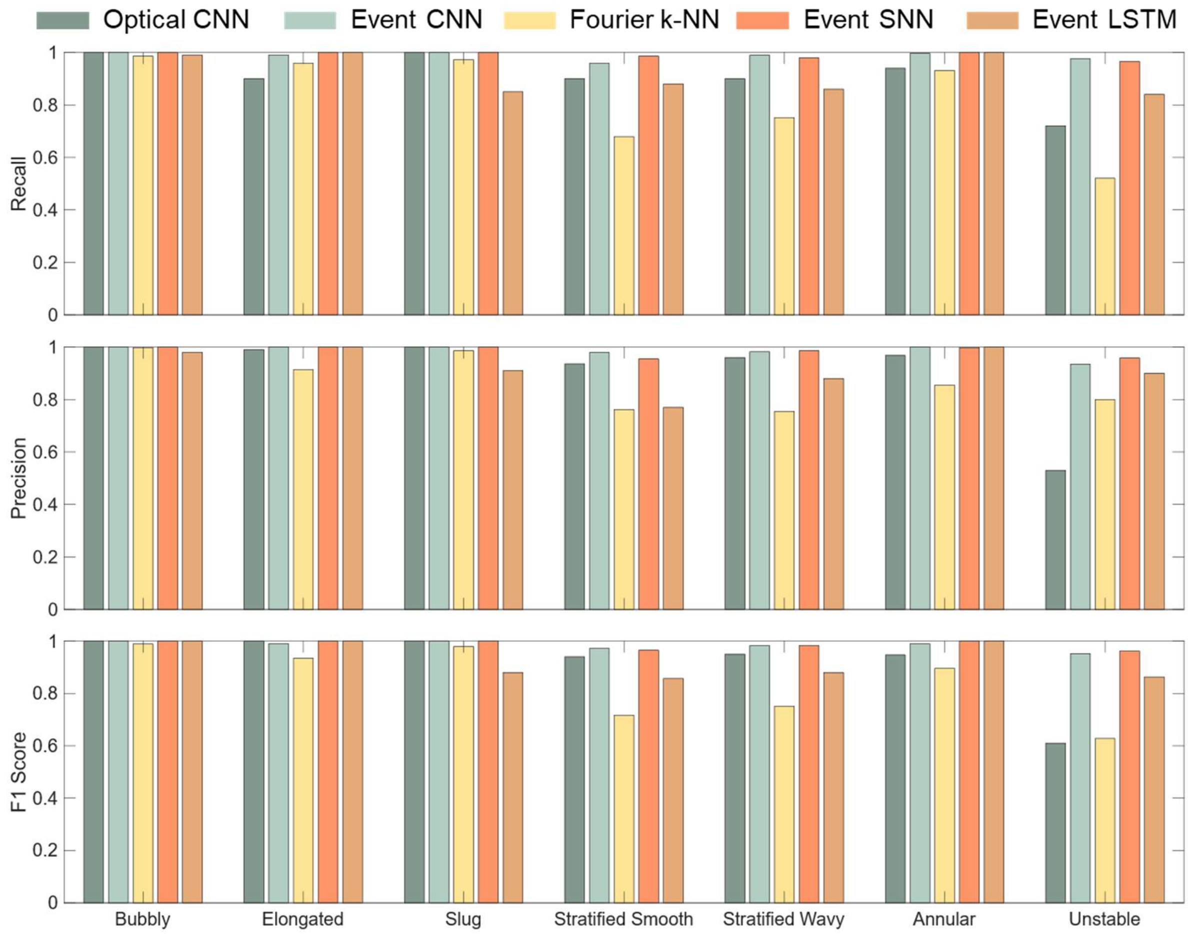

Figure C4. Comparison of Recall, Precision, and F1-Score for the evaluated model. Recall measures the ability to correctly identify positive instances, Precision reflects the proportion of true positive predictions among all positive predictions, and F1-Score represents the harmonic mean of Precision and Recall, balancing both metrics for overall performance assessment.

C5. Real-time Classification

In real-time classification systems using event-based vision, the event sequence length refers to the number of temporally ordered events grouped together as a single input sample for model inference. This parameter is critical because it directly influences classification accuracy, latency, and the system's ability to respond reliably to fast-changing physical phenomena. In our framework, we utilize a lightweight Long Short-Term Memory (LSTM) model to process these event sequences. LSTM networks are well-suited for this task due to their capacity to capture temporal dependencies within asynchronous data streams, making them effective for recognizing dynamic patterns in flow boiling behavior.

To determine the appropriate sequence length for LSTM input, we evaluated several configurations starting from 2,500 events. While shorter sequences in this range allowed for rapid inference, they often lacked sufficient temporal context, resulting in unstable or noisy predictions, especially in transitional flow regimes. Conversely, longer sequences beyond 5,000 events increased computational cost and introduced a slight degradation in performance, likely due to the over-smoothing of temporal information and reduced sensitivity to rapid feature changes. Based on empirical analysis, a sequence length of 5,000 events is selected as the optimal balance. This configuration provided high classification accuracy, maintained a low inference latency of approximately 1.4 ms, and ensured consistent model performance across a wide range of boiling conditions.

Additionally, this sequence length aligns well with our event accumulation and segmentation process, allowing seamless integration into a real-time LSTM-based classification pipeline. It also ensures that each LSTM input contains enough temporal diversity to fully leverage the model’s recurrent structure without exceeding hardware or time constraints required for real-time operation.

References

1. Serrano-Gotarredona T, Linares-Barranco B. Poker-DVS and MNIST-DVS. Their history, how they were made, and other details. *Front Neurosci*. 2015;9:481.

2. Li H, Liu H, Ji X, Li G, Shi L. Cifar10-dvs: an event-stream dataset for object classification. *Front Neurosci*. 2017;11:309.

3. Orchard G, Jayawant A, Cohen GK, Thakor N. Converting static image datasets to spiking neuromorphic datasets using saccades. *Front Neurosci*. 2015;9:437.

4. Hu Y, Liu SC, Delbruck T. v2e: From video frames to realistic DVS events. In: *Proceedings of the IEEE/CVF Conference on Computer Vision and Pattern Recognition*. ; 2021:1312-1321.

5. Fawcett T. An introduction to ROC analysis. *Pattern Recognit Lett*. 2006;27(8):861-874.